TURBULENT FLOWS WITHIN A CYCLONE AND BEHIND AN AHMED VEHICLE MODEL

WANG XIAOWEN

Ph.D

The Hong Kong Polytechnic University

2011

The Hong Kong Polytechnic University

Department of Mechanical Engineering

Turbulent Flows within a Cyclone and behind an Ahmed Vehicle Model

Wang Xiaowen

A thesis submitted in partial fulfillment of the requirements

for the degree of Doctor of Philosophy

August 2011

CERTIFICATE OF ORIGINALITY

I hereby certify that this thesis is my own work and that, to the best of my knowledge and belief, it reproduces no material previously published or written, nor material that has been accepted for the award of any other degree or diploma, except where due acknowledgement has been made in the text.

(Signed) _____

(Name of student) Wang Xiaowen

ABSTRACT

This thesis is an experimental study of turbulent flows, consisting of two parts:

(1) *An investigation of the highly three-dimensional flow structure around a simplified vehicle model*

The lasting high fuel cost has inspired resurgence in drag reduction research for vehicles, which calls for a thorough understanding of the vehicle wake. Flow around the Ahmed vehicle model has received considerable attention in the literature. Nevertheless, our knowledge of this flow is rather incomplete. This investigation aims to revisit turbulent flow structure behind this model. Two rear slant angles, i.e., $\alpha = 25^{\circ}$ and 35°, of the model were examined, representing two distinct flow regimes. The Reynolds number was 5.26×10^4 based on the model height (H) and incident flow velocity. Using particle image velocimetry (PIV), flow was measured with and without a gap ($g/H = 0.174$) between the vehicle underside and ground in three orthogonal planes, viz. the *x-z, x-y* and *y-z* planes, where *x, y* and *z* are the coordinates along longitudinal, transverse and spanwise directions, respectively. The measured velocity and vorticity data reconfirm the well documented major characteristics of the mean flow structure. However, both instantaneous and time-averaged PIV data unveil a number of important aspects of

the flow structure, which have not been captured previously due to a variety of reasons. As such, a considerably modified flow structure model is proposed. Time-averaged velocities, vorticity components, and the Reynolds normal and shear stresses are presented and discussed, along with their dependence on *g/H* in the two distinct flow regimes.

(2) *A detailed study of the extraordinarily complicated turbulence structure in a cylinder-on-cone cyclone*

The turbulent flow within a cylinder-on-cone cyclone is highly three-dimensional and complicated; our knowledge of this flow has yet to be improved. Turbulent flow structure in a cylinder-on-cone cyclone was experimentally investigated, which is characterized by a reverse flow in the core region. Two separate efforts have been made. Firstly, measurements were performed at a fixed swirl number of 3 with the Reynolds number varying from 37,100 to 74,200, based on the inlet velocity and the cyclone body diameter. The flow field in planes normal to and through the cyclone axis was measured in detail using a two-component laser Doppler anemometry (LDA) and PIV. Two dominant frequencies of vortical structures were identified based on LDA-measured tangential and axial velocity spectra. One of them agreed quite well with previous reports, but the other was observed for the first time. One explanation was

proposed. Secondly, special attention was turned to the swirl number effect on the flow. The swirl number examined was from 2.4 to 5.3, with the Reynolds number fixed at 7.4 x 10^4. Three regions of the flow have been identified after careful analysis of the data, which are referred to as the core, the outer and the wall-affected regions, respectively; each is distinct from another in terms of the vorticity concentration, frequency of quasi-periodical coherent structure, the probability density function, mean and variance of velocities. It has been found that the flow, including its Strouhal numbers and radial distributions of the mean and fluctuating velocities, depends considerably on the swirl number.

Acknowledgement

I would like to express my unfeigned deep gratitude to my supervisor, Professor Y. Zhou for his many ideas and insights that have had such a strong influence on the thesis. His precise manner and diligence impress me very much, and it will benefit me in my future career. I would also like to express my gratitude to Drs. W.O. Wong and T.L. Chan, my thesis co-supervisors, for many useful suggestions and discussions. I thank them for giving me the opportunity to learn so much at The Hong Kong Polytechnic University, and giving me encouragement and support throughout the duration of this project.

Thanks are due to many other people for contribution to this work, including Mr. Y.F. Pin, Mr. J.F. Huang, Dr. M.M. Alam, and Mr. P. Zhang.

Finally, I wish to express my thanks to my families for their love, patience and support for all the years I was away from home.

Contents

NOMENCLATURE

A	Inlet area of the cyclone.
a	Inlet height of the cyclone.
b	Inlet width of the cyclone.
d_e	Diameter of the cyclone outlet.
E_α	Power spectral density function of signal α.
F	Flatness.
f	Frequency in spectra.
f_1, f_2	Two distinct precessing vortex frequencies within cyclone.
f_{prec}	Precessing vortex frequency within cyclone.
g	Gap between Ahmed model underside and ground surface.
H	Height of the Ahmed vehicle model.
L	Cyclone cylinder length in Chapters 3 and 4, and length of the Ahmed vehicle model in Chapter 2.
N_1	Number of measured velocity in the range of $0.25 \leq r/R \leq 0.68$ in Chapter 4.
N_2	Number of measured velocity in the range of $-0.25 \leq r/R$

	$\leq$ -0.68 in Chapter 4.
$p(\hat{\alpha})$	Probability density function of quantity $\hat{\alpha}$.
R	Radius of the cyclone cylindrical chamber.
Re	Reynolds number, defined by $\frac{U_\infty H}{\nu}$ in Chapter 2 and $\frac{U_{in}(2R)}{\nu}$ in Chapters 3 and 4.
S	Swirl number $\equiv \pi d_e R/2A$
S_k	Skewness.
St	Strouhal number, defined by $f_{prec}2R/U_{in}$ in Chapters 3 and 4.
T_{v_θ}	Averaged turbulence intensity of tangential velocity.
U_{in}	Inlet velocity of the cyclone (m/sec).
U_∞	Free-stream velocity.
V_r, V_θ, V_z	Instantaneous velocities in radial, circumferential and axial directions, respectively (m/sec).
v_r, v_θ, v_z	Fluctuating velocities in radial, circumferential and axial directions, respectively (m/sec).
U, V, W	Instantaneous velocities in streamwise, spanwise and transverse directions, respectively (m/sec).
u, v, w	fluctuating velocities in streamwise, spanwise and

transverse directions, respectively (m/sec).

Coordinate system

x, y, z	Coordinates in streamwise, spanwise and transverse directions, respectively, in Chapter 2.
r, θ, z	Coordinates in radial, circumferential and axial directions, respectively, in Chapters 3 and 4.

Greek symbols

α	Represents the rear slant angle of the Ahmed vehicle model in Chapter 2 or denotes V_θ, $\overline{V}_\theta$, $v_{\theta,rms}$, or V_r in Chapter 3 and Chapter 4.
β	Denotes $\overline{U}^*$, $\overline{W}^*$, u^*_{rms}, w^*_{rms} in Chapter 2 or $\overline{V}_\theta$, $v_{\theta,rms}$ in Chapter 4.
δ	$\delta = \frac{\beta_N - \beta_{N-\Delta N}}{\beta_N} \times 100\%$, which provides a measure for the dependence of experimental uncertainties on the number of the PIV images.
ν	Kinematic viscosity of fluid
$\Omega_x, \Omega_y, \Omega_z$	Instantaneous vorticity components in streamwise, spanwise and transverse directions, respectively (1/sec).
$\omega_x, \omega_y, \omega_z$	Fluctuating vorticity components in streamwise,

spanwise and transverse directions, respectively (1/sec).

Superscript

*	Denotes dimensionless parameter normalized by H and/or U_∞ in Chapter 2 or R and/or U_{in}, in Chapters 3 and 4.

Subscript

N	Number of PIV images in Chapter 2 and 4.
ΔN	Increment in N in Chapter 2 and 4.
rms	Root mean square value.

Special symbols

^	Circumferentially averaged velocity component: $(\hat{\alpha}(r) = \frac{1}{2\pi}\int_0^{2\pi} \alpha(r,\theta)d\theta \approx \frac{1}{2\pi}\sum_{\theta_i=0}^{2\pi} \alpha(r,\theta_i)\Delta\theta_i)$
¯	Overbar denotes time-averaging.

CHAPTER 1

INTRODUCTION

1.1 Background

The recently high-rise oil price highlights the necessity and urgency of searching for methods to reduce the drag of vehicles. Many classes of transport and multifarious important applications stand to reap great rewards from the successful development of drag reduction technologies. For example, the annual fuel cost is estimated to exceed thirty billion dollars for land vehicles in Hong Kong. About 60% of the total drag of a passenger car driving in a highway is due to the aerodynamic resistance. Apparently, even a very modest reduction in aerodynamics drag of these transport vehicles will lead to a tremendous saving of fuel cost.

Wake behind 3D vehicle models has caught considerable attention recently in the literature because of its fundamental and industrial significance (Oertel 1990). Shear layer separation from the models causes a negative base pressure in the leeward side of the models, resulting in a pressure drag (Roshko 1955). Past studies have unveiled that the pressure drag contributes predominantly to the total drag acting on the vehicle, in particular at a high speed. The pressure drag is generated largely by the after-body for most cars, with little contribution from the fore-body (Hucho & Sovran 1993) and is directly linked to the coherent structures in the vehicle wake (e.g. Beaudoin & Aider 2008). As such, the wake of three-dimensional (3D) vehicle models has caught considerable attention in the past because of its fundamental and engineering significance (e.g. Oertel 1990); a large number of experimental and numerical

investigations have been performed since the pioneer work of Janssen and Hucho (1974).

On the other hand, passenger cars and light commercial road vehicles are widely used in our life. Vehicular emission is one of the major sources of urban air pollution. Air pollutants are primarily from road traffic in many cities. Due to the high level use of diesel vehicles, diesel emissions become more serious in the cities such as Hong Kong. These pollutants are included two parts which are gaseous and particulate. These particulates are respirable and impact human health (Figler *et al*. 1996, Stober 1987).

Cyclone separators are most widely used in engineering as industrial gas-cleaning devices, e.g., vehicle exhaust-gas cleaning devices, vacuum cleaners, incinerators and boilers. The basic cyclone design has evolved little since its first application about one hundred years ago, largely attributed to the complexity and inadequate knowledge of the turbulent swirling flow and instabilities such as vortex breakdown and precessing vortex core within a cyclone. These instabilities are responsible for extra losses, producing a high pressure drop and a high level of turbulence and mixing in the cyclone (e.g. Biffin *et al*. 1984). As a result, there are problems in the use of cyclones. A typical example is the incorrect prediction of the separation efficiency of submicron particles in a common industrial cyclone separator. This calls for the need to gain an in-depth understanding of fluid dynamics, including the turbulent flow structure, which is crucial for improving the theoretical model of the separation efficiency (Bose *et al*. 2010).

1.2 Literature Review

1.2.1 Turbulent near wake of an Ahmed vehicle model

The so-called Ahmed body (Ahmed *et al.* 1984) is perhaps the most widely studied simplified car model, which is a 3D bluff body. The wake of this model is highly three-dimensional, unsteady, complex and complicated. Past experimental and numerical studies indicate three major components in its wake: a recirculation bubble over the rear slanted surface, longitudinal vortices originating from the two side edges or C-pillars of the surface and a recirculation torus in the base of the model (Ahmed *et al.* 1984, Brunn *et al.* 2007, Hucho & Sovran 1993, Sims-Williams 2001, Lienhart *et al*. 2003, and Kapadia *et al.* 2003).

Previous studies have greatly advanced our understanding of the flow structure behind the Ahmed model and meanwhile also raise some issues to be resolved. For example, the well-known wake structure model for $\alpha < 30°$, where α represents the rear slant angle of the Ahmed vehicle model, is characterized by one pair of counter-rotating longitudinal vortices (Hucho & Sovran 1993). However, Krajnovic *et al.*'s (2005) numerical simulation of the Ahmed vehicle model at $\alpha = 25°$ with $g/H = 0.174$, where g was the gap between the ground surface and the model underside and H was the model height, pointed to the presence of one more pair of counter-rotating longitudinal vortices near the lower corner of the side surface. This pair of vortices was experimentally observed by Strachan *et al*. (2007) based on LDA measurements, which were referred to as "lower vortices" to be distinguished from the C-pillar

vortices. This pair of lower vortices was not reported in earlier studies, for example, by Ahmed (1984), Sims-Williams & Duncan (2003) and Vino *et al.* (2005), who used a 10-hole directional probe and a five-hole probe, respectively, nor by Lienhart *et al*. (2003), who also used an LDA technique. The mechanism behind the lower vortex generation and the dynamic role of this vortex needs to be clarified. One may wonder whether this vortex has anything to do with the clearance or gap between the ground surface and vehicle underside due to the presence of wheels. Krajnovic & Davidson (2005b) observed flow separation at the leading lower edge of the vehicle model with $g/H = 0.174$, but not in their earlier studies of a similar vehicle model with $g/H = 0.08$ (Krajnovic & Davidson 2002, 2003). They subsequently linked the different observations to the clearance effect. So far, this effect on the vehicle aerodynamics has not been given adequate attention in the literature. Previous studies (e.g. Ahmed *et al.* 1984, Brunn *et al.* 2007, Hucho & Sovran 1993, Sims-Williams 2001, Lienhart *et al*. 2003, Kapadia *et al.* 2003) have mostly focused on the time-averaged flow field, with the instantaneous flow field examined only via flow visualization (e.g. Ahmed *et al.* 1984). The fluctuating flow field is almost completely overlooked. The instantaneous and fluctuating flow fields are crucial for a thorough understanding and control of the vehicle aerodynamics. Bearman (1997) measured using PIV the wake of a 1/8 scale fastback vehicle and noted a significant difference between time-averaged and unsteady flow structures behind the model. His time-averaged flow was consistent with earlier studies, showing one pair of counter-rotating longitudinal vortices; but the instantaneous flow showed many compact coherent structures that

occurred rather randomly in time and space, completely different from the time-averaged flow structure.

1.2.2 Turbulent flow structure and swirl number effect in a cylinder-on-cone cyclone

Early investigations of cyclones were based on measurements by Pitot static tubes (Linden 1949) and hot-wire anemometry (Ustimenko and Bukhman 1968). The investigations aimed primarily at understanding the turbulent flow structure and determining the most efficient shape of a cyclone. With the advent of nonintrusive LDA, there have been increasing experimental investigations of the gas flow in a cyclone in the last one or two decades (e.g. O'Doherty *et al*. 1991, Chanaud 1965, Cassidy and Falvey 1970, Gouldin *et al*. 1984, Harvey 1962, Sarpkaya 1971, Alekseenko *et al*. 1999, Derksen and Van den Akker 2000, Peng *et al*. 2001, Hoekstra *et al*. 1999). In spite of previous investigations, many aspects of fluid dynamics including the flow instabilities such as the vortex breakdown and precessing vortex core (PVC) within a cyclone have yet to be better understood. These instabilities will generate extra losses and produce a higher pressure drop in the cyclone. In term of particle separation, the PVC will cause a pressure fluctuation and associated high levels of turbulence and mixing in the cyclone (Biffin *et al*. 1984). As a result, there are problems with cyclones in engineering such as the incorrect prediction of the separation efficiency of submicron particles in common industrial cyclone separator (Yazdabadi *et al*. 1994). Previous investigations on PVC and associated instabilities

are mostly related to swirl burners (Schildmacher and Koch 2005) and generators (Czarny *et al*. 2002); there have been very limited reports on the PVC that occurs in a cyclone with a reverse flow.

The swirl flow in a cyclone separator is characterized by a strong tangential velocity component, a relatively small axial component and a very small radial component. One of the important characteristic parameters for the swirl flow or cyclone flow is the swirl number, *S*. In this thesis, the *S* is defined as the ratio of the averaged angular momentum to the averaged axial momentum of the flow times the inlet hydraulic radius of the cyclone. In isothermal operation, *S* is determined by the geometrical parameters of a cyclone, given by $\pi d_e R/2A$, where d_e is the diameter of the cyclone outlet, *R* is the radius of the cyclone cylindrical chamber, and *A* is the inlet area. The choice of *S* may affect the separation efficiency and the pressure drop of the cyclone. In general, a higher *S* increases the separation efficiency of heavy particles and also corresponds to a higher pressure drop.

Let us consider the swirl flow without inverse flow involved. Alekseenko *et al.* (1999) performed theoretical and experimental investigation of steady helical vortices in a swirl flow formed in a cylindrical chamber of square cross section. Five different swirl numbers from 1.0 to 3.8 were investigated. The Strouhal number, *St* ($\equiv f_{\text{prec}} 2R/U_{in}$, where f_{prec} is the precessing frequency of the vortex in the cyclone), was almost constant for the range of the inlet Reynolds number *Re* ($\equiv U_{in}2R/v$, where U_{in} is the inlet velocity, and *v* the kinematic viscosity of fluid) = 1.4 ~ 4.5 x 10^4, though exhibiting a dependence on *S*. Both Chao *et al.* (1991) and Alekseenko *et al.* (1999)

pointed out that the flow structure in a swirl flow depended on S as well as on Re and the conditions at the exit and the downstream geometry of a swirl tube. Lu *et al*. (2005) noted through large-eddy simulation that the swirl number played an important role in the development of the swirl flow in a swirl tube.

Flow in a cylinder-on-cone cyclone is interested in this thesis, which is another type of swirl flow, rather different from the swirl flow discussed above. This flow is associated with a reverse flow, while the other is not. For the convenience of discussion, we hereinafter refer to the former as the cyclone flow and the latter as the swirl flow, unless otherwise stated. The very presence of an inverse flow should make the dependence of the flow structure on S in the cyclone flow distinct from that in the swirl flow. A number of questions may naturally arise. How does the reverse flow in the cyclone influence the relationship between the cyclone flow structure and swirl number? There have been a number of numerical and experimental investigations on the turbulent flow structure in cyclones, for example, Zhou and Soo (1990) and Hsieh and Rajamani (1991), Cristea *et al*. (1994) and Derksen (2003). None of these investigations examined the effect of S on the flow. Another question is whether the dependence of St on S would be the same as in the swirl flow. Significant attention has been devoted in the literature to St in the cyclone flow because of its engineering significance. For example, a higher St of the cyclone flow is beneficial to enhancing the mixing of different phases in the cyclone. As a matter of fact, previous reports show a scattering in the St values. Hoekstra *et al.* (1999) found experimentally St = 0.6 in a cyclone at $Re = 2.5 \times 10^4$ and $S = 3.1$; however, Derksen & Akker (2000)

observed numerically a *St* of 0.53 at *Re* = 1.4 x 10^4 and *S* = 2.1, whose geometry was similar to that used by Hoekstra *et al*. Then, Hoekstra's (2000) measurements of *St* was 0.7 in a cyclone at *S* = 3.93 and a *Re* in the order of 10^5. Solero and Coghe (2002) measured St = 0.62 in a single phase gas flow at *S* = 2.39 and *Re* = 3.76 × 10^4 and 1.25 × 10^5. One question is inevitable: what causes the scattered observations in *St,* ranging from 0.53 to 0.70? Is it the variation in *S*? Different experimental conditions and uncertainties could not entirely account for the large disparity in measured *St*. Then, one wonders whether the scattered *St* is linked to the effect of the Reynolds number or the swirl number or both. The effect of the swirl number has not been previously investigated for the cyclone flow.

1.3 Objectives and work performed

With the issues identified in literature review in mind, this work sets out for two major aims. One is to gain a better understanding of the vehicle aerodynamics. This is done by investigating experimentally the flow structure around an Ahmed vehicle model with and without a gap, in terms of instantaneous and time-averaged velocity, vorticity, streamline, and Reynolds stresses. Two rear slant angles, i.e., 25º and 35º, were investigated, covering two distinct flow regimes. In view of a highly 3-D flow, the PIV measurements were conducted in three orthogonal planes behind the model with and without a clearance between the model and the wind tunnel wall. Specific objectives with this flow include:

(i) to gain through measurements a detailed picture of the flow structure

around Ahmed vehicle model;

(ii) to investigate the effect of the clearance between the model underside and the ground surface on the flow structure;

(iii) to provide the experimental data of the second order moments of fluctuating velocities as well as the mean velocity field for numerical modeling.

The other aim is to study experimentally the flow within a cylinder-on-cone cyclone that is characterized by a reverse flow in the core region. Measurements were conducted in an industrial cyclone model. The swirl number range examined was from 2.4 to 5.3, and the Reynolds number range was $3.7 \sim 7.4 \times 10^4$. Both PIV and LDA techniques were deployed to measure the flow. Specifically,

(iv) to improve our understanding of the turbulent flow structure in a cylinder-on-cone cyclone;

(v) to investigate the effect of the Reynolds number on the Strouhal number;

(vi) to determine the possible dependence of the flow structure, including the Strouhal number, on the swirl number.

1.4 Outline of the thesis

The work presented in the thesis consists technically of two parts. One is related to the flow structure around an Ahmed vehicle model with and without a gap, and the other is the turbulence in a cylinder-on-cone cyclone that is characterized by a reverse flow in the core region. The two parts are introduced in three chapters; with Introduction and Summary chapters, the thesis includes a total of five chapters.

Introduction to the thesis is Chapter 1. The turbulent flow structures behind the simplified Ahmed vehicle model are presented in Chapter 2, covering two distinct flow regimes as, viz. the rear slant angle $\alpha < 30^{o}$ and $\alpha > 30^{o}$. The results of the turbulent flow within a cylinder-on-cone cyclone are presented and discussed in Chapters 3 and 4. Finally, Summary and Conclusions are given in Chapter 5.

CHAPTER 2

TURBULENT NEAR WAKE OF AN AHMED VEHICLE MODEL WITH AND WITHOUT A CLEARANCE FROM WALL

2.1 Introduction

The global warming and lasting high fuel costs in the past few years highlight the necessity and urgency of drag reduction research for vehicles, which warrants a thorough understanding of the flow around vehicles because of a connection between the flow structure and aerodynamic drag. Past studies have unveiled that the pressure drag contributes predominantly to the total drag acting on vehicles, in particular at a high speed. The pressure drag is generated largely by the after-body for most cars, with little contribution from the fore-body (Hucho & Sovran 1993) and is directly linked to the coherent structures in the vehicle wake (e.g. Beaudoin & Aider 2008). As such, the wake of three-dimensional (3-D) vehicle models has caught considerable attention in the past because of its fundamental and engineering significance (e.g. Oertel 1990); a large number of experimental and numerical investigations have been performed since the pioneer work of Janssen and Hucho (1974).

The so-called Ahmed body (Ahmed *et al.* 1984) is perhaps the most widely studied simplified car model, which is a 3-D bluff body. The wake of this model is unsteady, very complicated, and highly 3-D. Past studies indicate three major components in its wake: a recirculation bubble over the rear slanted surface, longitudinal vortices originating from the two side edges or C-pillars of the surface and a recirculation torus in the base of the model. The strength and behaviors of the

three types of coherent structures and their interactions depend on the slant angle (α) of the upper rear surface of the model (e.g. Ahmed *et al*. 1984). Please refer to Figure 2-1 for the schematic of the coherent structures and Figure 2-2 for the definition of α and the coordinate system. At relatively small α, the flow is characterized by two counter-rotating longitudinal vortices (e.g. Brunn *et al.* 2007). The vortices produce drag on one hand and induce a downwash, which enhances flow attachment on the slanted surface, between them on the other hand. The net effect is a drag reduction. The minimum drag occurs at $\alpha = 12.5^{\circ}$. The flow at this rear slant angle appears to be "two dimensional" except in the vicinity of the two C-pillars of the surface. This is evident from the parallel isobars of static pressure running across the surface (Ahmed *et al*. 1984). Beyond $\alpha \approx 15°$, the flow over the rear slanted surface becomes highly 3-D. The pressure drag rises rapidly with increasing α and reaches the maximum at $\alpha = 30°$, where the two longitudinal vortices achieve their maximum strength. At $\alpha > 30°$, the flow is dominated by spanwise vortices with the longitudinal vortices burst, and the pressure drag falls despite a fully separated flow. Apparently, $\alpha = 30°$ is a division point for two distinct regimes (Hucho & Sovran 1993). The flow is highly sensitive to a small change in α at the critical configuration. This is evident in Sims-Williams's (2001) detailed study of the time-averaged and unsteady flow structures at $\alpha = 30°$ based on 5-hole probe and smoke flow visualization measurements.

Previous studies have greatly advanced our understanding of the flow structure behind the Ahmed model and meanwhile raised a number of issues to be resolved or

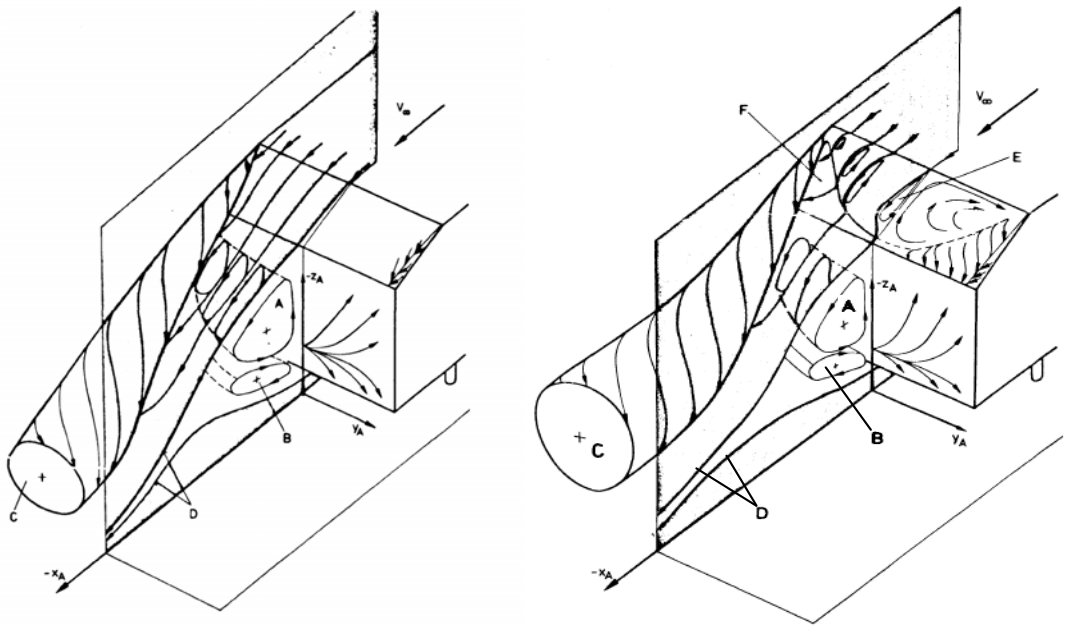

(a) (b)

Figure 2-1 Schematic of the flow structure behind a 3-D Ahmed vehicle model (from Ahmed *et al*. 1984): (a) $\alpha < 30°$, (b) $\alpha = 30°$, the high drag flow situation.

clarified. For example, flow structure models were proposed, which are different from the well known model shown in Ahmed *et al*. (1984). Vino et al. (2005) investigated experimentally flow structures in the near-wake of the Ahmed model ($\alpha = 30°$) using a 13-hole probe, which allowed reliable measurements in regions exhibiting large flow angles, including flow reversals. Their time-averaged results showed good agreement with previously published data at x/H = 1.09 but not at 0.044, much of the inconsistency being connected to interactions between the separated flow over the slant and the recirculatory flow in the vertical base of the vehicle model (Fig 2-1b). Their proposed flow structure model deviated from what Ahmed et al. (1984) suggested; their detached flow over the slant was not reattached, while the flow above the central region of the slant (Fig 2-1b) was characterized by a large separation bubble that reattached before separating again from the base. Based on their numerical

data, Krajnovic & Davidson (2005b) also questioned the correctness of Ahmed et al.'s flow structure model and even suggested that the pair of downstream longitudinal vortices did not stem from the shear layer rollup about the side edge of the slanted surface (their Fig 19).

Our knowledge of the instantaneous and fluctuating flow fields has yet to be improved, in particular, the higher order statistical moments of fluctuating velocities such as the Reynolds stresses. This knowledge is important for a thorough understanding and control of vehicle aerodynamics and also crucial for the validation of numerical models. Bearman (1997) measured using PIV the wake of a 1/8 scale fastback vehicle and noted a significant difference between time-averaged and unsteady flow structures behind the model. The instantaneous flow consisted of a substantial number of more compact coherent structures that occurred rather randomly in time and space, whilst the time-averaged flow was dominated by a pair of counter-rotating longitudinal vortices. Using LDA and hotwire, Lienhart & Becker (2003) measured rather extensively the higher order statistical moments of velocities as well as the mean velocities behind Ahmed vehicle model at α = 25° and 35°, though with little discussion of flow physics.

The well-known wake structure model for $\alpha < 30°$ is characterized by one pair of counter-rotating longitudinal vortices. However, Krajnovic *et al.*'s (2005) numerical simulation of the Ahmed vehicle model at α = 25° with g/H = 0.174 pointed to the presence of one more pair of counter-rotating longitudinal vortices near the lower corner of the side surface, though Krajnovic *et al.* considered the vortices to be too

weak to be of aerodynamic significance. In this Chapter, g denotes the gap separation between the ground surface and the model underside and H represents the model height. Strachan *et al*. (2007) measured using laser Doppler anemometry (LDA) time-averaged velocities behind an Ahmed vehicle model of $\alpha = 0° \sim 40°$, which was supported on an overhead aerodynamic strut. They observed at $g/H = 0.174$ a shear layer near the lower side edge of the model, thus also inferring the presence of one pair of counter-rotating longitudinal vortices, which were referred to as "lower vortices" to be distinguished from the C-pillar vortices. This pair of lower vortices was not reported previously, for example, by Ahmed et al. (1984), Sims-Williams & Duncan (2003) and Vino *et al.* (2005), who used a 10-hole, a 5-hole and a 13-hole directional probe, respectively, nor by Lienhart *et al*. (2003), who also used an LDA technique. Strachan *et al*. ascribed this discrepancy to the use of cylindrical struts used in the earlier investigations and suggested that the struts suppress the formation of the lower vortices. This has been demonstrated to be incorrect in the present investigation. The mechanism behind the lower vortex generation and the dynamic role of this vortex needs to be clarified.

One may wonder whether the discrepancy mentioned above has anything to do with $g/H \neq 0$ due to the presence of wheels. Krajnovic & Davidson (2005b) observed flow separation at the leading lower edge of the vehicle model with $g/H = 0.174$, but not in their earlier studies of a similar vehicle model with $g/H = 0.08$ (Krajnovic & Davidson 2002, 2003). They subsequently linked the different observations to the clearance effect. So far, this effect on the vehicle aerodynamics has not been given

adequate attention in the literature.

With the above issues identified in mind, the first objective of this work is to gain through measurements a better picture of the flow structure around the Ahmed vehicle model; the second is to investigate the effect of the clearance between the model underside and the ground surface on the flow structure; the third is to provide the experimental data of the second order moments of fluctuating velocities as well as the mean velocity field for numerical modelling. Two configurations, i.e., $\alpha = 25^{\circ}$ and 35°, were investigated, corresponding to the two distinct flow regimes (Ahmed et al. 1984, Hucho & Sovran 1993). In view of a highly 3-D flow, the PIV measurements were conducted in three orthogonal planes behind the model with and without a clearance between the model underside and the wind tunnel wall. Based on the data obtained, the instantaneous and time-averaged flow fields are examined and discussed, along with the Reynolds normal and shear stresses and also published results, including the variants of proposed flow structure models.

2.2. Experimental details

2.2.1 Wind tunnel and vehicle model

Experiments were carried out in a closed circuit wind tunnel with a 2.4-m-long square test section (0.6 m x 0.6 m). The flow non-uniformity in the test section is 0.1% and the streamwise turbulence intensity is less than 0.4% in the absence of the vehicle model for the velocity range examined presently. The working section wall was made of optical glass in order to enhance the signal-to-noise ratio in PIV measurements. See Huang et al. (2006) for more details of the tunnel. The dimensions

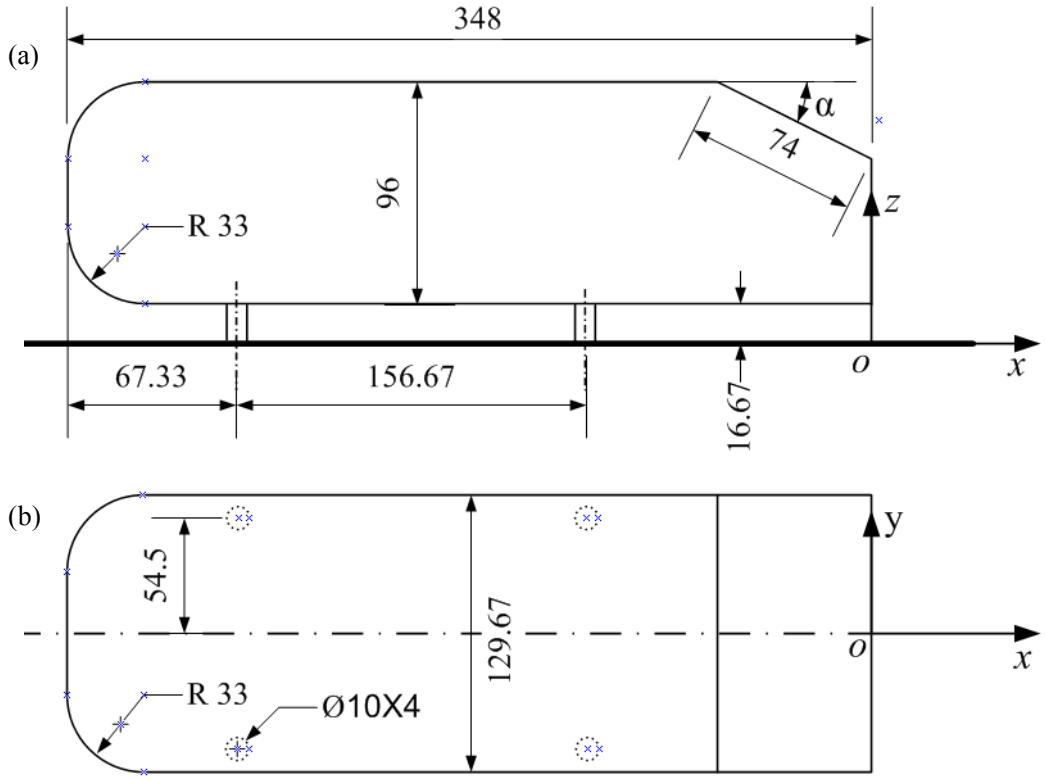

Figure 2-2 Dimensions of the scaled-down Ahmed vehicle model and the definition of the coordinate system: (a) side view, (b) plan view.

of a 1/3-scaled Ahmed vehicle model are given in Figure 2-2. Two angles, i.e. $\alpha = 25°$ and 35°, were investigated. The model is 0.348 m in length (L), 0.13 m in width (B), and 0.096m in H. The four wheels of the model were simulated by four 16.67-mm-tall struts with a diameter of 10 mm. Measurements were conducted at a free-stream velocity of U_∞= 8.33 m/s, corresponding to a Reynolds number, $Re_H \equiv U_\infty H/\nu = 5.26\times10^4$, where ν is the kinematic viscosity of air. The model was placed on a flat plate (length x width x thickness = 2 m x 0.59 m x 0.02 m), with its front end at 0.3 m downstream of the leading edge of the plate. The blockage ratio of the frontal surface of the model to the rectangular test section above the flat plate was around 4.1%, not exceeding 5%, a suggested limit beyond which the blockage effect cannot be neglected (Farell et al. 1977). The leading edge of the plate was a clipper-built curve,

following Narasimha and Prasad's (1994) design, to avoid flow separation. The coordinate system (Fig 2-2), follows the right-hand rule and is defined such that x, y and z are directed along the mean flow, vertical (transverse), and spanwise directions, respectively. In this Chapter, asterisk denotes normalization by H and/or U_∞, e.g. $x^*= x/H$, $y^* = y/H$ and $z^* = z/H$.

2.2.2 Documentation of boundary layer

The boundary layer over the plate may have an effect on the flow structure around a finite-height bluff body (Wang et al. 2006). It is therefore important to document the conditions of the boundary layer, where the model was placed. An LDA system (Dantec Model 58N40) with an enhanced flow velocity analyzer was used to measure the mean and root mean square (rms) value of the streamwise velocity, i.e., $\overline{U}$ and u_{rms}, measured at 0.3 m from the leading edge of the plate in the plane of symmetry. The flow was seeded by smoke generated from paraffin oil with an averaged particle size of around 1μm in diameter. The measuring volume of the LDA system had a major axis of 2.48 mm and a minor axis of 1.18 mm. More than 5,000 instantaneous samples were collected at each point. The measurement results were given in Figure 2-3. Experimental uncertainties were estimated to be within 2.9% in $\overline{U}$ and 3.9% in u_{rms}. The disturbance thickness of the boundary layer was about 4 mm (i.e., 0.036H), estimated from the $\overline{U}$ distribution. Such a thin boundary layer should produce a negligibly small effect on the flow structure.

2.2.3 PIV measurements

A DANTEC standard PIV system was used to measure flow around the Ahmed

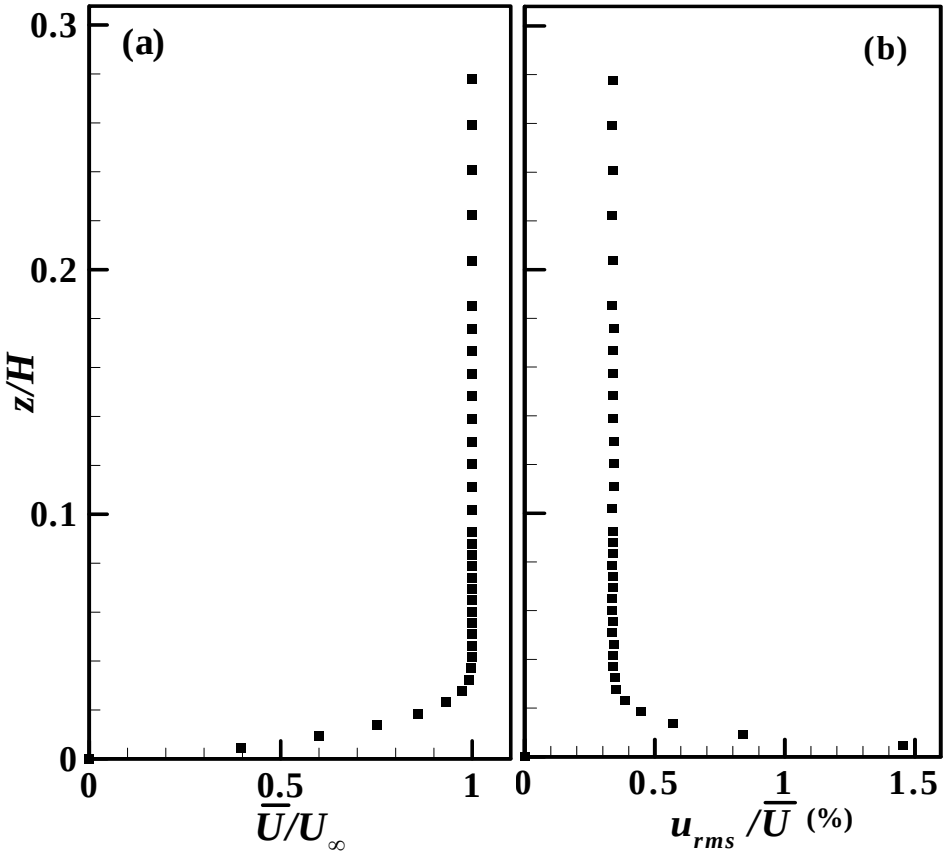

Figure 2-3 The distributions of mean and rms streamwise velocities in the boundary layer over the flat plate at 0.3 m from the leading edge of the plate (y^* = 0, U_∞= 8.33 m/s).

model with and without the four struts (wheels), i.e. g^* = 0.174 and 0, in order to understand the effect of the clearance between the model underside and wall on the flow structure. The schematic of experimental setup is shown in Figure 2-4. The same seeding was used as in the LDA measurement. Flow illumination was provided by two Newwave standard pulsed laser sources of 532nm wavelength, each with a maximum energy output of 120mJ/pulse. Each laser pulse lasted for 0.01 μs. Particle images were taken using a CCD camera (HiSense type 4M, double frames, 2048×2048 pixels). Synchronization between image taking and flow illumination was provided by the Dantec FlowMap processor (System HUB).

The flow is highly three-dimensional (e.g. Ahmed et al. 1984). In order to

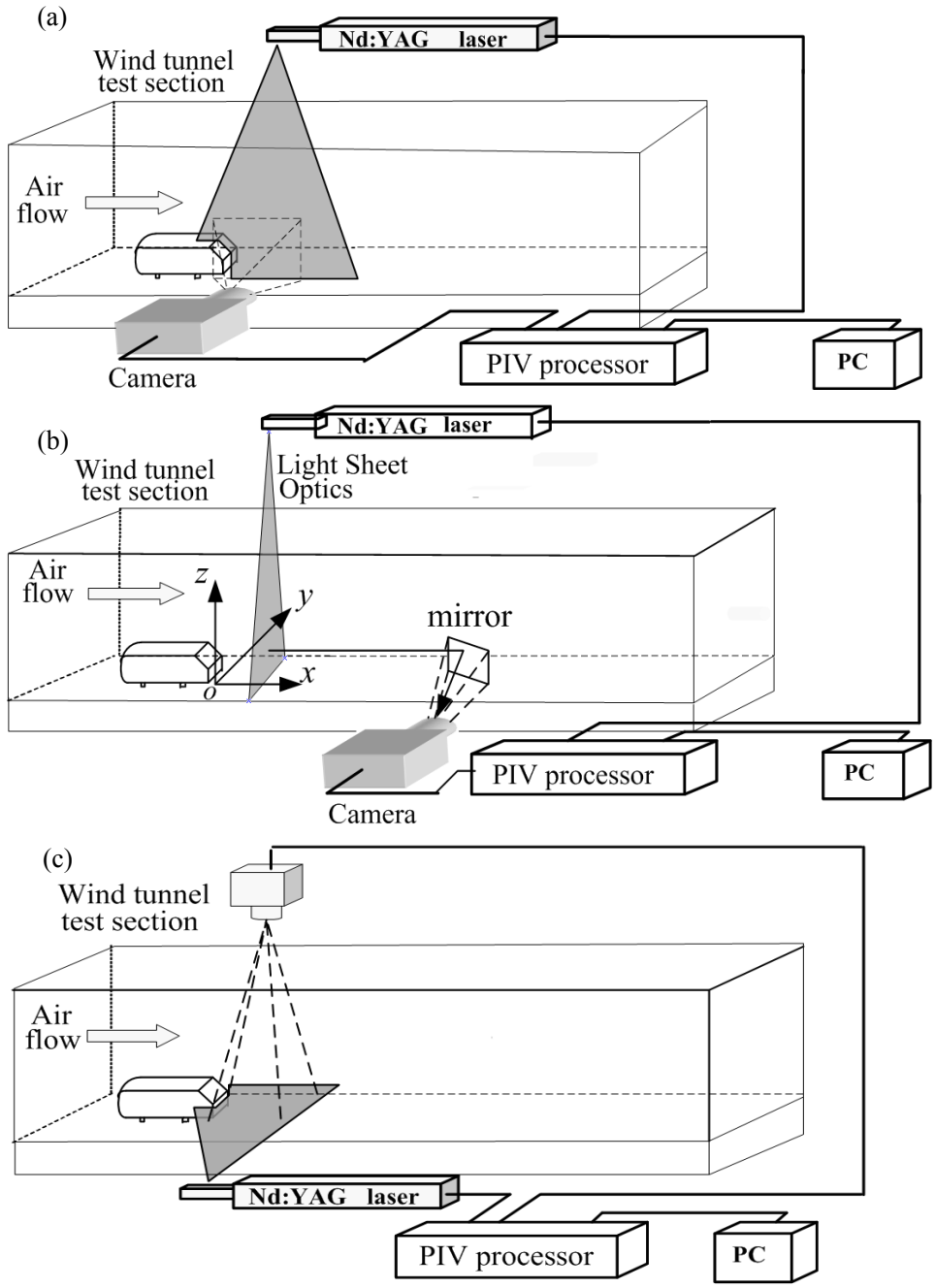

Figure 2-4 PIV measurement arrangements in (a) the *x*-*z* plane, (b) *y*-*z* plane, and (c) *x*-*y* plane**.**

capture accurately the flow structure, one should ideally conduct measurements around the model in a large number of planes along each of the *x*, *y* and *z* directions. This is unpractical because of the demands for a tremendous storage space of data and also an exhaustive amount of time and effort for data analysis. Therefore, PIV measurements were performed in a limited number of planes, including the *x*-*z* plane

at $y^* = 0$ (symmetry plane), the *x*-*y* plane at mid-height of the model from wall, i.e. $z^* = 0.67$ at $g^* = 0.174$ or $z^* = 0.5$ at $g^* = 0$, and the *y*-*z* plane at $x^* = 0.23$ and 5.80, one in the near wake and the other in the far wake, i.e., within and outside the recirculation region, respectively. Different measurement planes are illustrated in Figure 2-4. For the measurements in the *y*-*z* plane, a mirror of 120 mm ×120 mm was vertically placed at $x/H = 15$ in the tunnel, whose normal direction was 135° from the x axis. At such a distance downstream of the PIV imaging plane, the camera should have a negligibly small effect on measurement (Zhang *et al*. 2006). The PIV images covered an area of 2.4H × 2.4H ($x^* = -0.6 \sim 1.8$, $z^* = -0.15 \sim 2.25$), 2.4H × 2.4H ($y^* = -1.2 \sim 1.2$, $z^* = -0.2 \sim 2.2$), and 1.96H × 1.96H ($x^* = -0.06 \sim 1.9$, $y^* = -0.98 \sim 0.98$) for the *x*-*z*, *y*-*z* and *x*-*y* planes, respectively. The image magnifications in both directions of the plane were identical, ranging from 103 to 113 μm/pixel. The interval between two successive pulses was set at 50 μs for measurements in the *x*-*y* and *x*-*z* planes, during which fluid particles may travel a distance of 0.42 mm at $U_\infty = 8.33$ m/s. Following Huang et al. (2006), the laser sheet was made thicker for measurements in the *y*-*z* plane, i.e., 3 mm (cf. 1.0~1.5 mm in the *x*-*y* and *x*-*z* planes) in order to capture the maximum number of seeding particles during each pulse.

In processing PIV images, 32 × 32 interrogation areas were used with a 50% overlap in each direction, producing 127 × 127 in-plane velocity vectors and the same number of vorticity components $\Omega_x = \overline{\Omega_x} + \omega_x$, $\Omega_y = \overline{\Omega_y} + \omega_y$ or $\Omega_z = \overline{\Omega_z} + \omega_z$ in the x, y and z directions, respectively, where overbar denotes time-averaging and ω_x, ω_y and ω_z are the fluctuating vorticity components, respectively. The vorticity data

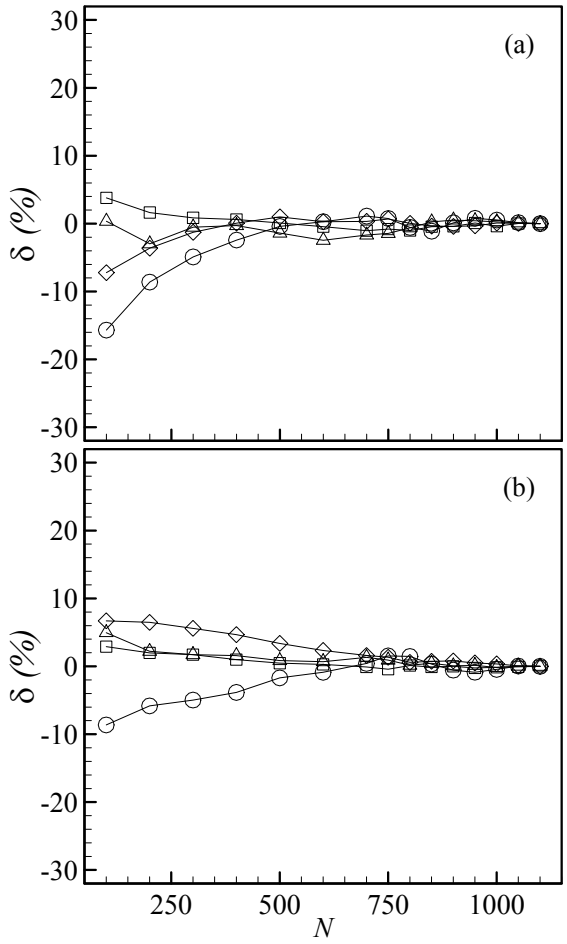

Figure 2-5 Dependence of $\delta = \frac{\beta_N - \beta_{N-\Delta N}}{\beta_N} \times 100\%$ on the number (N) of the PIV images captured in the x-z plane, where β denotes U_{mean} (□), u_{rms} (Δ), W_{mean} (◊) or w_{rms} (O) measured at $x^* = 0.23$, $y^* = 0$, $z^* = 0.4$: (a) α = 25°, (b) 35°. The maximum N is 1100; $g^* = 0.174$.

was calculated by a built-in function of the FlowMap Processor based on eight surrounding velocity data. The spatial resolution of vorticity data was about 1.81 mm, 1.81 mm and 1.66 mm for the x-z, y-z, and x-y planes, respectively.

A total of 1100 PIV images were captured in each plane. The number of images has to be adequate for both mean and fluctuating flow fields. Figure 2-5 presents the dependence of $\delta = \frac{\beta_N - \beta_{N-\Delta N}}{\beta_N}$ on N, where β denotes $\overline{U}^*$, $\overline{W}^*$, u^*_{rms} or w^*_{rms},

subscript N *or* N - ΔN is the number of images (ΔN is the increment in N). The velocity data was obtained with $g^* = 0.174$ at (x^*, y^*, z^*) = 0.23, 0, 0.4 in the x-z plane. The parameter δ provides a measure of the dependence of experimental uncertainties on N. Apparently, with increasing N, δ converges rapidly to less than ±1% at $N \approx 700$ at $\alpha = 25°$ or 35° for all the quantities. Similar results have been obtained at other locations, thus demonstrating that 1100 images are adequate presently.

2.3. Longitudinal structures

2.3.1 Time-averaged flow

The wake of the Ahmed vehicle model is characterized by predominantly longitudinal structures that play a crucial role in determining aerodynamic forces (e.g. Ahmed et al. 1984). Naturally, the longitudinal structures have been a focus in previous experimental investigations, most of which were performed based on time-averaged data perhaps due to a limitation in measurement techniques. As such, time-averaged data is presently examined first to facilitate data comparison and interpretation. Figure 2-6 compares the iso-contours of $\overline{\Omega_x^*}$, in the y-z plane at $x^* =$ 0.23 with and without a gap of $g^* = 0.174$ for $\alpha = 25°$ and 35°. The same cutoff contour level and increment are used in the four plots of Fig 2-6 and those following to facilitate comparison. The flow structure appears highly complicated, displaying many vorticity concentrations, as noted by Bearman (1997). A close inspection of the contours unveils interesting details on the flow structure, as well as the major flow characteristics that conform to previous numerical and experimental studies (Ahmed

et al. 1984, Lienhart *et al*. 2003, Sims-Williams *et al.* 2001, Krajnovic & Davidson 2005, Vino *et al.* 2005 and Minguez *et al*. 2009**)**.

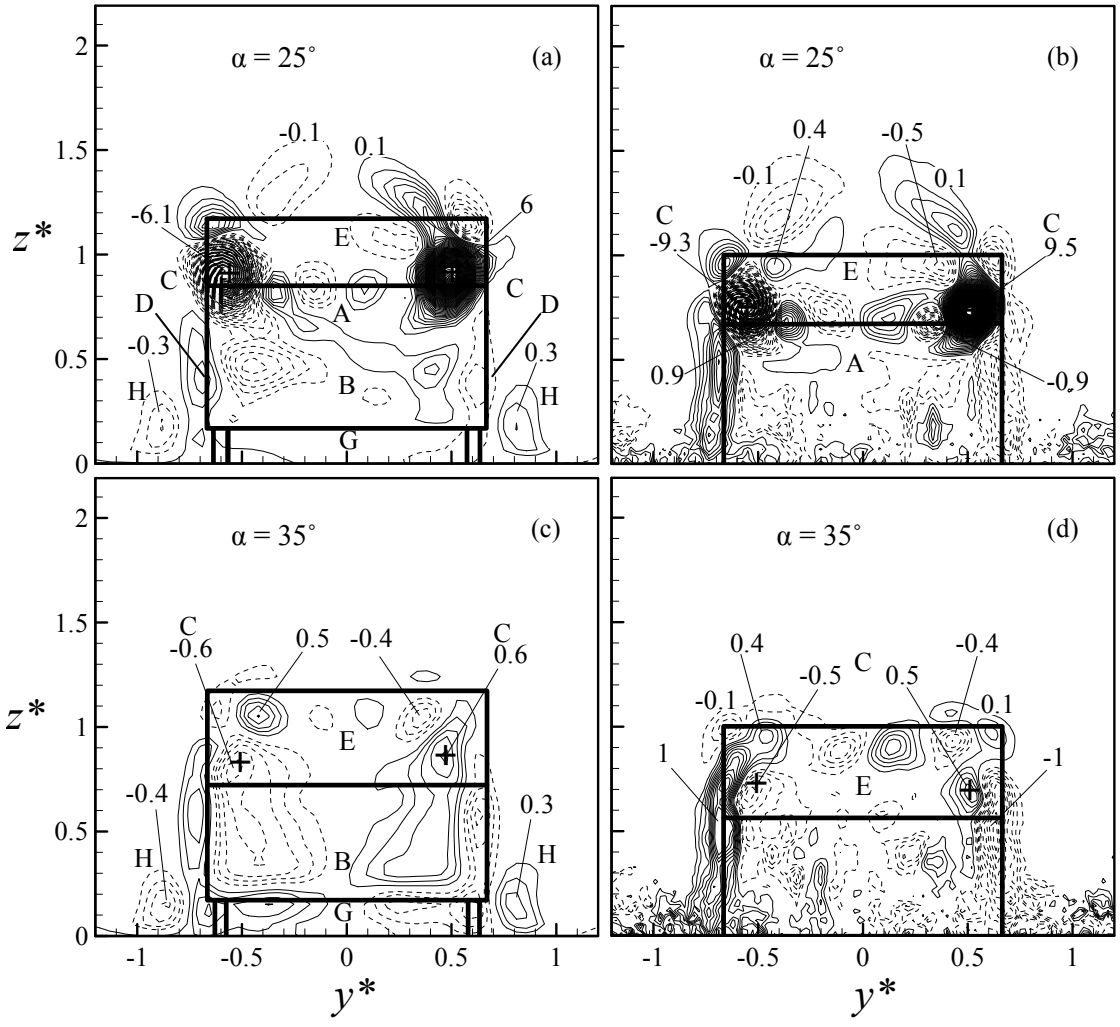

Figure 2-6 Iso-contours of averaged streamwise component, $\overline{\Omega_x}^*$, of vorticity in the *y*-*z* plane at $x^* = 0.23$ ($Re_H = 5.26\times10^4$): (a, c) $g^* = 0.174$, (b, d) $g^* = 0$. The contour interval is 0.1 and the cutoff level is ± 0.1.

At $\alpha = 25°$ (Figure 2-6a), a number of observations can be made. Firstly, the two most concentrated longitudinal vortices, marked by "C", are well known C-pillar vortices. Their centres are located at (y^*, z^*) ≈ (- 0.56, 0.9) and (0.52, 0.9), respectively. With flow blowing over the vehicle body, the shear layers over the C-pillars roll up into the longitudinal or C-pillar vortices. Secondly, there are many vorticity concentrations behind the model vertical base, which tend to be aligned in

two rows, one at the same level of the upper edge of the base and the other right above the lower edge. These structures probably result from the shear layer separation from the upper and lower edges, that is, they are associated with the two recirculatory bubbles, one above the other, and referred to as vortices "A" and "B" in Ahmed *et al*. (1984). The signs of the structures near the upper edge tend to occur alternately, which have not been reported previously and will be discussed later in detail together with instantaneous vorticity contours. Thirdly, the central region "E" of the slant surface is not associated with large vorticity concentrations. This should be reasonable. Compared with the case of $\alpha < 12.5°$ where flow over the slant surface is rather two-dimensional (2-D) and fully attached to the surface (Ahmed et al. 1984), the two longitudinal vortices for $12.5° < \alpha \leq 30°$ grow in size, resulting in a 3-D flow over the slant surface and meanwhile maintaining attached flow to the central section of the surface (e.g. Strachan *et al*. 2007). Fourthly, a number of concentrations show up above the C-pillar vortices. As will be seen later from the data in the *x*-*z* plane, the shear layer developed over the top surface of the model does not entirely remain attached to the slant; rather, part of it shoots over, deviating only slightly from the horizontal direction. The detached shear layer, under the rolling effect of C-pillar vortices, is probably responsible for the concentrations. Fifthly, Figure 2-6a displays one additional pair of counter-rotating longitudinal vortices, marked by "H", which occur near the lower corners of the model, one at $(y^*, z^*) \approx (-0.88, 0.16)$ and the other at $(y^*, z^*) \approx (0.80, 0.16)$. Their maximum concentration is about 5% of the C-pillar vortex. Most previous measurements using multi-hole probes, hotwires or LDA failed

to capture the two vortices. The first observation was made by Krajnovic *et al.* (2005) based on their LES data at α = 25°, who considered the vortices to be too weak to be of any aerodynamic significance. Stranchen *et al*. (2007) made a similar observation based on their LDA data. With their model supported by a single overhead strut, they ascribed the generation of the vortices to four cylindrical struts used in many earlier measurements. A different opinion is offered here. The presence of the boundary layers formed on the wall and the model underside decelerates fluid and hence increases the pressure of the gap flow. The iso-contours of the averaged transverse velocity $\overline{V^*}$ in the *y*-*z* plane (not shown) indicate a flow squeezed out of the gap, that is, the pressure difference between flow inside the gap and that outside induces the rollup of fluid, forming longitudinal vortices in a manner similar to the C-pillar vortices. The vortices are presently referred to as the lower vortices, following Stranchen *et al*. (2007). The lower vortices are predominantly longitudinal. As a matter of fact, supplementary PIV measurements (not shown), conducted in the *x*-*z* plane at *y** = -0.57 and -0.77, failed to capture any appreciable vorticity concentration at the position where the lower vortices occur. Finally, there is one stretched vorticity concentration, marked by "D", along each side surface of the model, which is probably due to the shear layer developed over the side surface of the model.

In the absence of the gap, i.e., g^* = 0 (Fig 2-6b), there is a marked change in the flow structure. The most noticeable is perhaps the absence of the lower vortices "H", corroborating our proposition on their generation mechanism. The maximum vorticity concentrations of the C-pillar vortices "C" are increased by about 50%, though the

vortex size shrinks. The vorticity concentrations generated by flow separation from the upper edge of the base, associated with recirculatory bubble "A", are evident and again occur alternately in sign. On the other hand, the lower row of concentrations could not be seen. This is reasonable since the recirculatory bubble "B" results largely from the shear layer separating from the lower edge of the vertical rear base and upwash flow (Ahmed *et al*. 1984, Sims-Williams & Duncan 2003, Vino *et al*. 2005). Finally, the stretched concentrations "D" are enhanced in both size and the maximum vorticity. The changes suggest that the gap has a considerable influence on the wake and hence aerodynamics of ground vehicles.

At $\alpha = 35°$, flow separates from the upper edge of the rear slant surface, and the C-pillar vortices burst (Ahmed *et al.* 1984). This is reflected in Fig 2-6c. Firstly, there is one row of vorticity concentrations, again alternately arranged in sign, right below the upper edge of the slant. They result from flow separation and are brought down by downwash flow. Secondly, the maximum vorticity concentration of vortices "C" diminishes to about 10% of its counterpart at $\alpha = 25°$ (Fig 2-6a). The vortices further exhibit a significant reduction in size, though appearing enlarged due to their merging with concentrations in the base. The observation is consistent with Ahmed *et al*.'s (1984) report that the separation region or half elliptic recirculation flow on the slant surface joined the separation bubble of the base so that bubbles "A" and "E" could no longer be considered to be separate. Note that the maximum concentration of the lower vortex "H" retains its level at $\alpha = 25°$ and now amounts to about 50% of the C-pillar vortex. Naturally, its dynamic role may not be necessarily negligible. There is

one pair of vortices “G” between the wall and the model underside, apparently linked to the shear layer developed in the gap and hence called the gap vortex. The gap vortex could not be seen in Fig 2-6a. As will be shown later, the downwash flow is markedly stronger at α = 25° than at α = 35°, thus keeping the gap vortices down, without being captured.

In the absence of the gap (Fig 2-6d, α = 35°), the row of alternately signed vorticity concentrations, resulting from shear layer separation from the slant surface, appears enhanced in strength, albeit slightly. The concentrations “D” are also strengthened. On the other hand, the C-pillar vortex is further impaired in both the maximum vorticity and size, compared to Fig 2-6c. So are the concentrations associated with the separation bubble in the model vertical base.

2.3.2 Instantaneous flow

Most of previous investigations are focused on time-averaged flow field around Ahmed vehicle model for various reasons. Many important details of the flow field could be lost or buried in the time-averaging process. There have been efforts in performing oil or smoke flow visualization to complement the data of time-averaged flow field (e.g. Ahmed *et al*. 1984, Lienhart & Becker 2003, Vino *et al*. 2005). These efforts provide flow pictures on the model surface or in the *x*-*z* plane and indeed further our understanding of flow physics. The present PIV measurements in three orthogonal planes provide us with a great opportunity to explore instantaneous flow structures off the vehicle model, in particular, in the *y*-*z* plane.

Figure 2-7 illustrates typical iso-contours of instantaneous streamwise vorticity

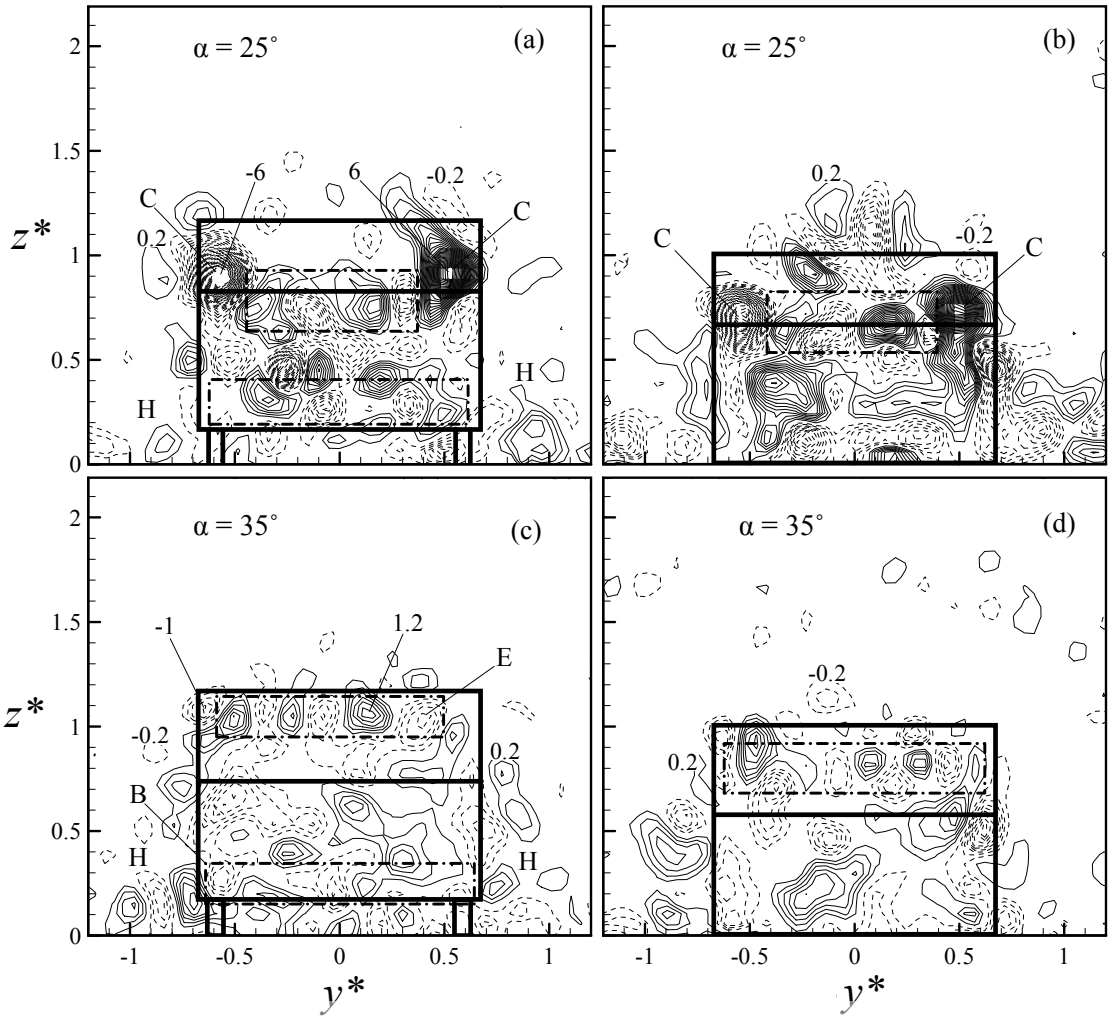

Figure 2-7 Iso-contours of instantaneous streamwise component, Ω_x^*, of vorticity in the *y*-*z* plane at $x^* = 0.23$ ($Re_H = 5.26\times10^4$): (a, c) $g^* = 0.174$, (b, d) $g^* = 0$. The contour interval is 0.2 and the cutoff level is ± 0.2.

Ω_x^* in the *y*-*z* plane at $x^* = 0.23$. Apparently, the instantaneous flow structure is highly complicated; the base region is packed with the vortical motions or vorticity concentrations of various scales. Nevertheless, a close inspection allows us to connect these motions to the major features shown in Figure 2-6. The C-pillar vortices are easily identified in Fig 2-7a and 7b with the pair of the most highly concentrated counter-rotating large-scale concentrations. The lower vortices are also discernible in Fig 2-7a and 7c. Note that in the absence of the clearance the vorticity concentrations (Fig 2-7b) may occur near the lower corners of the model. However, their signs

appear rather random, that is, these concentrations tend to cancel out each other in the averaging process, explaining the absence of the lower vortex in Fig 2-6b and 6d.

It is of interest to note that one row of four alternately signed vorticity concentrations occur between the C-pillar vortices in Fig 2-7a and 7b, corresponding reasonably well to the concentrations between the C-pillar vortices in Fig 2-6a and 6b. Absence of a negative concentration between the positive C-pillar vortex and the positive concentration at $(y^*, z^*) \approx (0.1, 0.85)$ in Fig 2-6a is probably due to cancellation by the random change in the size of the positive C-pillar vortex. The row of alternately signed vorticity concentrations near the lower edge of the base in Fig 2-7a is also interesting, which may be associated with the recirculatory bubble "B" in the time-averaged flow field. These structures appear smaller scaled than those right below the upper edge of the base. At $\alpha = 35°$, flow separates from the upper edge of the slant, not the upper edge of the base (Ahmed *et al*. 1984). Therefore, the alternately signed structures could not be seen near the upper edge of the base but are evident right below the upper edge of the slant (Fig 2-7c, 7d). These structures are again of relatively small scales. One is naturally tempted to beg the question: why do the structures associated with the recirculatory bubbles "A" and "B" tend to occur alternately in sign, which has been confirmed by many plots of instantaneous Ω_x^*-contours we have inspected?

It has been established that the recirculatory bubbles "A" and "B" result from spanwise shedding from the vertical base (e.g. Ahmed *et al*. 1984). Such spanwise structures should be nominally 2-D in the central section, though highly 3-D near their

ends. Vino *et al*. (2005) measured surface pressure and all three fluctuating components of flow velocity around an Ahmed model at Re_H = 1.2 x 10^5. The spectra of the pressure and velocity signals displayed a pronounced peak at a Strouhal number of about 0.11 based on H, demonstrating unequivocally the presence of quasi-periodical structures. Furthermore, this peak is by far stronger for the streamwise and transverse fluctuating velocities than for the spanwise component, suggesting that the coherent structures were predominantly spanwise oriented. The formation nature of the structures, along with their behaviours, prompts us to connect the structures with the Karman vortex street behind a 2-D bluff body. The latter flow has been extensively studied in the literature and many aspects of it are well understood. It is now well known that two major types of vortical structures occur in this flow, i.e., the nominally 2-D spanwise structures and the predominantly longitudinal rib structures (e.g. Zhou & Antonia 1994, Zhang *et al*. 2000). Evidently, the streamwise vorticity concentrations observed in the base (Figs 2-6a or 2-7a) could be a manifestation of the longitudinal rib vortices. There is another possibility. Flow visualizations (Wu *et al*. 1996, Williamson 1996) point to a waviness of the spanwise structures. This has been confirmed by direct numerical simulation (DNS) data (Thompson *et al*. 1994, Zhang *et al*. 1995). The spanwise structures can be shed in either parallel or oblique modes (Williamson 1996). All of these features, *inter alia*, could be associated with the flow structure separated from the upper and lower edges of the base. In view of the end effects, in particular, the induction effect of the two C-pillar vortices, the scenario of wavy spanwise rolls is considered to be more likely

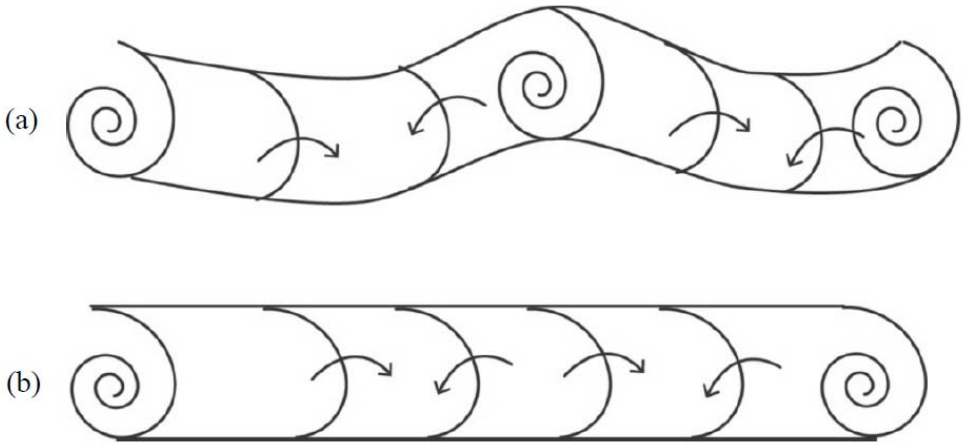

Figure 2-8 schematic of the two scenarios of the spanwise roll: (a) wavy spanwise roll, (b) spanwise roll, both wrapped with rib structures.

for the alternately signed structures separated from the upper edge of the base. On the other hand, the rib structures wrapped with a spanwise structure could explain the structures near the lower edge of the base and the upper edge of the slant. We will come to this point again when discussing transverse structures in Section 5. On the basis of the present data and previous observations, the schematic representations of the two scenarios are constructed in Fig.2-8. For simplicity, the spanwise rolls are drawn with a circular cross-section. The actual spanwise structures could be elliptical or other shapes.

Figure 2-9 presents the iso-contours of the averaged vertical velocity, $\overline{W}^*$, in the *y-z* plane at $x^* = 0.23$. The centres of the C-pillar vortices have been marked by a cross in Figures (2-9)~(2-11) to facilitate interpretation. At $\alpha = 25°$, the negative contours overwhelm over the slant surface, due to the attached downwash flow, and the upper part of the base because of flow separation from the upper edge of the base. The negative contours are flanged by positive concentrations, apparently linked to the

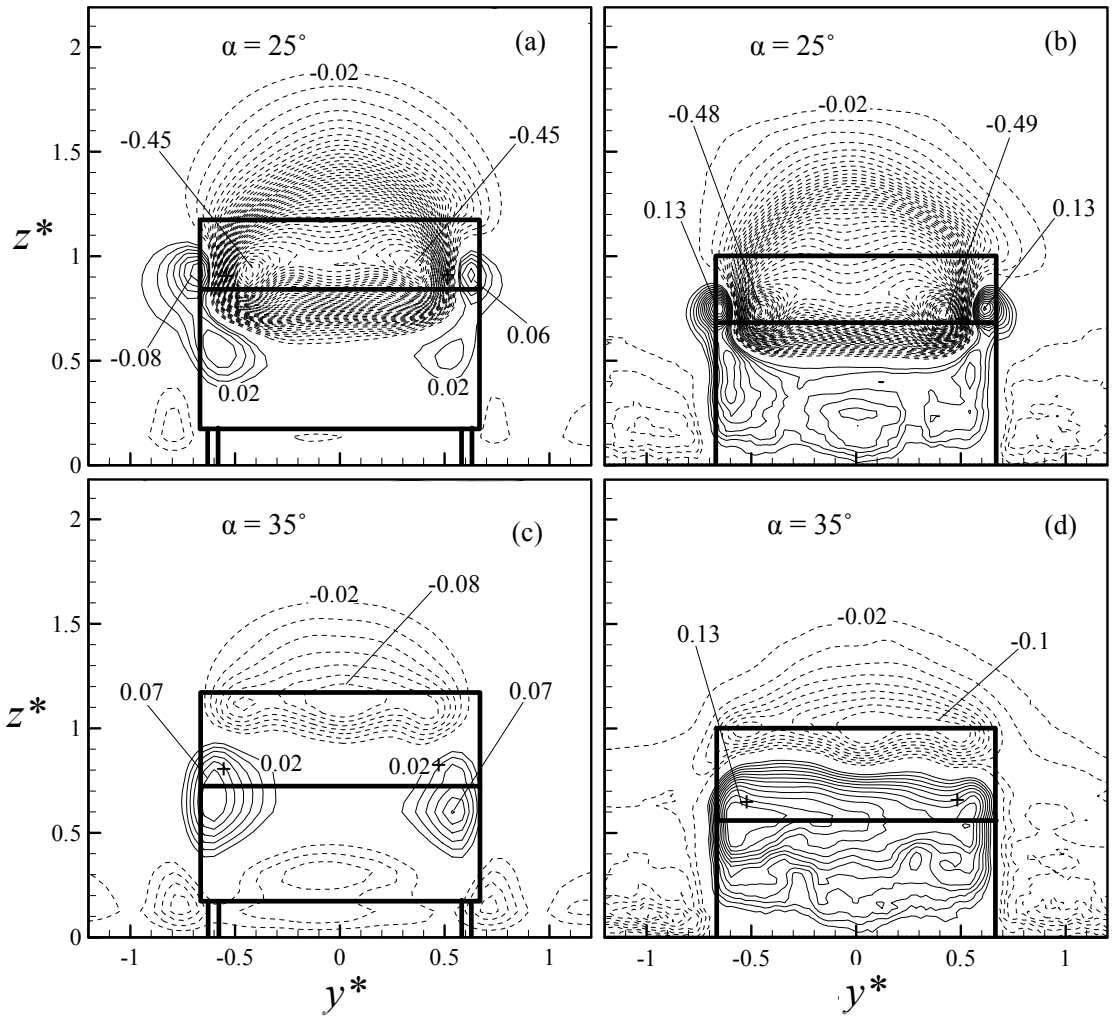

Figure 2-9 Iso-contours of the averaged vertical velocity, $\overline{W}^*$, in the *y*-*z* plane at *x** = 0.23 (Re_H = 5.26×10^4): (a, c) *g** = 0.174, (b, d) *g** = 0. The contour interval is 0.01 and the cutoff level is ± 0.02.

C-Pillar vortices and the recirculatory bubbles. In the absence of the clearance, the positive concentration is strengthened in the lower base region, due to an upwash flow induced by downwash flow within the recirculation bubble; on the other hand, the negative concentration is enhanced on both sides of the model. At α = 35°, downwash flow is greatly weakened with a separation bubble formed over the slant surface. The negative contours in the lower part of the vertical base are probably induced by the vortices resulting from merged C-pillar and recirculatory vortices "B". Without the clearance, the positive contours are extended into the lower half of the slant surface.

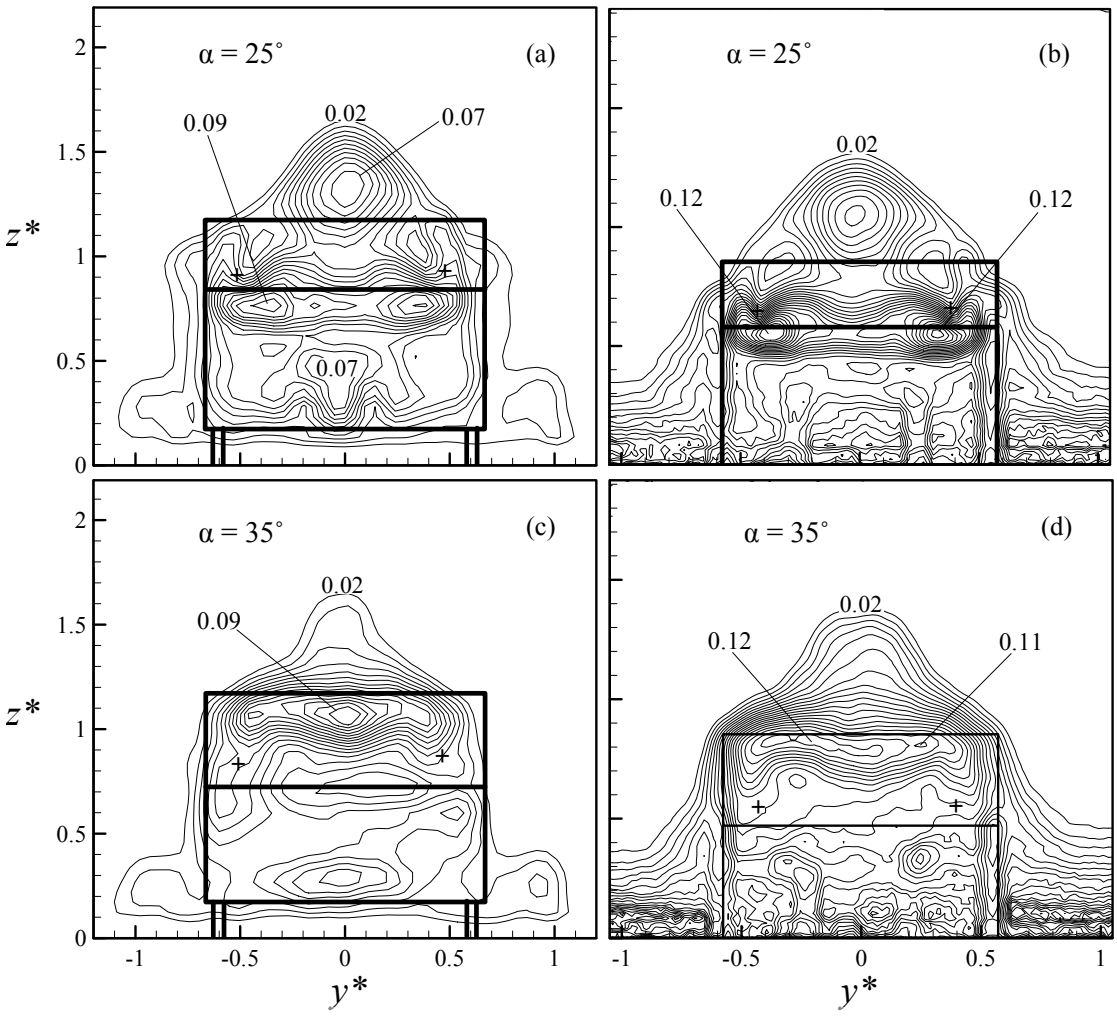

Figure 2-10 Iso-contours of the rms vertical velocity, w^*_{rms}, in the *y*-*z* plane at *x** = 0.23 (Re_H = 5.26×10^4): (a, c) *g** = 0.174, (b, d) *g** = 0. The contour interval is 0.005 and the cutoff level is ± 0.02.

The iso-contours of the root-mean-square value, w^*_{rms}, of the vertical velocity at α = 25° (Figure 2-10a) show two concentrations near the two upper corners of the vertical base, produced by the two C-pillar vortices. The contours are also of relatively high level about the upper and lower edges of the base, resulting from flow separation from the two edges which produces two rows of alternately signed longitudinal vortices in addition to spanwise coherent structures. The two concentrations near the lower corners of the base stem evidently from the lower vortices. Note that the concentration of the w^*_{rms} contours that occurs above the central

region of the upper edge of the slant surface results from the shear layer developed

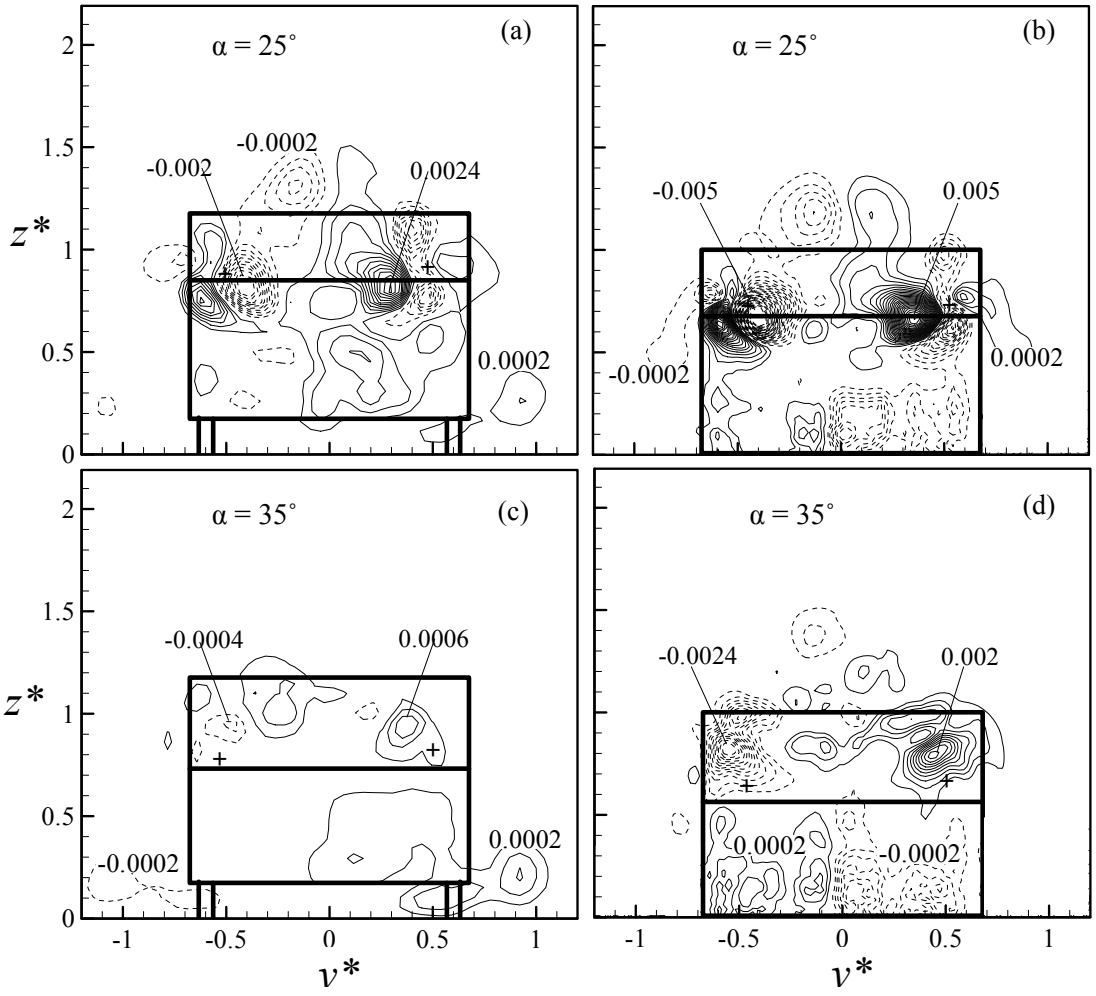

Figure 2-11 Iso-contours of the averaged Reynolds shear stress, $\overline{vw}^*$, in the *y*-*z* plane at $x^* = 0.23$ ($Re_H = 5.26\times10^4$): (a, c) $g^* = 0.174$, (b, d) $g^* = 0$. The contour interval is 0.0002 and the cutoff level is ± 0.0002.

over the top surface of the model, as is evident from the w^*_{rms} contours in the *x*-*z* plane, to be shown later. The absence of the clearance (Fig 2-10b) increases the w^*_{rms} concentrations about the upper edge of the vertical base, due to the enhanced C-pillar vortices and vortices separated from this edge, internally consistent with the $\overline{\Omega^*_x}$ contours shown in Fig 2-6b.

At $\alpha = 35°$ (Figure 2-10c), the w^*_{rms} concentrations increase significantly right below the upper edge of the slant because of flow separation from this edge. On the other hand, the

concentrations about the two horizontal edges of the vertical base have been impaired, as is expected. It is of interest to note that the strength of the two concentrations corresponding to the lower vortices gains a discernible growth, compared with that at $\alpha = 25°$, which occurs in the context of the greatly weakened C-pillar vortices. Similarly to the case of $\alpha = 25°$, the absence of the clearance (Fig 2-10d) increases the w^*_{rms} concentrations below the upper edge of the slant surface. The v^*_{rms} contours exhibit similar features to those of w^*_{rms} and are therefore not shown.

Figure 2-11 shows the iso-contours of the averaged Reynolds shear stress $\overline{vw}^*$ in the *y*-*z* plane at *x** = 0.23. At $\alpha = 25°$, the relatively high level $\overline{vw}^*$ is mostly concentrated within the C-pillar vortices (c.f. Fig 2-6a), that is, the C-pillar vortices are largely responsible for the production of $\overline{vw}^*$. The clover-leaf pattern about the vortex centre resembles that associated with the spanwise vortex in the near wake of a 2-D bluff body (e.g. Zhou & Yiu 2006). The small magnitude of $\overline{vw}^*$ outside the C-pillar vortices is ascribed to the fact that other longitudinal vortices tend to occur rather randomly in location and hence the associated positive and negative $\overline{vw}^*$ mostly cancel out each other. In the absence of the clearance, the $\overline{vw}^*$ (Fig 2-11b) occurs again mostly within the C-pillar vortices and its maximum magnitude doubles that in Fig 2-11a because of the significantly increased maximum vorticity of the C-pillar vortices (Fig 2-6a & 2-6b). At $\alpha = 35°$, the $\overline{vw}^*$ concentration (Fig 2-11c & 2-11d) diminishes considerably due to the burst of the C-pillar vortices.

Our discussion has so far been focused on the near wake at $x^* = 0.23$; the far wake, i.e., downstream of the recirculation region, should not be ignored. At *x** = 5.80,

the iso-contours of $\overline{\Omega_x^*}$ in the *y*-*z* plane (Figure 2-12) display two counter-rotating

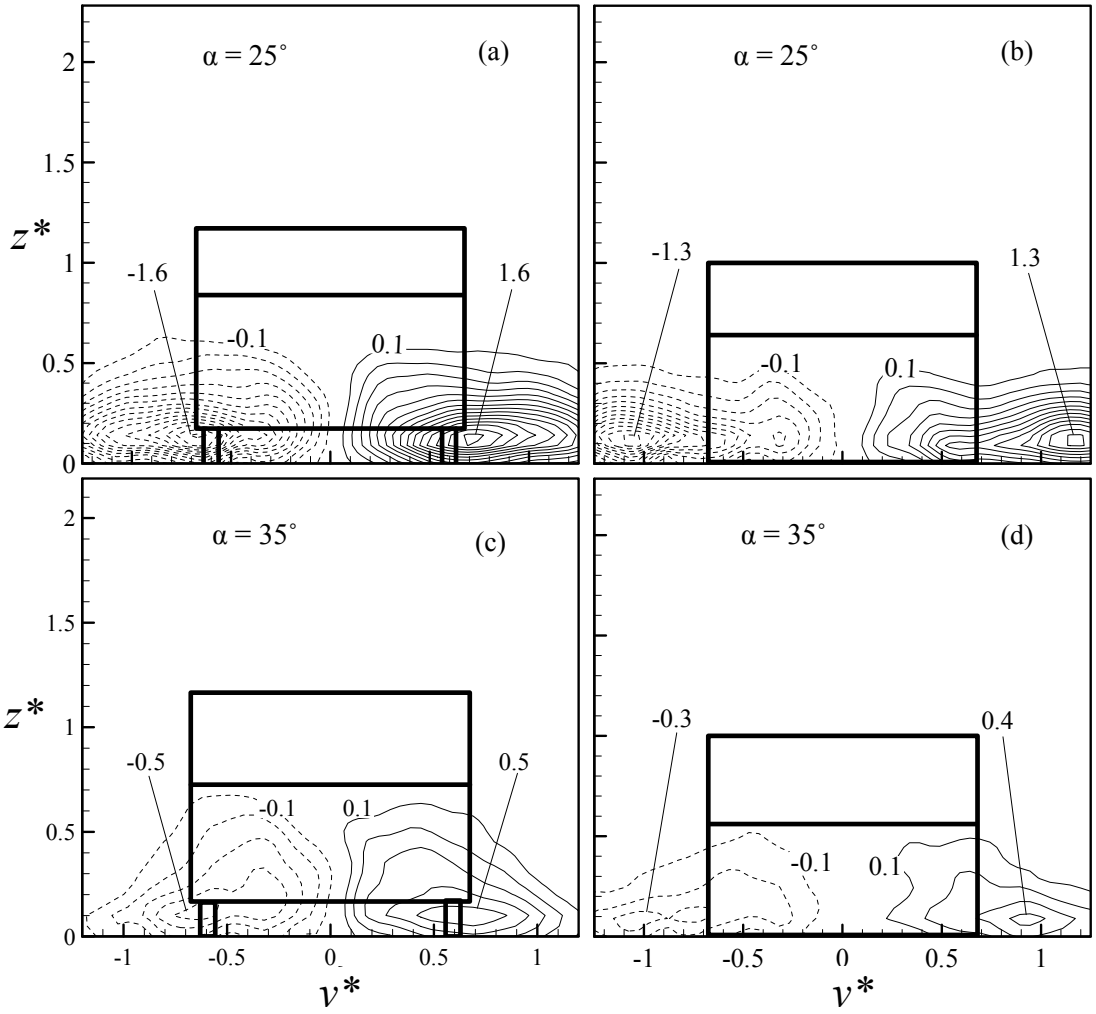

Figure 2-12 Iso-contours of averaged streamwise component, $\overline{\Omega_x^*}$, of vorticity in the *y*-*z* plane at $x^* = 5.8$ ($Re_H = 5.26\times10^4$): (a, c) $g^* = 0.174$, (b, d) $g^* = 0$. The contour interval is 0.1 and the cutoff level is ± 0.1.

vortices, irrespective of the angle of the slant or with and without a clearance. The vortex centres occur much closer to the wall than at $x^* = 0.23$. Note that the maximum vorticity of the vortices with a clearance changes from $\overline{\Omega_x^*} = 6.0$ at $x^* = 0.23$ to 1.6 at $x^* = 5.80$, a drop by 73%, at $\alpha = 25°$ with a clearance but from 9.5 to 1.3, a drop by 84% without a clearance. As such, the strengths of the vortices with a clearance (Fig 2-12a) exceed appreciably their counterparts without a clearance (Fig 2-12b), in distinct contrast to what is shown in Fig 2-6. A similar observation is made at $\alpha = 35°$.

The results suggest that the presence of a clearance enhances the persistence of the vortices. It is noteworthy that, at α = 35° when the C-pillar vortices burst at very beginning, the evolution of the vortices is distinct from that at α = 25°, its maximum vorticity magnitude changing little from x^* = 0.23 to 5.80, irrespective of the presence of the clearance. Furthermore, this magnitude at x^* = 5.80 is substantially lower than its counterpart at α = 25°, implying that the counter-rotating vortices shown in Fig 2-12a & 2-12b must stem from the C-pillar vortices, instead of the recirculatory bubbles behind the vertical base. The results do not support the flow model proposed by Krajnovic & Davidson (2005b) where the downstream vortex was connected to the recirculatory bubble, rather than the C-pillar vortex.

2.4. Spanwise structures

The knowledge of spanwise structures is essential for us to understand thoroughly the highly 3-D flow structure around an Ahmed vehicle model. Figure 2-13 shows the iso-contours of the time-averaged spanwise vorticity, $\overline{\Omega_y^*}$, in the *x*-*z* plane at y^* = 0. At α = 25°, the $\overline{\Omega_y^*}$ -contours (Fig 2-13a and 2-13b) remain attached to the slant surface, be g^* = 0 or not. Two recirculatory bubbles are evident at g^* = 0.174 (Fig 2-13a), which are separated from the upper and lower edges and are referred to in Section 3 as vortices "A" and "B", respectively, though bubble "B" disappears at g* = 0 (Fig 2-13b). At α = 35°, flow separates from the upper edge of the slant, rather than the lower edge (Fig 2-13c and 2-13d). Naturally, the recirculatory bubble "A" is absent. There is a small region of positive $\overline{\Omega_y^*}$ -contours attached to the vertical base at α = 25° or both the slant and vertical base at α = 35°,

induced by the negative circulation. Recirculatory bubble "B" exhibits a considerably

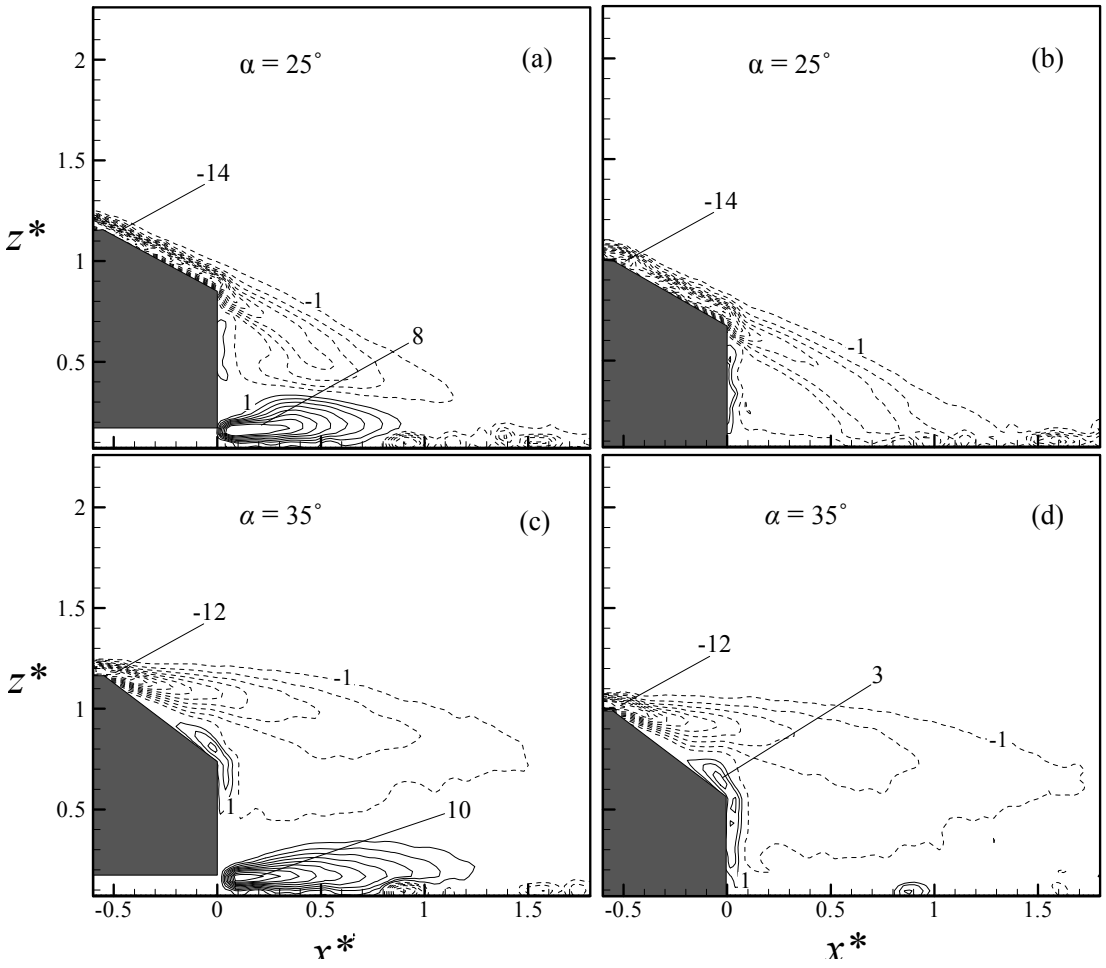

Figure 2-13 Iso-contours of the averaged spanwise component of vorticity, $\overline{\Omega_y^*}$, in the *x*-*z* plane at $y^* = 0$ ($Re_H = 5.26\times10^4$): (a, c) $g^* = 0.174$, (b, d) $g^* = 0$. The contour interval is 1.0 and the cutoff level is ± 1.

larger strength in terms of the maximum vorticity concentration and size at $\alpha = 35°$ than at $\alpha = 25°$. As shown in Fig 2-9, downwash flow is significantly enhanced at $\alpha = 25°$, compared with the case of $\alpha = 35°$, acting to repress the development of bubble "B". It is worth noting that vortex "A" or "B" produces a much higher vorticity concentration in the *x*-*z* plane than in the *y*-*z* plane (Fig 2-6), suggesting its overwhelmingly spanwise orientation.

Typical instantaneous iso-contours of Ω_y^* are illustrated in Fig 2-14, with the

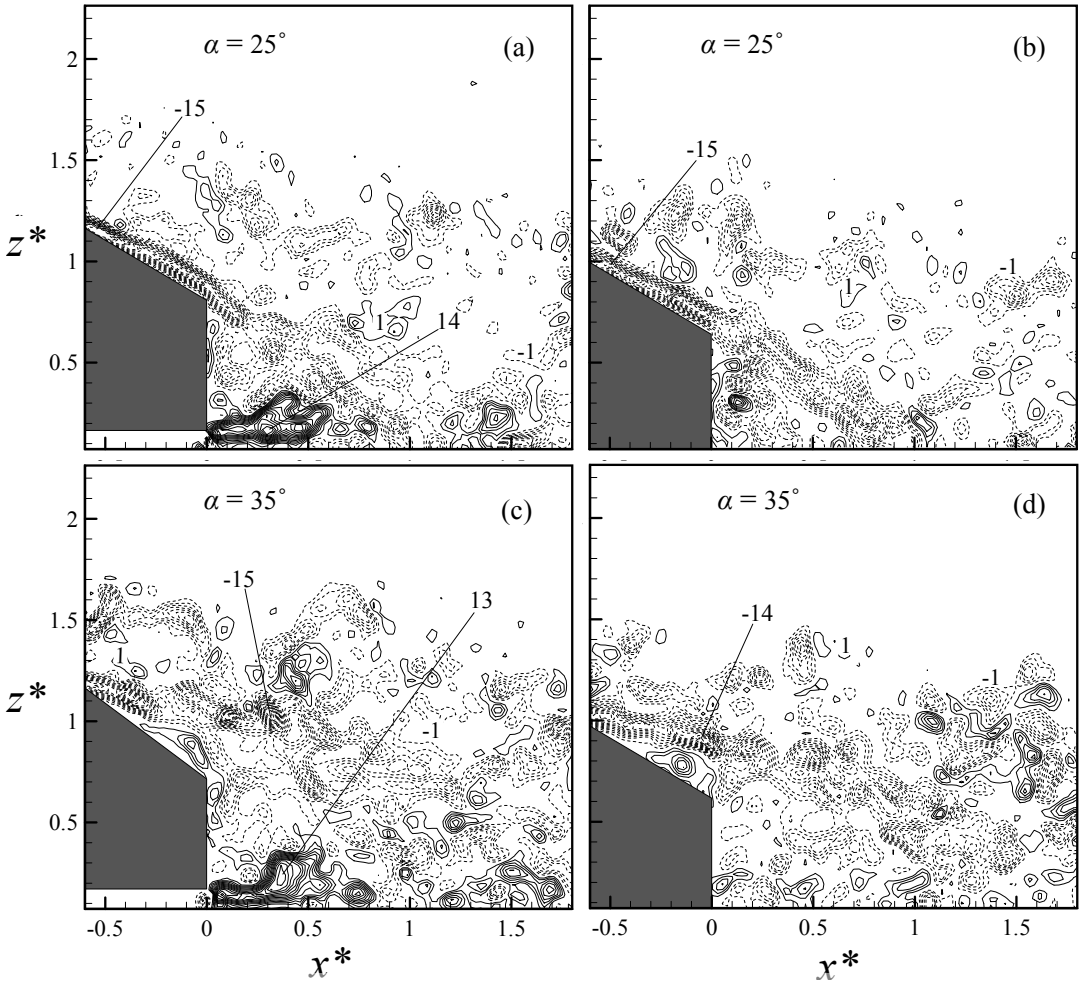

Figure 2-14 Iso-contours of the instantaneous spanwise component of vorticity, Ω_y^*, in the *x*-*z* plane at $y^* = 0$ ($Re_H = 5.26\times10^4$): (a, c) $g^* = 0.174$, (b, d) $g^* = 0$. The contour interval is 1.0 and the cutoff level is ± 1.0.

major features consistent with the time-averaged picture (Fig 2-13). For example, at α = 25°, there is one highly concentrated negative vorticity layer attached to the slant surface. After separating from the upper edge of the base, part of it rolls up, forming a recirculation behind the base, and the rest appears shooting towards the wall and then rebouncing. There are some vorticity concentrations downstraem of the base and above the body. These structures correspond to the concentrations above the top of the model observed in Fig 2-6a and 6b. The upper recirculatory bubble "A" and lower "B" are evident with $g^* = 0.174$; "B" is absent with $g^* = 0$. Flow separation occurs at

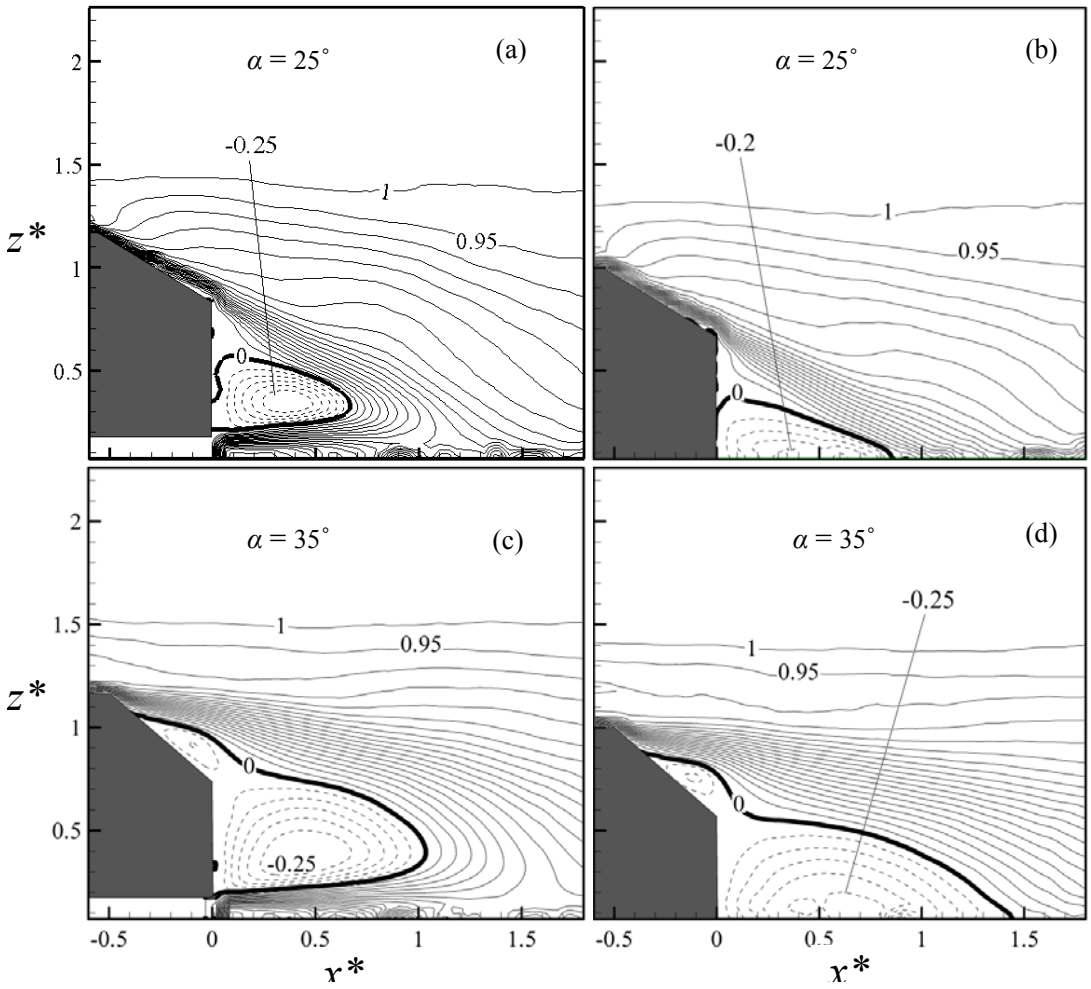

Figure 2-15 Iso-contours of averaged streamwise velocity, $\overline{U}^*$, in the *x*-*z* plane at *y** = 0 (Re_H = 5.26×10^4): (a, c) *g** = 0.174, (b, d) *g** = 0. The contour interval is 0.05.

the upper edge of the slant at α = 35° and bubble "A" is not seen.

The distribution of the mean streamwise velocity, $\overline{U}^*$, in the *x*-*z* plane may allow us to determine the reversed flow region or wake bubble, which may provide us with the information on aerodynamic drag. The reversed flow region is identified with negative $\overline{U}^*$, and is enclosed by $\overline{U}^*$ = 0, which is highlighted by a thick contour in Fig 2-15. Its maximum longitudinal length is defined as the bubble or recirculation length. This length is 0.67H at α = 25° and grows to 1.03H at α = 35° for g* = 0.174. At α = 35°, the recirculation region grows significantly, including a small region

attached to the slant surface and a region behind the vertical base, as observed by

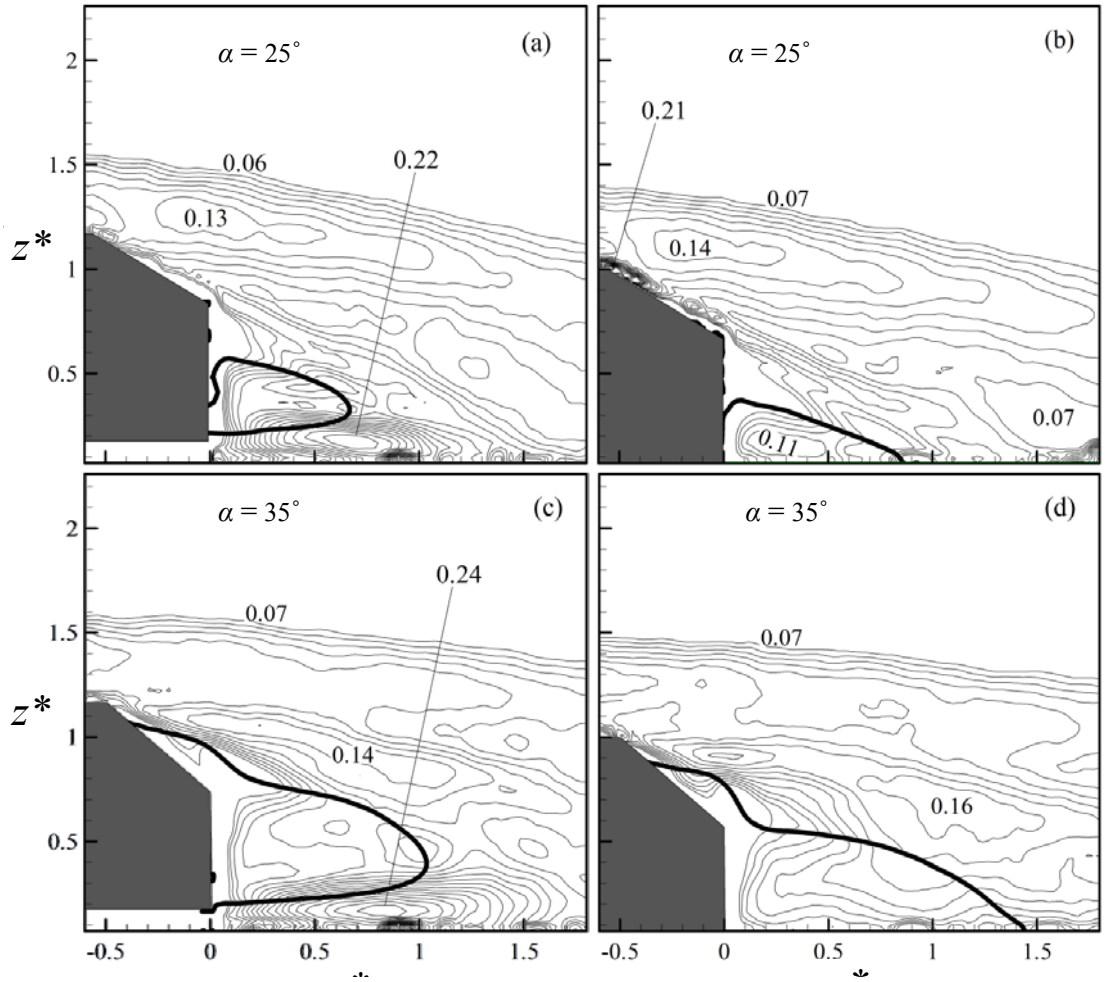

Figure 2-16 Iso-contours of the rms streamwise velocity, u^*_{rms}, in the *x*-*z* plane at *y** = 0 (Re_H = 5.26×10^4): (a, c) *g** = 0.174, (b, d) *g** = 0. The contour interval = 0.01. The bold-line denotes $\overline{U}^* = 0$.

Lienhart & Becker (2003) at the same α and also Vino *et al*. (2005) at α = 30°. The variation of the recirculation length with α is consistent with the difference in the pressure drag coefficient due to the vertical base, which is 0.08 at α = 25° and 0.095 at α = 35° (Ahmed *et al*. 1984). In the absence of the clearance (g^* = 0), the recirculation region is enclosed by $\overline{U}^*$ = 0, the slant and base surfaces, and wall. The recirculation length is prolonged to 0.86H at α = 25° and 1.43H at α = 35°.

The iso-contours of the rms streamwise velocity, u^*_{rms}, in the *x*-*z* plane (Figure

2-16a) at $y^* = 0$ show three major concentration regions at $\alpha = 25°$ and $g^* = 0.174$.

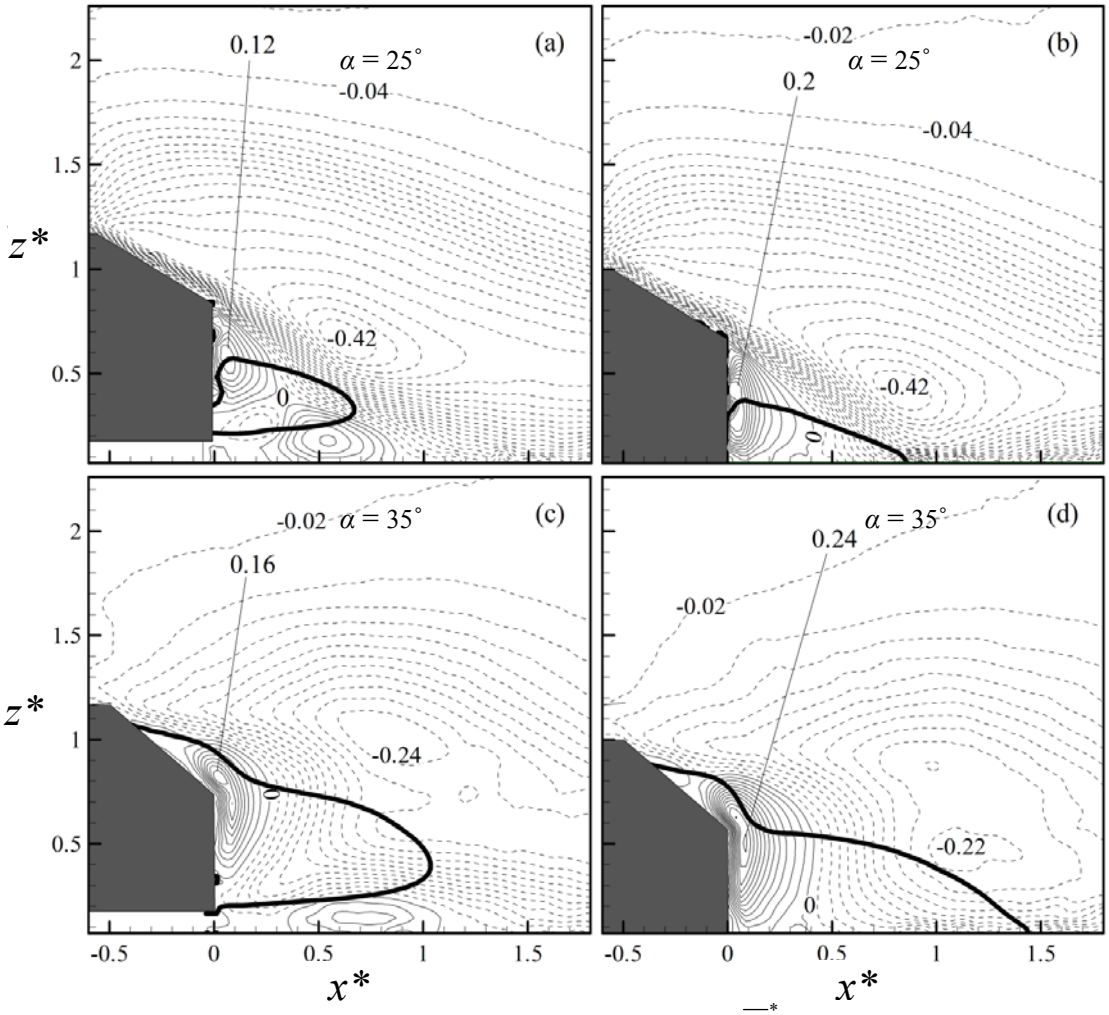

Figure 2-17 Iso-contours of the averaged vertical velocity, $\overline{W}^*$, in the x-z plane at $y^* = 0$ ($Re_H = 5.26\times10^4$): (a, c) $g^* = 0.174$, (b, d) $g^* = 0$. The contour interval is 0.02. The bold-line denotes $\overline{U}^* = 0$.

The maximum concentration occurs at $x^* \approx 0.7$ and $z^* \approx 0.2$, apparently associated with bubble "B". The concentration above "B" is attributed to bubble "A" and has markedly less intensity. The third one is located at $x^* \approx 0.0$ and $z^* \approx 1.25$ and is evidently connected to the shear layer separated from the upper edge of the slant. The observation points to that, while part of the shear layer developed over the top of the model remains attached to the slant (Figs 2-14a and 2-15a), the other part is detached from the body, responsible for the concentrations above the upper edge of the slant,

albeit weak, in the $\overline{\Omega_x^*}$- and w_{rms}^*-contours (Figs 2-6a and 2-10a). At α = 35° (Fig 2-16c), the three concentrations are still discernible. The concentration from shear layer separation from the upper edge of the slant appears now downward dislocated. The concentration due to bubble "B" grows appreciably probably because of the greatly weakened concentration related to bubble "A". At g^* = 0 (Fig 2-16b), there is one weak concentration behind the vertical base and near the wall, probably induced by the shear layer shooting towards the wall. Note that in each case there is one blank area near the upper edge of the base, where the u_{rms}^*-contour level is very low. This area corresponds to the stagnant fluid region where $\overline{U}^* \approx 0$ (c.f. Fig 2-15).

The iso-contours of the time-averaged velocity, $\overline{W}^*$, in the x-z plane at y^* = 0 (Figure 2-17) essentially conform to the flow structure models proposed by Ahmed *et al*. (1984). At α = 25° and g^* = 0.174 (Fig 2-17a), four concentrations are seen. The upper two are connected to the motion of bubble "A" and the lower two are linked to bubble "B", which could not be seen naturally at g^* = 0 (Fig 2-17b and 17d). At α = 35°, the positive concentration of $\overline{W}^*$ attached to the vertical base is extended to the area over the slant due to flow separation from the upper edge of the slant; the two negative concentrations are merged.

The iso-contours of the rms vertical velocity, w_{rms}^*, in the x-z plane at y^* = 0 display two concentrations at α = 25° and g^* = 0.174 (Figure 2-18a). The upper one is apparently associated with the shear layer detached from the upper edge of the slant. The maximum of the lower one occurs right between bubbles "A" and "B" (c.f. Fig 2-13a), suggesting that this concentration results from both "A" and "B". Naturally,

the absence of bubble "B" at $g^* = 0$ (Fig 2-18b) leads to a great reduction in the strength of this concentration. At $\alpha = 35°$ and $g^* = 0.174$ (Figure 2-18c), the upper concentration is downward shifted, with an increased maximum magnitude, due to a

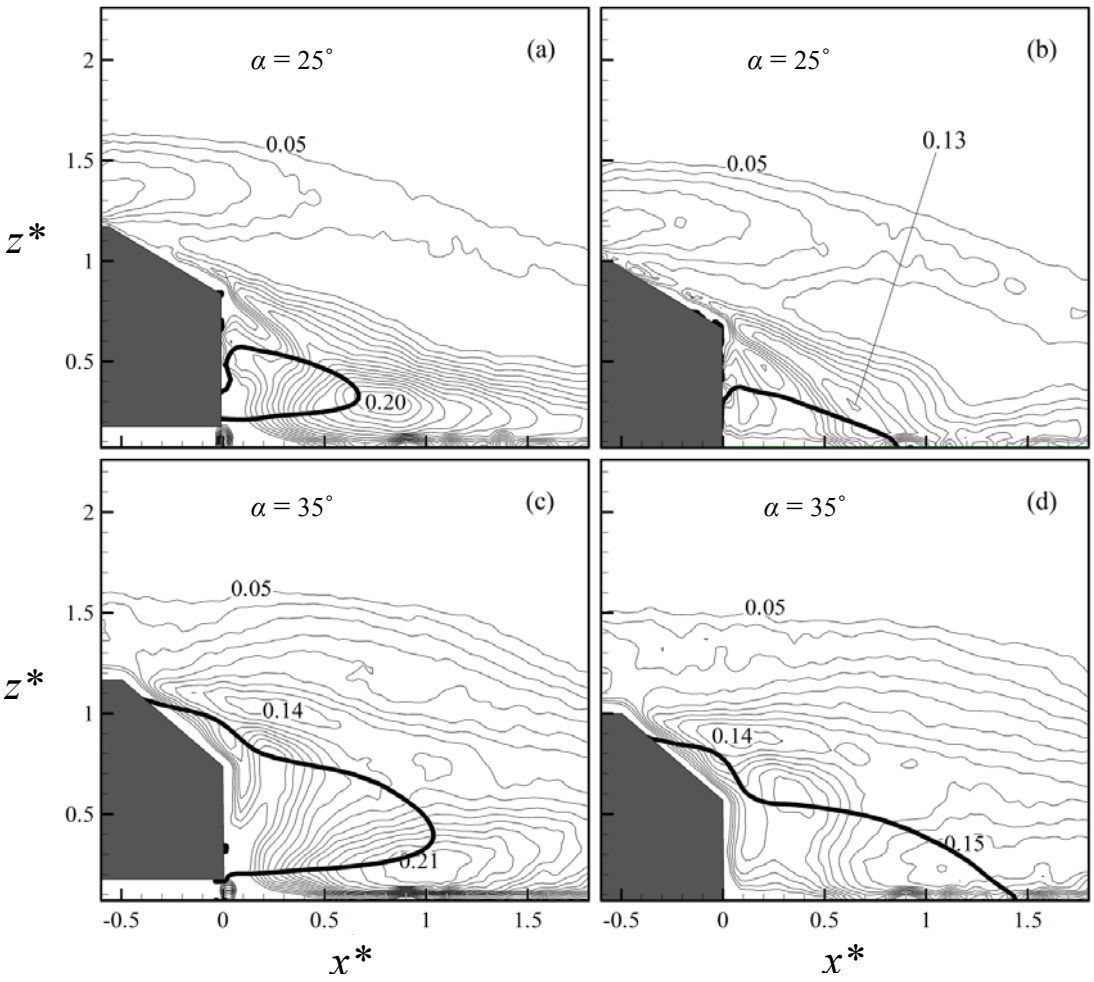

Figure 2-18 Iso-contours of the rms vertical velocity, w^*_{rms}, in the x-z plane at $y^* = 0$ ($Re_H = 5.26\times10^4$): (a, c) $g^* = 0.174$, (b, d) $g^* = 0$. The contour interval = 0.01. The bold-line denotes $\overline{U}^* = 0$.

change in the flow separation location. At $g^* = 0$, the lower concentration is again greatly reduced without bubble "B".

The Reynolds shear stress, $\overline{uw}^*$, in the x-z plane ($y^* = 0$) show three concentrations at $\alpha = 25°$ and $g^* = 0.174$ (Figure 2-19a). The upper and lower concentrations behind the base are generated by bubbles "A" and "B", respectively.

The lower is positive and the upper is negative, with the former exceeding considerably the latter in the magnitude of $\overline{uw}^*$. This is expected since bubble "B" is largely associated with positive *u* and positive *w* (upwash), and "A" associated with

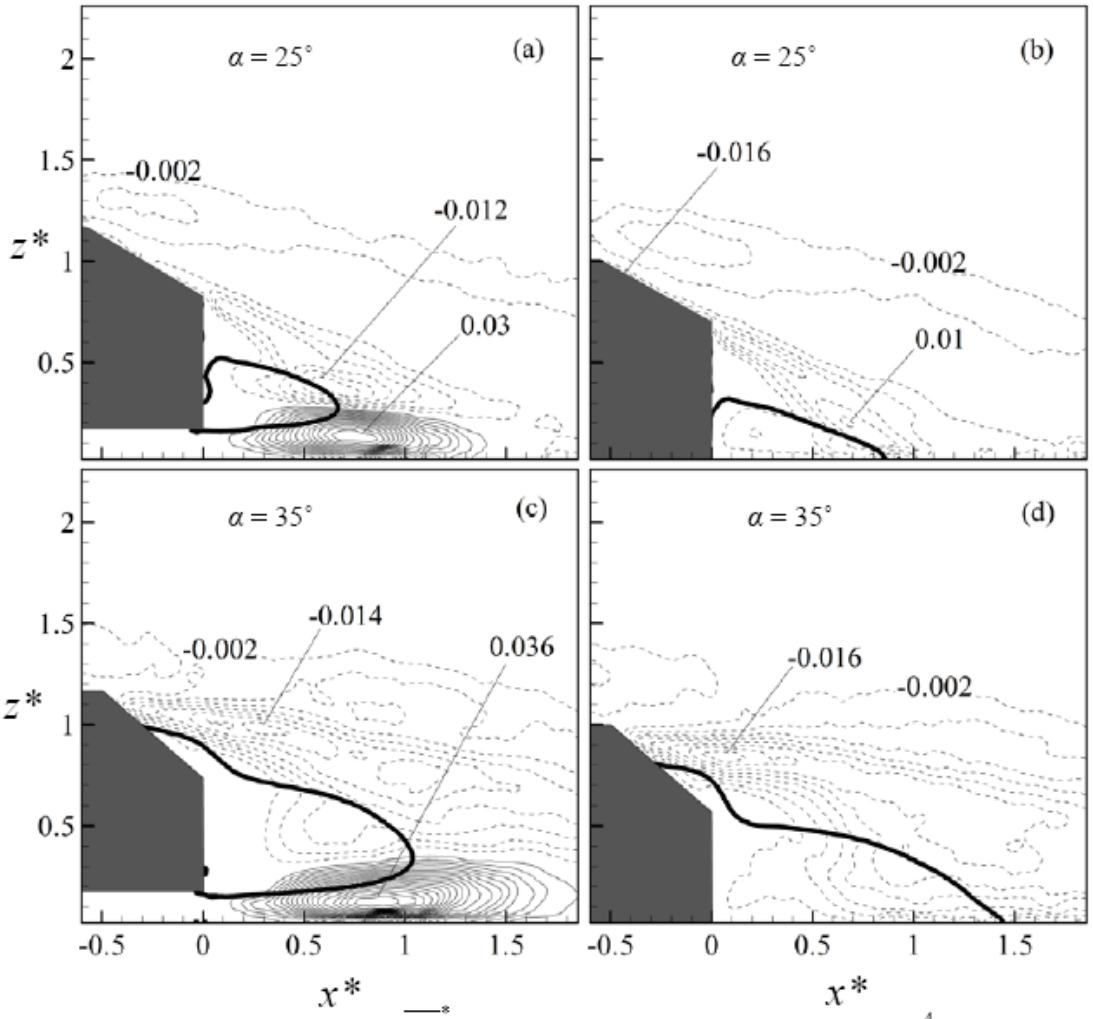

Figure 2-19 Iso-contours of the $\overline{uw}^*$, in the *x*-*z* plane at $y^* = 0$ ($Re_H = 5.26\times10^4$): (a, c) $g^* = 0.174$, (b, d) $g^* = 0$. The contour interval is 0.002 and the cutoff level is ±0.002. The bold-line denotes $\overline{U}^* = 0$.

positive *u* and negative *w* (downwash). The concentration above the slant is due to the detached shear layer from the upper edge of the slant and is negative because positive *u* is mostly associated with negative *w*. Its magnitude is markedly weaker than the other two concentrations. At $\alpha = 35°$, the two negative concentrations merge into one because the recirculation over the slant is connected to that behind the base (Fig

2-19c). At $g^* = 0$, there is no positive concentration behind the base because of the absence of bubble "B" (Fig 2-19b and 19d). The negative concentration is weakened at $\alpha = 25°$ due to an impaired bubble "A" (Fig 2-13b).

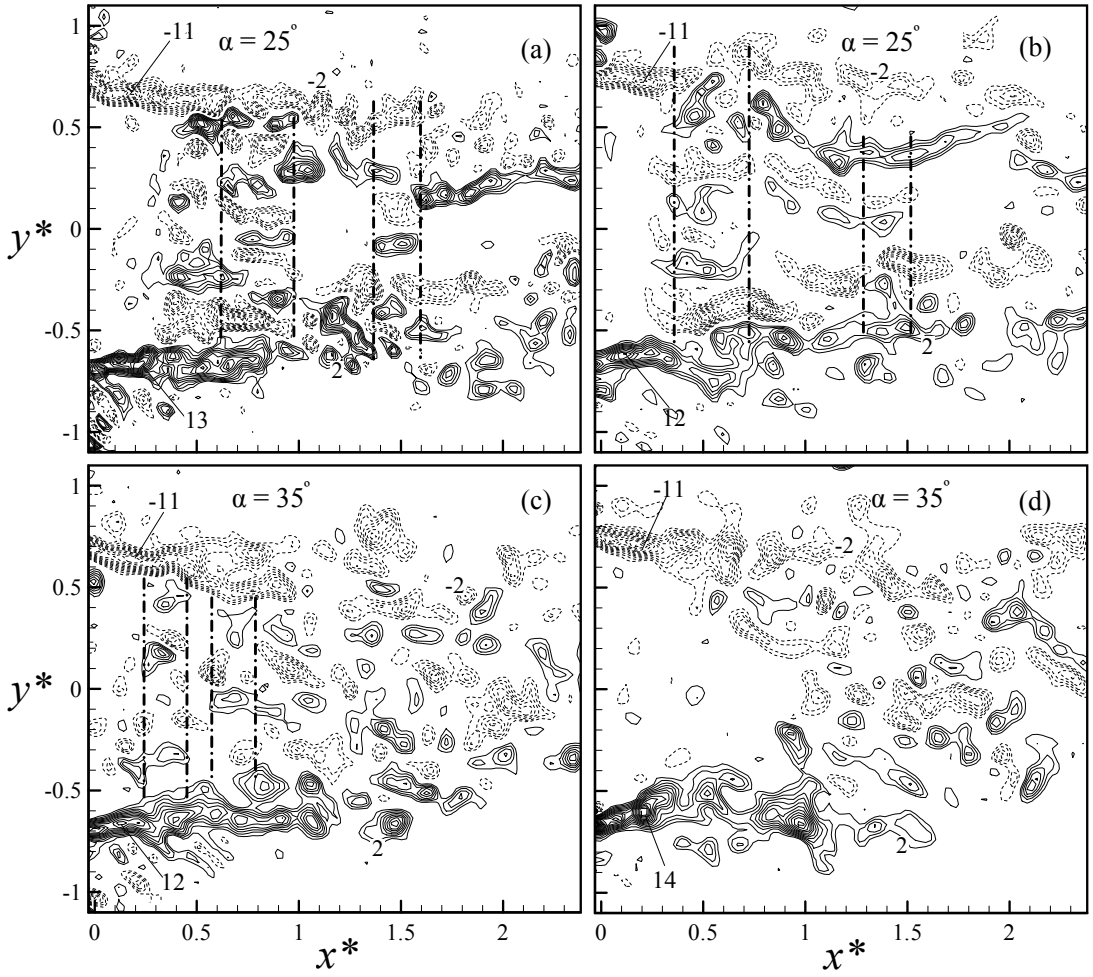

Figure 2-20 Iso-contours of instantaneous transverse vorticity, Ω_z^*, in the *x*-*y* plane at (Re_H ($Re_H = 5.26\times10^4$): (a, c) $z^* = 0.67$, $g^* = 0.174$, (b, d) $z^* = 0.5$, $g^* = 0$. The contour interval is 1 and the cutoff level is ± 2.

2.5. Transverse structures

The behaviours of the 3-D flow structure in the *x*-*y* plane are investigated by examining the transverse structures of vorticity. Figure 2-20 presents the typical iso-contours of the instantaneous vertical component of vorticity, Ω_z^*, in the *x*-*y* plane

at $z^* = 0.67$ for $g^* = 0.174$ and $z^* = 0.50$ for $g^* = 0$. As in the *y*-*z* and *x*-*z* planes, the instantaneous flow structure appears complicated. Consider first the case of $\alpha = 25°$. Two highly concentrated vorticity strips, emanating from the two side surfaces of the model, are located symmetrically about $y^* = 0$， viz. at $y^* \approx -0.7$ and 0.7, respectively, apparently corresponding to vortex "D" (Fig 2-6a). Their maximum magnitudes of Ω_z^* reaches 13 and 11, respectively, by far greater than their counterpart in the *y*-*z* plane (Figs 2-6 and 2-7). This is expected since the vorticity vector produced by the shear layer or the gradient of *U* in the *y* direction is predominantly along the *z*-direction. The strip structures appear breaking down into patches at $x^* \approx 1.0$, probably as a result of interaction and merger with the C-pillar vortices. The patches are characterized by markedly lower maximum vorticity. It is noteworthy that the C-pillar vortex is downward inclined in the near wake and hence its induced vorticity concentrations in the *x*-*y* plane are of the same sign as those of vortex "D" on the same side. On another note, the oppositely signed structures tend to occur over $x^* = 0.35 \sim 1.0$ on the inner side ($y^* \approx \pm 0.5$) of the two strip structures, possibly resulting from interactions between the strip structures and recirculatory bubbles "A" and "B". Furthermore, as observed in the *y*-*z* plane, a number of alternately signed structures are arranged in a row along the y-direction. Two such rows are discernible in Fig 2-20a, as highlighted by thick broken lines. A quasi-longitudinal vortex, which is not oriented exactly longitudinally but inclined with respect to the x-axis, may show up in the *x*-*y* plane. Therefore, these structures are ascribed to the signatures of the alternately signed longitudinal structures associated with bubbles "A" and "B"

observed in Figs 2-6a and 2-7a. The association with "A" is more likely since the structures associated with "B" should be smaller, as will be discussed later in this section. The above flow features are also seen in the absence of clearance, i.e., $g^* = 0$ (Fig 2-20b).

At α = 35°, the flow structure exhibits differences. Firstly, vorticity concentrations are more randomly distributed, all over the place at $g^* = 0.174$ (Fig 2-20c), but depleted in the recirculation region at $g^* = 0$ (Fig 20d). At this configuration, flow separates from the upper edge of the slant, not the lower, and the absence of bubble "A" accounts for the more randomly distributed vorticity concentrations. At $g^* = 0$, bubble "B" does not exist either and the vorticity concentrations separated from the upper edge of the slant can hardly reach the recirculation region at $z^* = 0.5$. As such, there are few vorticity concentrations in this region. Secondly, the alternately signed concentrations, highlighted by thick broken lines, are still discernible at $g^* = 0.174$ but appear smaller-scaled, albeit slightly, than those at $\alpha = 25°$. The structures are connected to bubble "B", which is associated with smaller scaled vorticity concentrations than "A". This point is illustrated in Fig 7a. Since bubble "A" is larger than "B", as is evident in the models (Fig 2-1) proposed by Ahmed *et al*. (1984), we may also infer that the longitudinal structures associated with "A" should be larger in scale. Such structures could not be identified at $g^* = 0$ because of the absence of bubble "B".

With the instantaneous transverse structures in mind, the corresponding mean vorticity field may be interpreted. In all cases, the iso-contours of $\overline{\Omega_z^*}$ in the *x*-*y*

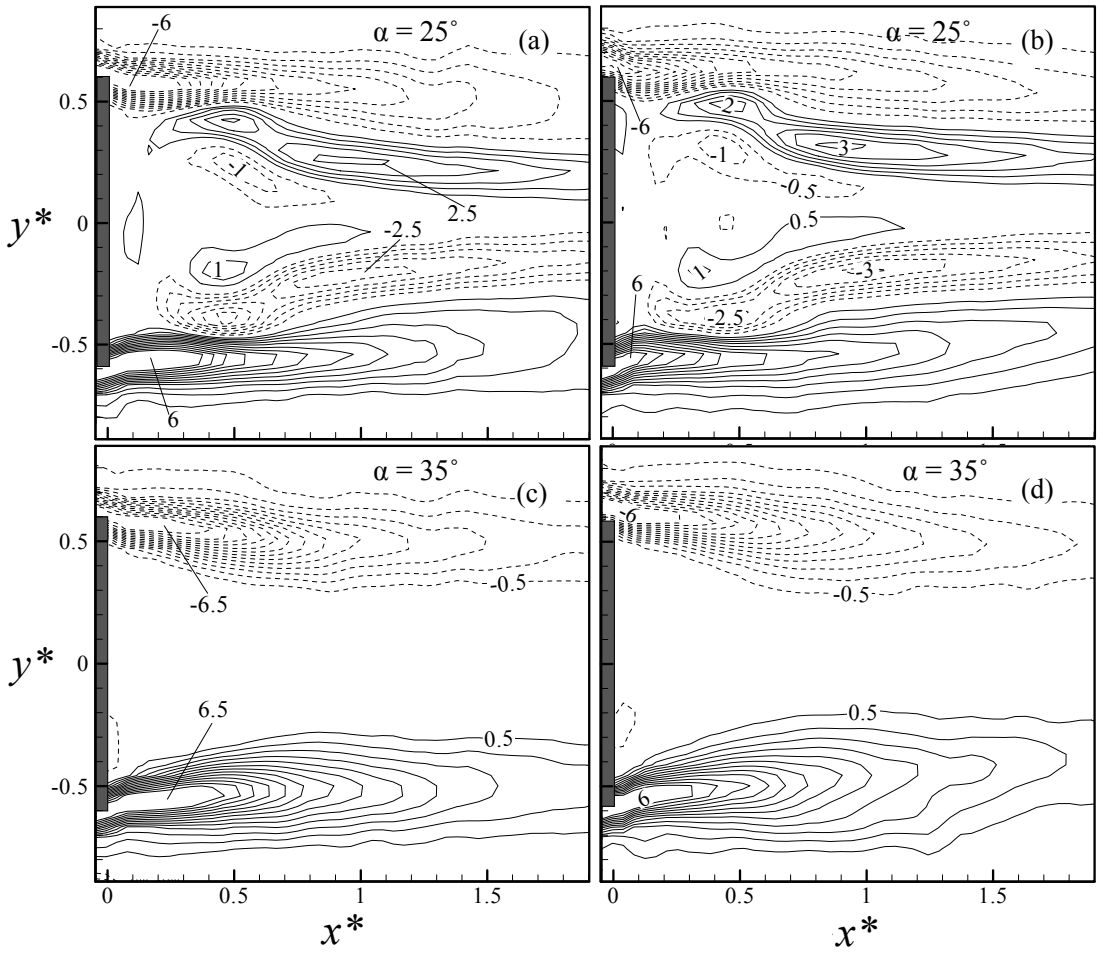

Figure 2-21 Iso-contours of the averaged vertical component of vorticity, $\overline{\Omega_z}^*$, in the *x*-*y* plane at ($Re_H = 5.26\times10^4$): (a, c) $z^* = 0.67$, $g^* = 0.174$, (b, d) $z^* = 0.5$, $g^* = 0$. The contour interval is 0.5 and the cutoff level is ± 0.5.

plane (Figure 2-21) are approximately symmetrical about $y^* = 0$. At $\alpha = 25°$ and $g^* = 0.174$, three strips are shown on each side of $y^* = 0$ (Fig 2-21a). The outer strip results largely from vortex "D" and its merging, starting from $x^* \approx 1.0$, with the C-pillar vortex. The middle oppositely signed strip may result from the interaction between "D" and bubble "A". The contribution from "B" could not be excluded. The sign of the inner strip is different from that of the middle strip, corroborating our proposition of bubble "A" in Fig 2-8. There is a blank area between the two inner strips, which meet at about $x^* \approx 0.7$. Further away from the C-pillar vortex which induces an oppositely signed vorticity concentration (e.g. Fig 2-7a), those vorticity

concentrations in the row of alternately signed structures associated with "A" tend to occur more randomly along the spanwise direction, enhancing the cancelation of each other. At $g^* = 0$ (Fig 2-21b), a similar flow structure is observed, supporting the assertion that the middle and inner strips are linked with the occurrence of the bubble "A".

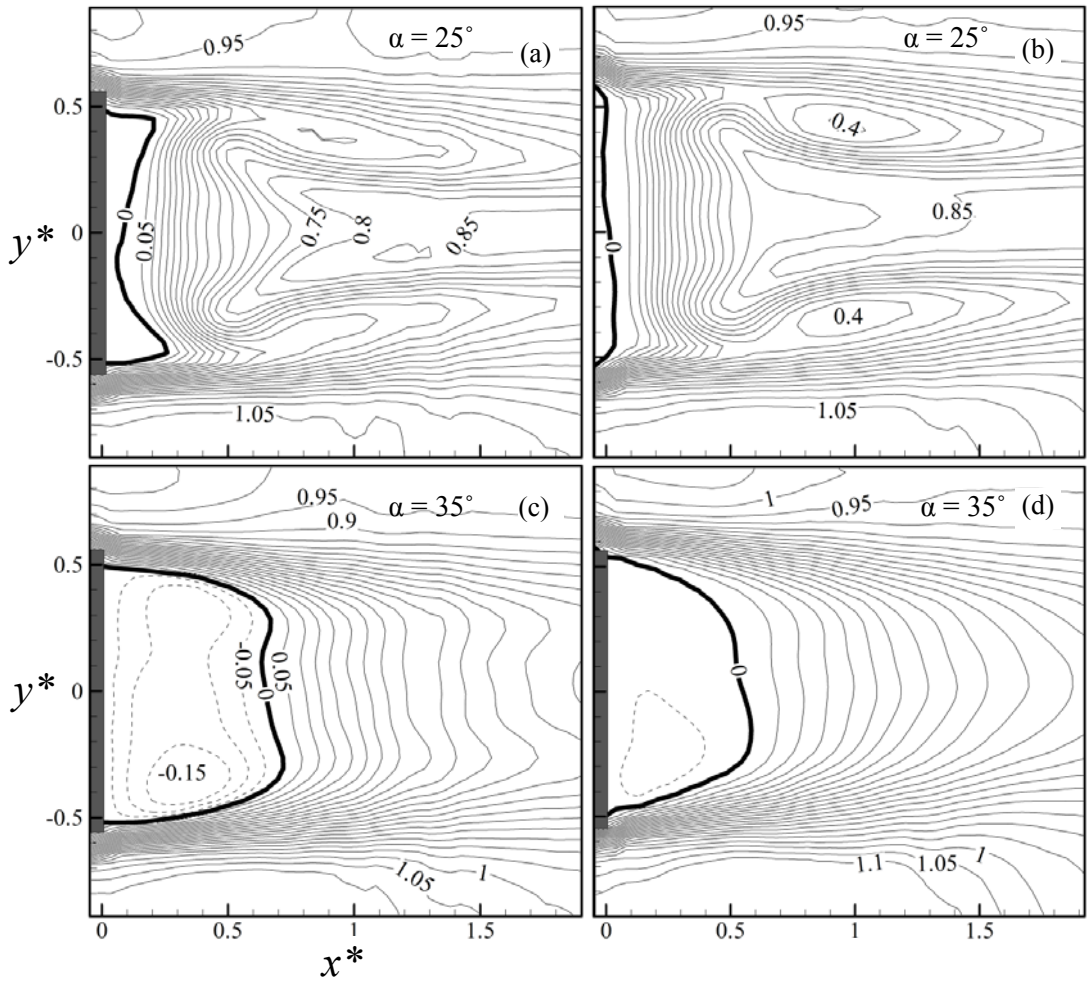

Figure 2-22 Iso-contours of the averaged streamwise velocity, $\overline{U}^*$, in the *x*-*y* plane at ($Re_H = 5.26\times10^4$): (a, c) $z^* = 0.67$, $g^* = 0.174$, (b, d) $z^* = 0.5$, $g^* = 0$. The contour interval is 0.1.

At $\alpha = 35°$, the outer strip only is observed in Fig 2-21c and 21d. This is not unexpected since bubble "A" does not exist; furthermore, at $g^* = 0.174$, the alternately signed structures associated with "B", as seen in Fig 2-20c, are located more randomly along the spanwise direction, promoting the cancelation of each other.

The $\overline{U}^*$-contours in the *x*-*y* plane (Fig 2-22) are approximately symmetric about *y** = 0; the contour of $\overline{U}^*$ = 0 encloses the recirculation region in the *x*-*y* plane. This region increases greatly at α = 35° than 25°, be *g** = 0 or not.

2.6. Summary and conclusions

The 3-D near wake of the Ahmed model, with and without a clearance (g* =

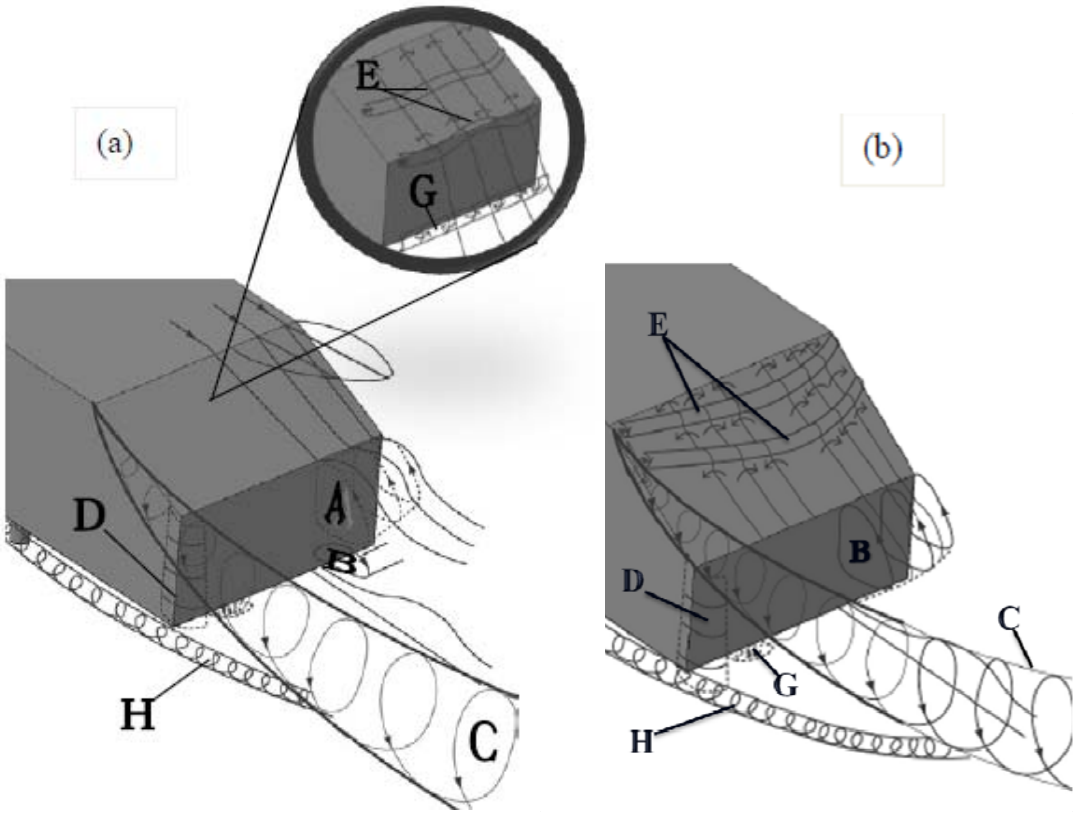

Figure 2-23 the schematic of the flow structure behind an Ahmed vehicle model:
(a) α = 25º, (b) α = 35º

0.174) from wall, has been investigated at $Re_H = 5.26\times10^4$ in detail based on the PIV measurements in three orthogonal planes. Two distinct flow regimes are examined, as represented by the configurations of α = 25° and 35°, respectively. The investigation leads to a number of findings, as summarized and incorporated in the schematic of the flow structure in Figure 2-23.

In the regime of α < 30°, following modifications are made, compared with the

classical model shown in Fig 2-1a:

1 Shear layer developed over the top of the vehicle model flows partially along the slant under the effect of the C-pillar vortex and detaches partially from the body, as suggested by the distributions of the Reynolds stresses (Figs 2-16a, 2-18a and 2-19a).

2 While part of the shear layer separated from the slant is drawn into recirculation bubble "A", the other part forms a quasi-periodical wavy spanwise roll flowing over "A", as is suggested by instantaneous Ω_y-contours (Fig 2-14a). The spectra of both fluctuating pressure and velocity signals measured near the upper edge of the vertical base by Vino *et al.*'s (2005) displayed a pronounced peak at a dimensionless frequency of 0.11, providing experimental evidence for quasi-periodical flow separation from the upper edge of the base. This spanwise roll produces alternately signed vorticity concentrations in the *y*-*z* plane (Figs 2-6a and 2-7a) and in the *x*-*y* plane (Figs 2-20a and 2-21a).

3 Separated from the lower edge of the base, the gap flow between the model underside and wall is partially drawn into recirculatory bubble "B" and partially rolls up, forming a spanwise roll that is separated quasi-periodically, again based on Vino *et al.*'s (2005) data. This roll is wrapped by longitudinal structures, as is supported by instantaneous longitudinal vorticity contours (Fig 2-7a). Its signature in the *x*-*y* plane is also discernible by the alternately signed transverse vorticity concentrations in Fig 2-20a.

4 Side vortex “D” is added, which is generated by the shear layer developed over the side surface. This vortex starts breaking down at $x^* \approx 1.0$ as a result of interaction and merger with the C-pillar vortex.

5 The previously observed lower vortex (Krajnovic *et al.* 2005; Strachan *et al*. 2007) is added, which is generated by the pressure difference between flow inside the gap and that outside, in a manner similar to how the C-pillar vortices are generated.

6 One pair of gap vortices are included, which are generated by struts between the model underside and wall.

In the regime of $\alpha \geq 30°$, the modifications 3 through 6 at $\alpha < 30°$ apply. Following changes are noted, as per the case of $\alpha < 30°$:

1 The shear layer developed over the top of the vehicle now separates near the upper edge of the slant (Figs 2-13c, 2-14c, 2-15c, 2-17c and 2-19c) and is imbedded with alternately signed longitudinal vortices, as evidenced in Figs 2-6c and 2-7c.

2 The C-pillar vortex is greatly weakened, as shown in Figs 2-6c and 2-7c.

3 Recirculation bubbles “E” over the slant and “A” behind the base merge into one (Figs 2-13c, 2-14c, 2-15c, 2-17c and 2-19c).

In addition, the effect of the clearance between the model underside and wall has been investigated. It has been found that this clearance has a pronounced effect on the near wake of the vehicle model. Firstly, both bubbles “A” and “B” are altered at $g^* = 0$ (Figs 2-13b, 2-13d, 2-14b, 2-14d and 2-19), including the disappearance of bubble

"B". But this does not necessarily mean the total recirculation bubble may shrink in size. As a matter of fact, the bubble size grows at $\alpha = 35°$, as shown in Fig 2-15c-d. Secondly, the absence of the clearance changes the strengths of the C-pillar vortex "C" and side vortex "D" (Fig 2-6).

Finally, the mean velocity and the second moments of fluctuating velocities have been obtained in three orthogonal planes for different configurations, i.e., $g^* = 0.174$ and 0 and $\alpha = 25°$ and 35°, which may be used for the validation of numerical models in the future.

CHAPTER 3

TURBULENT FLOW STRUCTURE IN A CYLINDER-ON-CONE CYCLONE

3.1. Introduction

Cyclone separators have been used in various industries for about 100 years, and are still one of the most widely used industrial gas-cleaning devices, e.g., vehicle exhaust-gas cleaning devices, vacuum cleaners, incinerators and boilers. In spite of a long history, the basic design of cyclones has evolved little from its first application, perhaps mainly due to the complexity and inadequate knowledge of the turbulent swirling flow, including the precessing vortex core inside the cyclone. Early experimental investigations of cyclones were conducted using pitot tubes (Linden 1949) and hot-wire anemometry (Ustimenko & Bukhman 1968), aiming primarily at understanding the turbulent flow structure and determining the most efficient shape of a cyclone. The two techniques suffer from a few drawbacks, for example, being intrusive to flows and point measurement, giving insufficient information on the overall flow structure. With the advent of non-intrusive laser Doppler velocimetry (LDA), there have been increasing experimental investigations of the gas flow in a cyclone in the last one or two decades. Using LDA, O'Doherty *et al.* (1991) unveiled a very complex flow structure associated with the strongly swirl flow in a cyclone. It is well known that flow with a high swirl number (>0.6) and a high Reynolds number ($Re = U_{in}\ 2R/\nu$, where R is the radius of the cyclone chamber, U_{in} the inlet velocity, and ν the kinematic viscosity of fluid) of more than 10^4 in a confined flow produces

the onset of vortex breakdown and a low frequency instability phenomenon due to the precessing motion of the vortex core (Chanaud 1965, Cassidy & Falvey 1970, Gouldin *et al.* 1984, Harvey 1962, Sarpkaya 1971). Alekseenko *et al.* (1999) reported the results of theoretical and experimental investigation of steady helical vortex structures in a swirl flow. They observed a linear relationship between the Strouhal number, St ($\equiv f_{prec}\ 2R/U_{in}$, where f_{prec} is the precessing frequency of the vortex in the cyclone), and Re (= 14000 ~ 45000) at a swirl number, S ($\equiv \pi\ d_e\ R\ /\ 2A$, where d_e is the diameter of the cyclone outlet, and A is the inlet area), of 1 ~ 3.8. Fluid dynamics in a cylinder-on-cone cyclone is different from the helical flow model. The former is in general characterized by the presence of a reverse flow, while the latter is not. Derksen & Akker (2000) noted numerically that the main vortex core moved about the geometrical axis of the reverse flow cyclone in a quasi-periodic manner, and St was found to be 0.53 at Re = 14000 and S = 2.1. Hoekstra *et al.* (1999) experimentally observed St = 0.6 in a cyclone of similar geometry at a comparable Re and S =3.1. However, Alekseenko *et al.* (1999) measured St = 0.85 at S = 1.9 and Re = 14000 ~ 45000. Peng *et al*. (2005) also observed experimentally a similar St value at S = 2.0 and Re = 57300 ~ 260000, and predicted a slightly lower St near the wall just under the vortex finder using a theoretical model of the tangential velocity of the flow at the wall.

In spite of previous investigations, many aspects of fluid dynamics including the flow instabilities such as the vortex breakdown and precessing vortex core (PVC) within a cyclone have yet to be better understood. These instabilities will generate

extra losses and produce a higher pressure drop in the cyclone. In term of particle separation, the PVC will cause a pressure fluctuation and associated high levels of turbulence and mixing in the cyclone (Biffin *et al.* 1984). As a result, there are problems with cyclones in engineering such as the incorrect prediction of the separation efficiency of submicron particles in common industrial cyclone separator (Yazdabadi *et al.* 1994). Previous investigations on PVC and associated instabilities are mostly related to swirl burners (Schildmacher & Koch 2005) and generators (Czarny *et al.* 2002); there have been very limited reports on the PVC, which occurs in a cyclone, with a reverse flow. This work aims to improve our understanding of the turbulent flow structure in a cylinder-on-cone cyclone that is characterized by a reverse flow in the core region. Measurements were conducted in an industrial cyclone model using particle imaging velocimetry (PIV) and laser Doppler velocimetry (LDA). Experimental details are given in Section 3.2. Experimental results are presented and discussed in Section 3.3. The work is concluded in Section 3.4.

3.2. Experimental details

Experimental investigation was conducted based on a laboratory scale model of cyclones as illustrated in Figure 3-1. The cyclone radius R is 47 mm, the outlet diameter d_e is 44 mm, the cyclone cylinder length L is 132 mm, and cross-sectional area of the cylindrical body A is 1100 mm^2. The coordinate system, (r, θ, z), is defined in Fig. 1a, with its origin at the center of the bottom plane of the cylindrical section of the cyclone body. The velocity components in the r, θ and z directions are

designated by V_r, V_θ, and V_z, respectively. The cylinder-on-cone cyclone was made of transparent acrylic. The inlet flow velocity of the cyclone, measured by a pitot tube, was 8 m/sec. Experiments were firstly conducted at $S = 3.0$ $Re = 47000$.

A two-component LDA system (Dantec Model 58N40) with an enhanced FVA signal processor was used to measure and V_θ and V_z along the axis X-X of the measurement plane at $z = R$ (Figure 3-1a and 3-1c). This section at $z/R = 1$ should be quite representative of others, except near the top and bottom of the cyclone, as indicated in PIV data in the (r, z) plane presented later. The flow was seeded by smoke generated by mosquito repellant, which was introduced into cyclone from the inlet. The LDA system was introduced in detail in Wang *et al*. (2005). The measuring volume formed by laser beams has a minor axis of 1.18 mm and a major axis of 2.48 mm. LDA measurements of V_θ and V_z were made at 38 points of 2mm uniform spacing along a diametric axis X-X of the measurement plane at $z/R = 1$ (Figure 3-1a and 3-1c). About 50,000 samples were taken for each point of LDA measurements at a sampling rate of about 1500 samples per second, with a typical validation rate of 80 ~ 95%. The data were processed using the signal processor of the LDA system (Dantec Model 58N40 with an enhanced FVA signal processor) to obtain the power spectral density function. The selected window size was 2048 points and the frequency range of the calculated spectrum was from 0 to 1500 Hz. Thus, the frequency resolution was about 0.7 Hz, which was considered to be adequate for the present investigation. Experimental uncertainties are estimated to be within 1% for the mean velocities, $\overline{V}_\theta$ and $\overline{V}_z$, and 3% for the fluctuating velocities, $V_{\theta rms}$ and $V_{z rms}$.

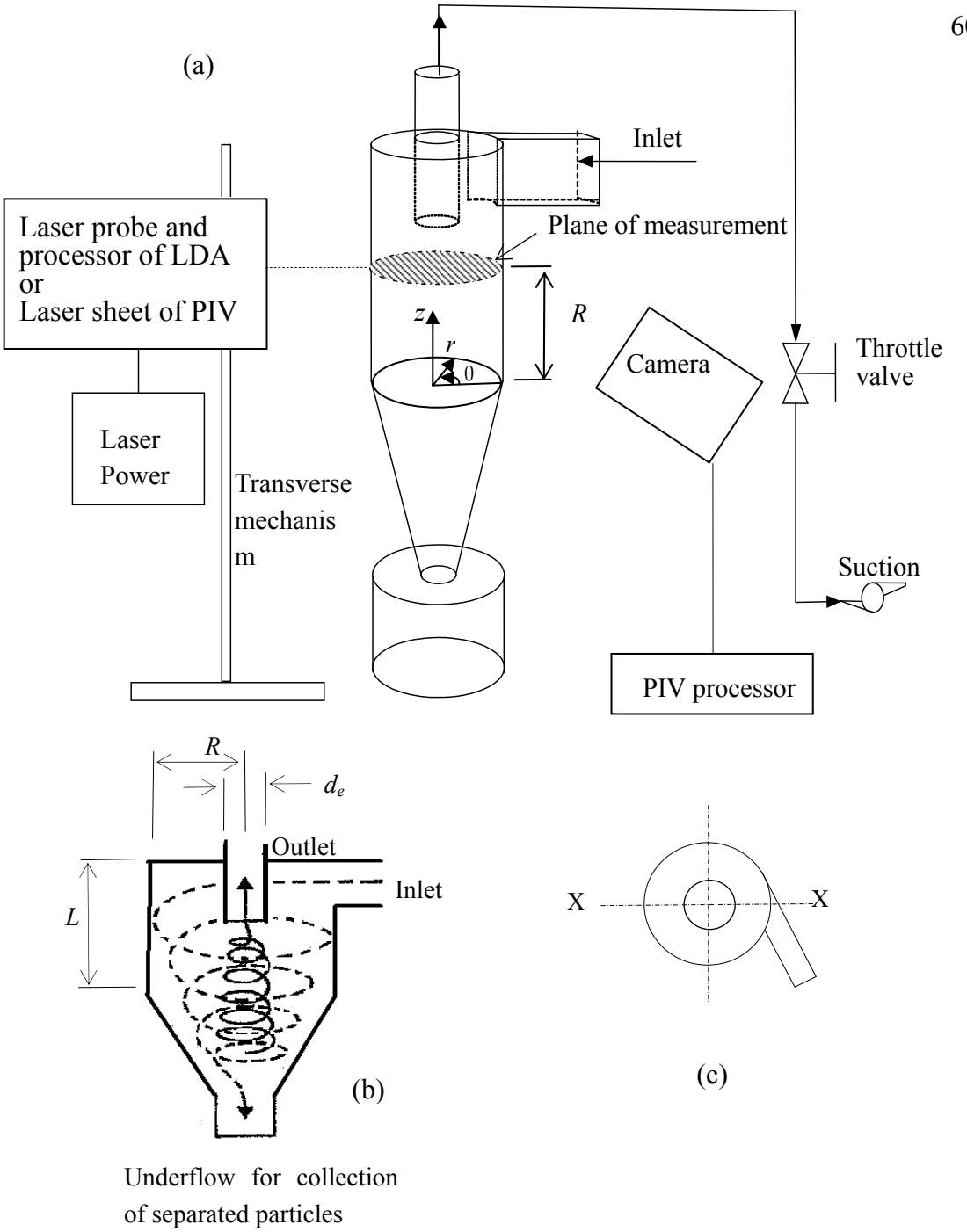

Figure 3-1 (a) Experimental setup. (b) Sketch of mean flow in the cyclone. (c) Top view of the cyclone.

In this chapter, overbar denotes time-averaging, while subscript rms represents the root mean square values.

A single hot wire operated on a constant temperature circuit at an overheat ratio of 1.8 was used to measure the fluctuating velocities, V_θ and V_z, inside the cyclone. The hot wire probe (Dantec type 55P11) is a 1.25 mm long platinum-plated tungsten

wire of 5 micron in diameter, mounted on a 1.9-mm-diameter and 30-mm-long ceramic tube. The hot wire probe was inserted into the measurement plane at $z/R = 1$ (Figure 3-1a and 3-1c) and traversed along the diametric axis X-X. Since the hot wire was used only to monitor the frequency information inside the cyclone, calibration was not needed. Hot-wire measurements were made at the same location as the LDA measurement. Signals from the circuits were offset, amplified and then digitized using a 16-channel (12 bit) A/D board and a personal computer at a sampling frequency 3.5 kHz per channel. The sampling duration was 40s.

A Dantec standard PIV2100 system was used to measure the flow velocities in the (r, θ)-plane at $z = R$ and (r, z)-plane which cut through the cyclone along the X-X axis. The flow was again seeded by smoke. The PIV system was introduced in detail in Hu *et al.* (2006). The flow illumination was provided by two New Wave standard pulsed laser sources of a wavelength of 532 nm, each having a maximum energy output of 120 mJ. The time interval to capture two sequential images was about 50 μs. Digital particle images were taken using one CCD camera (HiSense type 13, gain × 4, double frames, 1280 × 1024 pixels). A Dantec FlowMap Processor (PIV2100) was used to synchronize image acquisition and illumination. A wide-angle lens was used so that each image covered an area of 90 × 72mm of the flow field in the (r, z)-plane and an area of 112 × 88 mm in the (r, θ)-plane. The longitudinal and lateral image magnifications were identical, i.e., 0.12 mm/pixel. Each laser pulse lasted for 10 ns. An optical filter was used to allow only the green light (the wavelength = 532 nm), generated by the laser source, to pass.

The amount of distortion of the PIV images due to the curvature of the transparent cylinder of 3mm wall thickness was measured by placing a single frequency sinusoidal transmittance grating (Applied Image, SF-2.0) of two cycles per mm in the (r, z) measurement plane. Image of the grating without cyclone was captured by the camera of the PIV system and another image of the cyclone with the grating placed in the (r, z) measurement plane was also captured by the camera. The distance between the grating and the camera and the zoom ratio of the imaging lens of the camera were kept constant in the two cases. The images were compared carefully using Matlab and the maximum distortion of the grating lines due to the curvature of the transparent cylinder was found to be about 1% at the left and right end edges of the (r, z) measurement plane.

The thickness of the light sheet of the PIV system is about 2mm. The time duration between every two images recorded for every velocity vector plot is 20μs and the maximum tangential velocity of the flow is about 20m/s. The maximum distance traveled of the seeding particles due to the tangential velocity is estimated to be 0.4mm. Therefore, the seeding particles did not leave the light sheet in the recording duration for the velocity vectors in the (r, z)-plane. Since the maximum axial velocity is less than that of the tangential velocities (Figure 3-2), there is no loss of pairs in the images due to the third velocity component, V_z, for the velocity vectors in (r, θ)-plane.

The PIV data analysis is conducted by a software program, FlowManager, provided by Dantec. The peak-finding algorithm is *Peak-height validation*, which

validates or rejects individual vectors based on the values of the peak heights in the correlation data**,** where the raw vector displacement was measured. The cross correlation between the initial and final positions of the flow field, recorded on two consecutive images, was calculated using a cross-correlation algorithm, included in FlowManager. In the processing of the (r, z)-plane images, 32 × 64 rectangular interrogation areas were used. Each interrogation area included 32 pixels with 50% overlap with other areas in either of the r and z directions. The overlap is used to minimize the occurrence of erroneous vectors. The in-plane velocity vector field consisted of 79 × 31 vectors (2449 vectors in total). In the processing of the (r, θ)-plane images, the interrogation area is 32 pixels × 32 pixels ($\approx 0.06d_e \times 0.06d_e$) with 25% overlap in either of the radial and tangential directions. The ensuing in-plane velocity vector field consisted of 53 × 42 vectors (2226 vectors in total). Vectors outside the specified velocity range are most likely to be outliers. *Velocity range validation* and *moving average validation* were applied to remove false vectors (outliers) among raw velocity vectors. The rejected vectors may be replaced by vectors estimated from surrounding values. Subsequently, the *moving average filter* is used for reducing noise in the obtained vectors. In this investigation, about 24 outliers are substituted in a typical vector map, accounting for about 1% of the total number of vectors generated. The uncertainty in the velocity measurement is estimated to be 3%. The vorticity component, Ω_z, in the (r, θ)-plane was approximately derived based on particle velocities. The number of the Ω_z data was the same as that of velocity vectors. The spatial resolution for Ω_z was about 1.86 mm or $0.04d_e$.

3.3. Presentation of results and discussion

The measured $\overline{V}_\theta$ (Figure 3-2a) and $\overline{V}_z$ (Figure 3-2b) are qualitatively agreeable with previous reports such as (Solero & Coghe 2002). For the convenience of discussion, we designate the value of *r/R* at $\theta = 0$ to be positive and that at $\theta = \pi$ to be negative. Both $\overline{V}_\theta$ and $\overline{V}_z$ display a twin peak distributions, with one peak at *r/R* = -0.3 and the other at *r/R* = 0.08. The minimum of the trough in both $\overline{V}_\theta$ and $\overline{V}_z$ indicates the centre of the vortex core (Hoffmann & Stein, 2002). This minimum occurs at *r/R* ≈ - 0.1, suggesting that the centre of the vortex core does not coincide with the geometrical centre of the cyclone. Furthermore, both $\overline{V}_\theta$ and $\overline{V}_z$ do not appear symmetrical about neither *r/R* = 0 nor the centre of the vortex core. The observations are reasonable since the flow inlet (Figure 3-1a and 3-1c) is located asymmetrically about the geometrical centre of the cyclone and the air flow enters the cyclone tangentially. $\overline{V}_\theta$ around the vortex center has not been measured because of insufficient concentration of smoke particles about the vortex center.

The flow field may be separated into two regions, i.e., the outer and inner regions, by the peaks of $\overline{V}_\theta$. In the inner or core region, i.e. *r/R* < -0.3 and *r/R* > 0.08, $\overline{V}_\theta$ increases approximately linearly with the distance from the centre of the vortex core, displaying similarity to a rigid body rotation or a forced vortex. In the outer region of the vortex, i.e., -1 < *r/R* < -0.3 and 0.08 < *r/R* < 1, $r^{0.7}\,\overline{V}_\theta$ ≈ constant, similar to previous report by Solero & Coghe (2002). The highest $\overline{V}_\theta$ occurs at the interface of the two regions and is approximately $1.66U_{in}$.

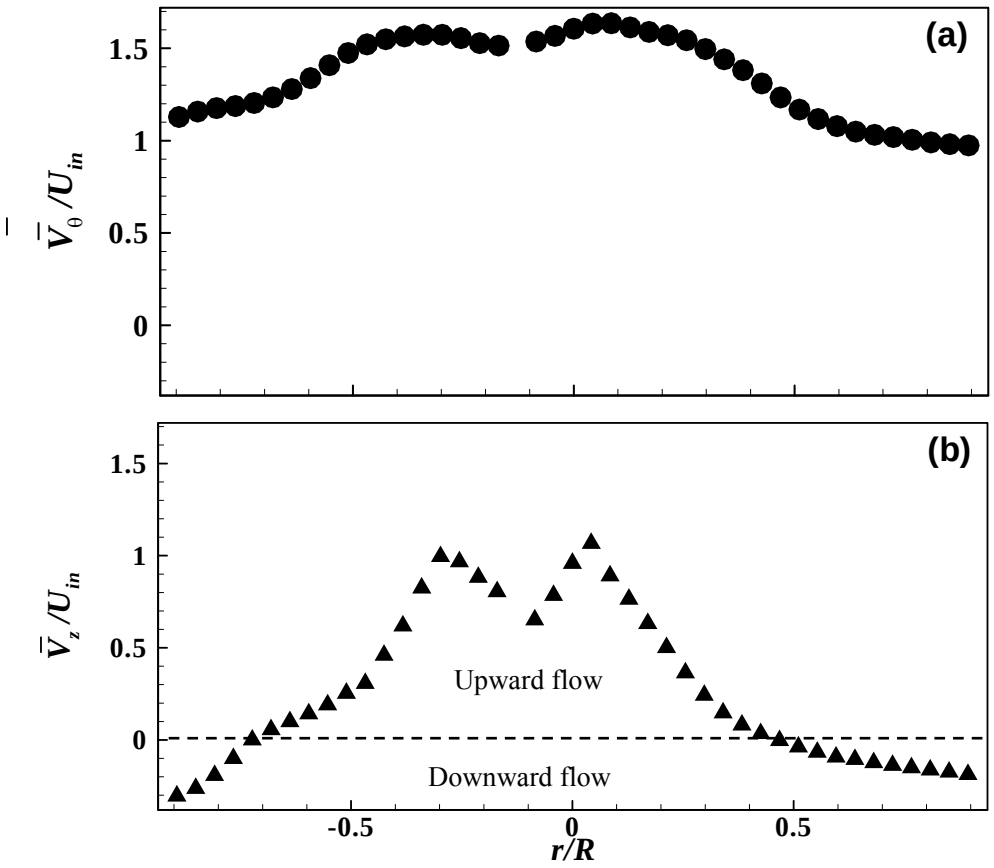

Figure 3-2 Radial distribution of (a) mean tangential velocity, $\overline{V}_\theta$, and (b) mean axial velocity, $\overline{V}_z$, in the (r, θ)-plane (z/R = 1). Re = 47000.

In the central region, the axial velocity $\overline{V}_z$ (Figure 3-2b) points up and is approximately linearly proportional to the distance from the centre of the vortex core. The lower axial velocity towards the centre of the vortex core reflects the loss of swirl in the exit pipe, resulting in an adverse pressure gradient at the centerline of the cyclone (Hoekstra *et al.* 1999). In the region close to the wall, $\overline{V}_z$ is downward-directed towards the conical section in an annular region, i.e., $-1 < r/R < -0.72$ and $0.43 < r/R < 1$, and is otherwise upward-directed. The observed distribution of $\overline{V}_z$ is reasonable. Once entering the cyclone tangentially, the air flow moves towards the wall, forming an outer downward vortex flow under the strong action of the centrifugal force. After reaching the bottom the flow turns upward.

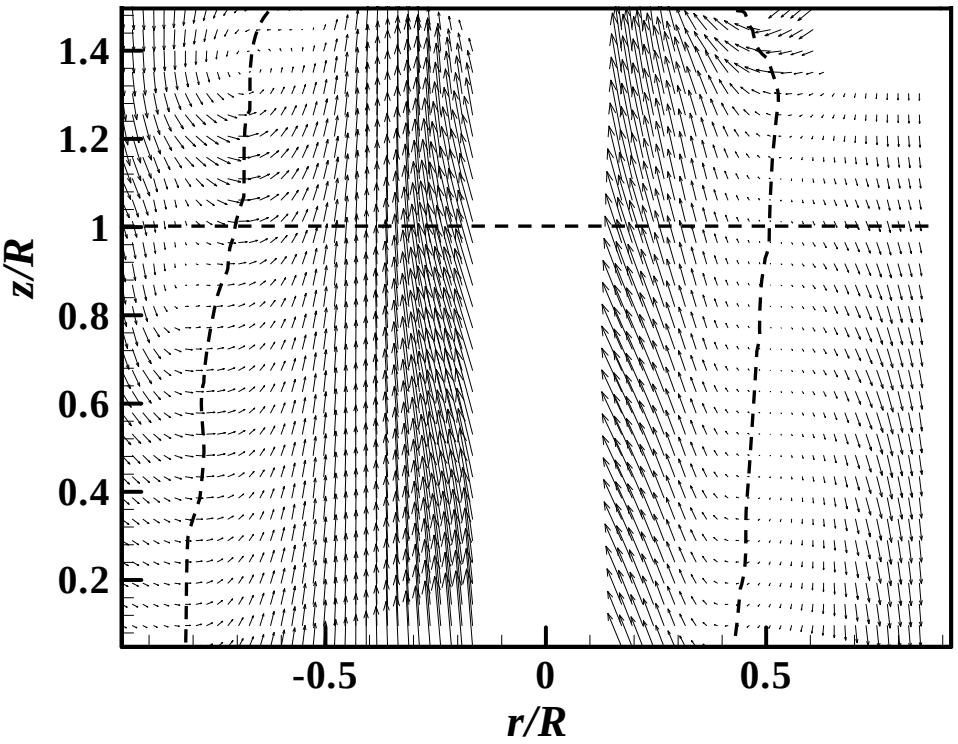

Figure 3-3 Averaged velocity vectors in the (*r, z*)-plane of the cyclone chamber measured using PIV, *Re* = 47000 and *S* =3.0, *Re* = 47000.

Figure 3-3 presents the velocity vectors in the (*r*, *z*)-plane averaged from 278 plots of PIV-measured instantaneous velocity vectors. Two curves indicate the location of zero axial velocity, i.e., $\overline{V}_z = 0$, indicating the interface between the regions of upward and downward axial flows. Apparently, the location of $\overline{V}_z = 0$ depends on *z/R*. At *z/R* = 1, $\overline{V}_z = 0$ occurs at *r*/*R* = -0.72 and 0.47, internally consistent with the radial distribution of LDA-measured $\overline{V}_z$. Seeding particles in PIV measurements were measured using a digital microscope and were found to be a few microns in diameter. The particle Stokes numbers of the seeding particles were calculated to be less than 0.1. It is possible that the blank strip (r/R < 0.1) resulted from very low velocity near the axis of the cyclone. A close examination of the vectors suggests that the axes of both the upward and downward swirl flows in the cylindrical body of the cyclone are tilted and shifted away from the geometrical axis

of the cyclone chamber. Using LDA in a cylinder-on-cone cyclone, Peng *et al*. (2001) also observed the asymmetry of axial velocity of the flow below the vortex finder.

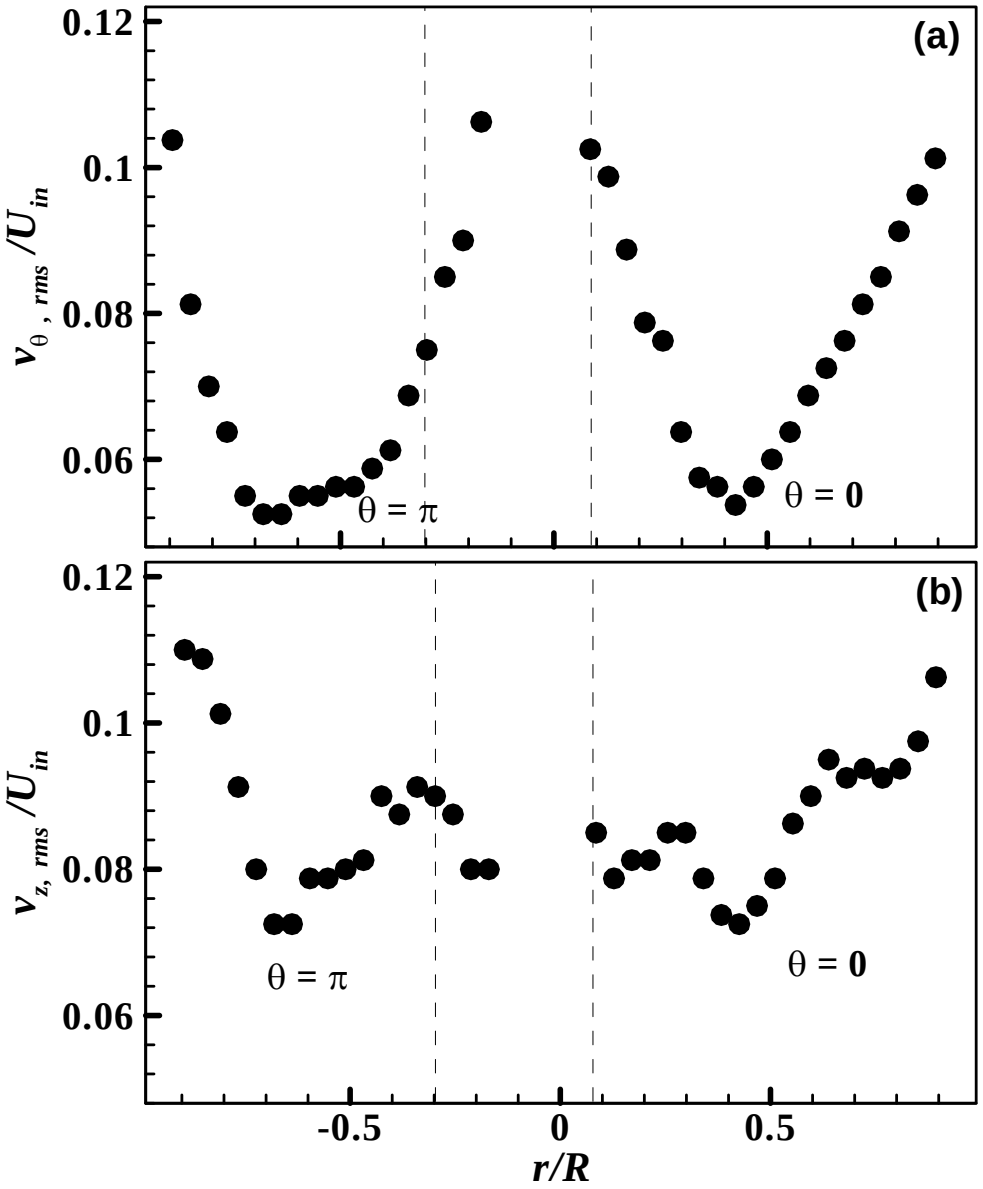

Figure 3-4 Radial distribution of (a) $V_{\theta,rms,}$ and (b) $V_{z,rms}$ in the (r, θ)-plane (z/R = 1). Re = 47000.

The fluctuating tangential velocity, $v_{\theta,rms}$ (Figure 3-4a), displays a W-shape distribution, rising markedly near the wall and the core. The results suggest a highly turbulent boundary layer over the cyclone wall and a highly turbulent inner precession vortex core. The large $v_{\theta,rms}$ towards the inner region is probably linked to the loss

of swirl in the exit pipe (Hoekstra *et al*. 1999). In contrast to the variation of $v_{\theta,rms}$, $v_{z,rms}$ displays peaks at *r/R* ≈ - 0.3 ~ 0.4 and 0.2 ~ 0.3, where $\overline{V}_z / U_{in}$ (Figure 3-2b) exhibits large gradients. The highly sheared flow is associated with an instability, resulting in large-scale vortical structures, as confirmed later by measured instantaneous vorticity contours. These vortical structures should be responsible for the peaks in $v_{z,rms}$.

Figure 3-5 presents the power spectral density function, E_{v_θ}, of V_θ measured using LDA at various *r/R* along the axis X-X of the measurement plane (Figure 3-1c). In the figures, *f* is frequency (Hz). One pronounced peak occurs at $St_1 = f_1 2R/U_{in}$ = 0.53 in E_{v_θ} at all positions except *r/R* ≥ 0.68. Another pronounced peak is identifiable at $St_2 = f_2 2R/U_{in}$ = 0.62 (Figure 3-5), though only over the upward flow region, i.e., *r/R* = 0.26 ~ 0.47. The observed St_2 agrees quite well with the Strouhal number (= 0.6) of the precessing vortex core in a similar cyclone (Hoekstra *et al.* 1999). Alekseenko *et al.* (1999) measured a Strouhal number of 0.85 in a helical flow at *S* = 1.9, 1.19 and 3.8 (*Re* = 14000 ~ 45000), which is significantly higher than the present St_1 and St_2. The deviation is expected in view of very different fluid dynamics between the flow in a cylinder-on-cone cyclone and a simple helical flow.

Previous investigations, (Derksen & Akker 2000), (Hoekstra *et al*. 1999), (Yazdabadi *et al*. 1994) and (Solero & Coghe 2002), on reverse-flow cyclone have reported one dominant frequency only, i.e., the one that is observed only in the

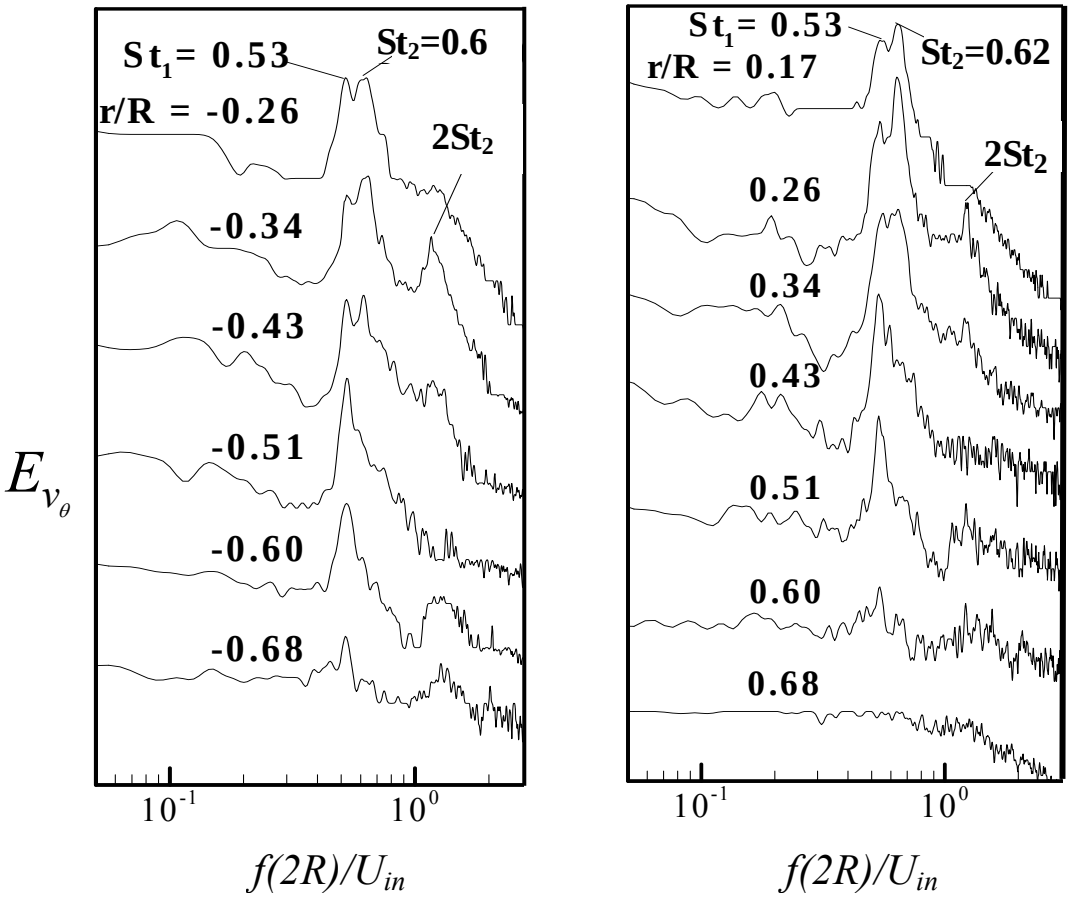

Figure 3-5 Power spectral density functions of V_θ, measured along the axis X-X (Figure 3-1c) in the (r, θ)-plane (z/R = 1), at various r/R using LDA. Re = 47000.

upward flow region. A scenario is proposed for the present observation of two dominant frequencies. Under the influence of the tangential flow momentum at the cyclone inlet, the flow within the cyclone is likely to precess as a whole, thus producing the peak in E_{v_θ} at St_1. This precessing flow spirals downwards. The region of upward directed flow also precesses. The two precessions, one spiral down and the other spiral up, are unlikely to have the same precessing frequency. In fact, being relatively small in diameter, the upward directed flow should have a higher precessing frequency due to the conservation of the moment of momentum if the wall shear force on fluid is neglected. Therefore, in addition to swirling with the whole

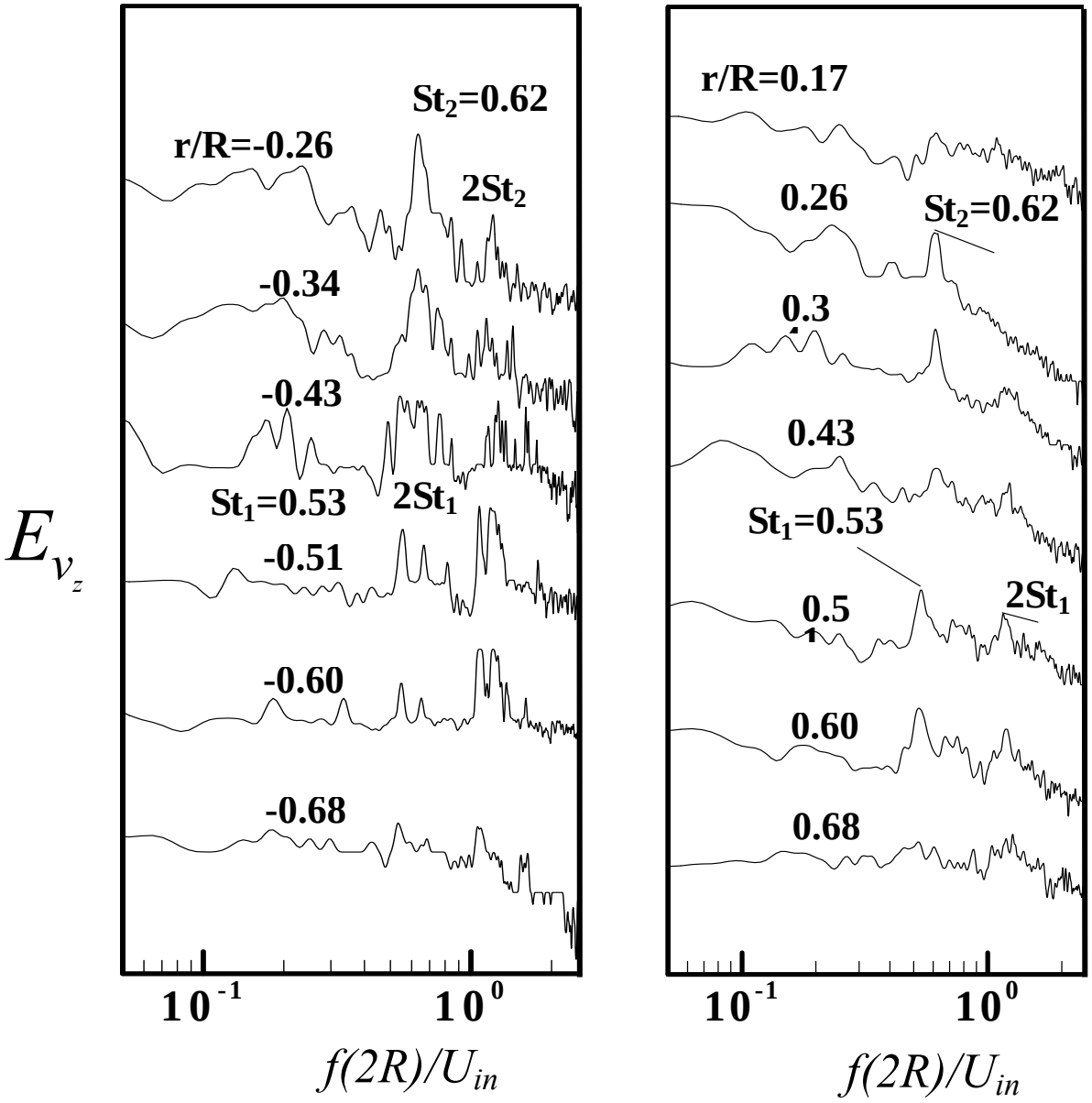

Figure 3-6 Power spectral density functions of V_z measured along the axis X-X (Figure 1c) in the (r, θ)-plane (z/R = 1), at various r/R using LDA. Re = 47000.

flow field, the region of the upward directed flow should precess at St_2, which is higher than St_1. Near the cyclone wall, the peak at St_1 is not discernible probably because of the boundary layer effect.

The V_z-spectrum, E_{v_z} (Figure 3-6), again displays a peak at St_2 in the region of $r/R \leq 0.47$, where the flow is upward. However, the peak at St_1 is only discernible for $0.47 < r/R < 0.68$. Furthermore, the peaks are appreciably less pronounced,

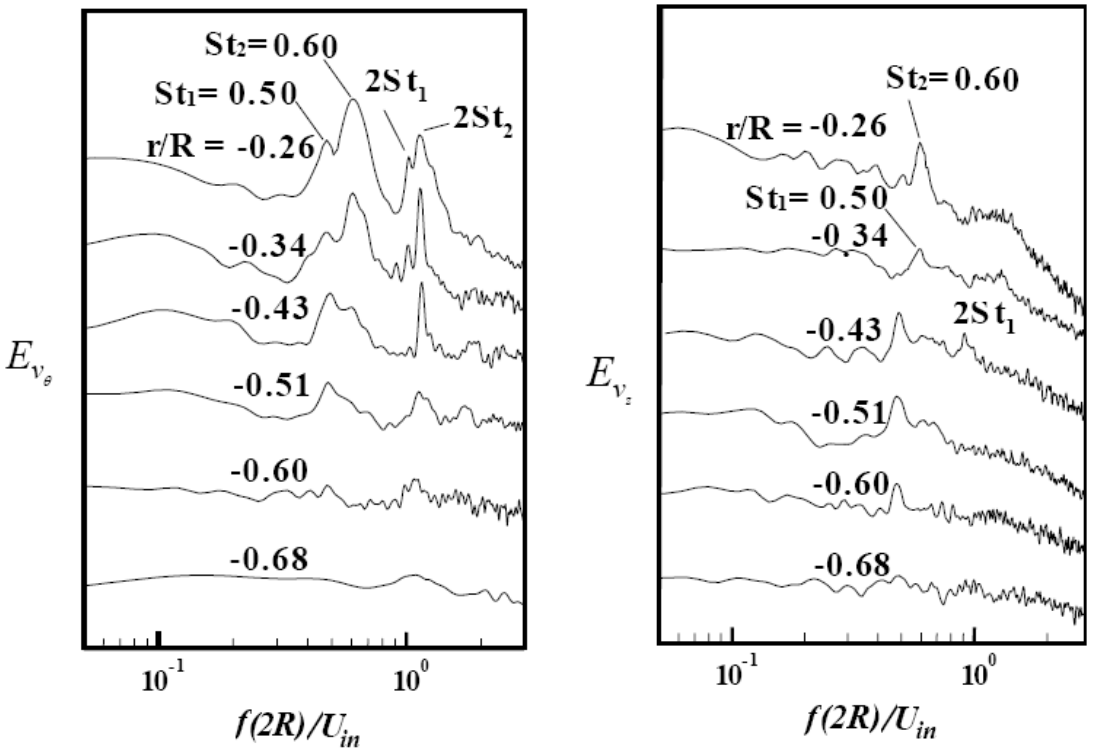

Figure 3-7 Power spectral density functions of V_θ and V_z measured along the axis X-X (Figure 3-1c) in the (r, θ)-plane (z/R = 1), at various r/R using hot-wire anemometry. Re = 47000.

compared with those in E_{v_θ}. The observation is probably due to the fact that the dominant frequencies, St_1 and St_2, are primarily due to the precessing downward and precessing upward motions, respectively. The precessing motions are sensitive along the V_θ direction, not at the V_z direction. As a result, the peak at St_1 cannot be detected in the region of upward flow and even at r/R = 0.68, where this peak is clearly discernible in E_{v_θ} (Figure 3-5). Chao *et al*. (Chao *et al.* 1991) observed two dominant frequencies in the axial velocity spectra within a swirl tube. They proposed that one of the frequencies was due to the precessing vortex core and the other to an azimuthal instability connected to the contraction downstream. Apparently, a swirl tube is rather different from a cylinder-on-cone cyclone; there is no reverse flow in the swirl tube, which is distinct from the present flow. Figure 3-7 shows the spectra of

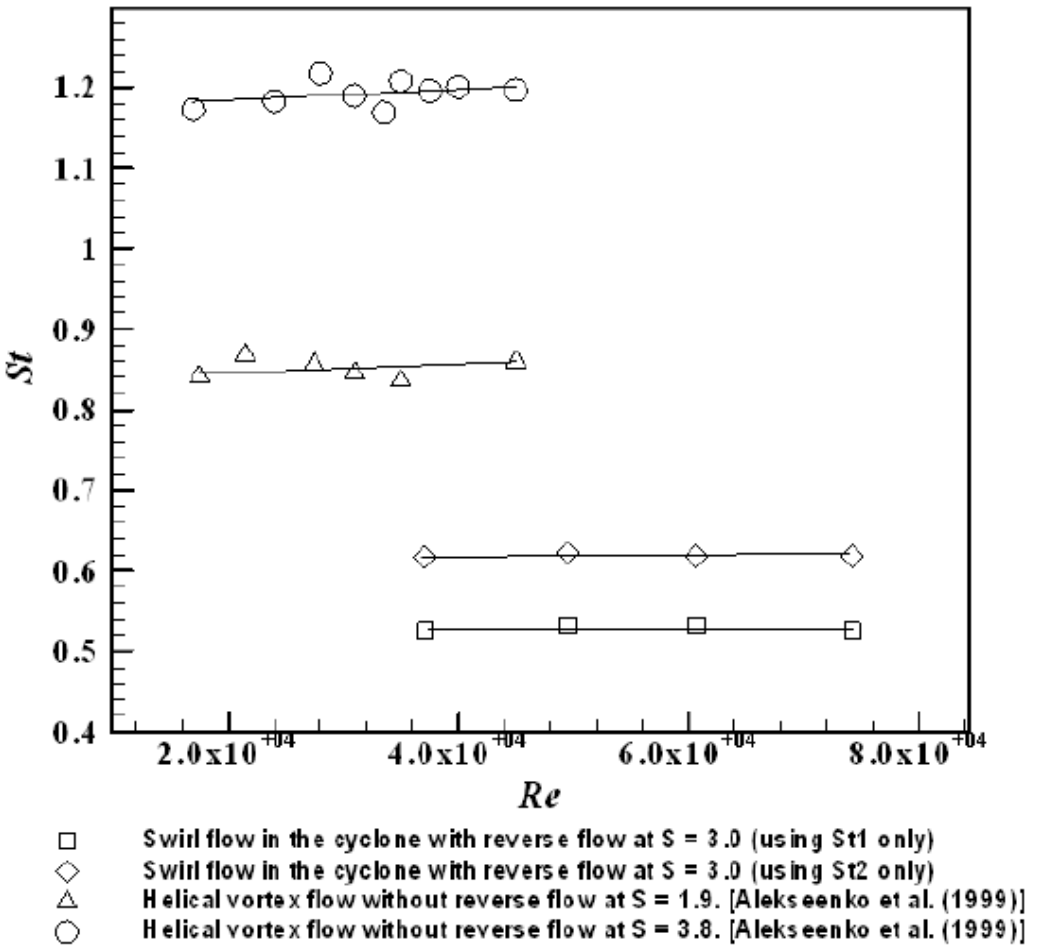

Figure 3-8 Strouhal numbers of the swirl flow in the present cyclone at four different Reynolds numbers.

hotwire-measured V_θ and V_z, which display two pronounced peaks at the same frequencies as those given in the LDA data. Derksen (2003) also measured two predominant frequencies at St = 0.7 and 1.58 in the vortex core of a cylinder-on-cone cyclone with reverse flow at Re = 280,000 and Swirl number = 3.9. Their experimental data was given only at one point near the center in the mid plane of the conical section of the cyclone. No explanation was provided.

Additional experiments were conducted at three different Reynolds numbers Re = 37100, 60000 and 74000. The simultaneous presence of two peaks in the spectra was again measured, as shown in Figure 3-8. Apparently, the Strouhal numbers appear

independent of *Re*. As it can be noticed, the measured St_1 and St_2 appears to be constant for the *Re* range presently investigated, significantly lower than Alekseenko *et al.*'s measurements, i.e. St = 0.85 at S = 1.9 and 1.19 at S = 3.8 (Re = 14000 ~ 45000), which is expected in view of very different fluid dynamics between the flow

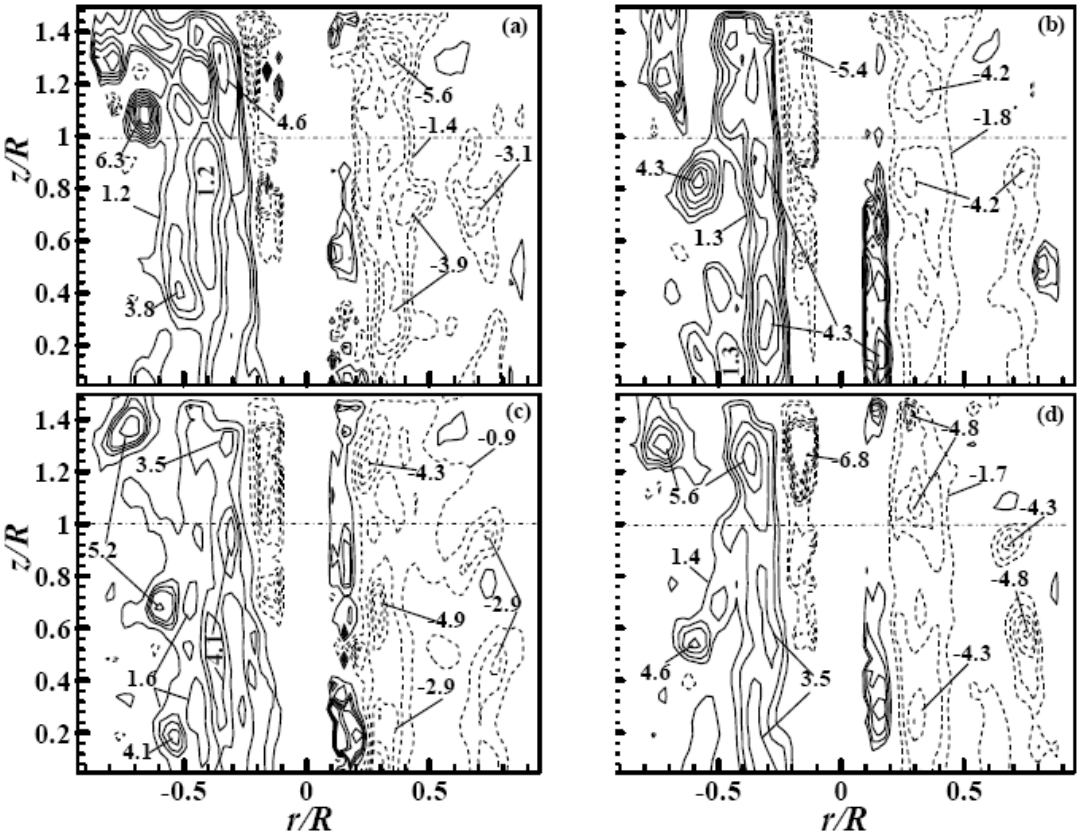

Figure 3-9 Contours of PIV-measured instantaneous normalized vorticity in (r, z)-plane. Re = 47000 and S =3.0. The (r, θ)-plane, where both PIV and LDA measurements were conducted, is marked by ----------

in a cylinder-on-cone cyclone and a simple helical flow.

In order to gain a better understanding of the turbulent flow structure in the cyclone, the contours of PIV-measured instantaneous vorticity, $\Omega_z 2R/U_{in}$, in the (r, z)-plane are examined, as illustrated in Figure 3-9. The normalized vorticity in the core region is opposite in sign to that in the outer region, suggesting that the precession of the overall flow (spiral downward) in the cyclone chamber is opposite

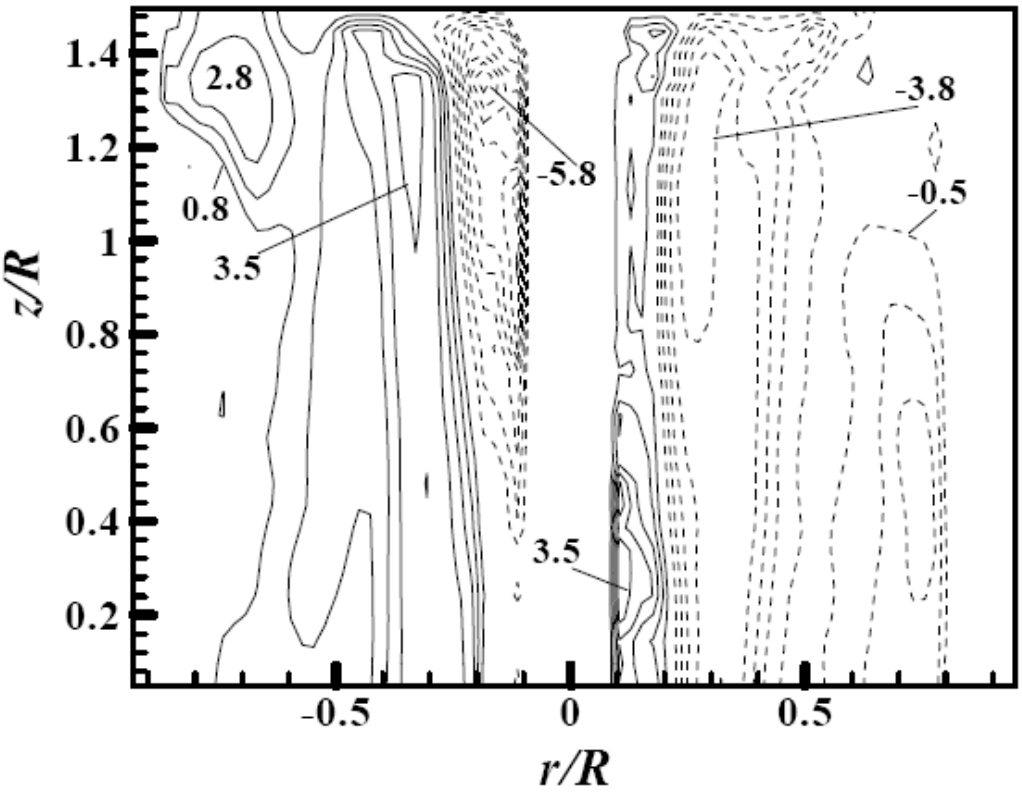

Figure 3-10 Averaged vorticity contours measured using PIV in the (r; z)-plane of the cylinder chamber. Re = 47000 and S =3.0.

in sense to the precession of the upward flow, which will be re-confirmed by the contours of axial vorticity measured in the (r, θ)-plane. The maximum concentrations of vorticity in the outer region occur in the immediate neighborhood of the inner region. This is more evident in the contours of vorticity (Figure 3-10) averaged from 278 plots of instantaneous vorticity measurements. The maximum concentrations of vorticity in the outer region coincide with the location where the maximum gradient of LDA-measured $\overline{V}_z$ occurs.

Figure 3-11 presents the contours of typical instantaneous axial vorticity, $\Omega_z 2R/U_{in}$, measured in the (r, θ)-plane (z/R = 1). The inner region is characterized by highly concentrated positive $\Omega_z 2R/U_{in}$, with the maximum occurring about r/R = 0,

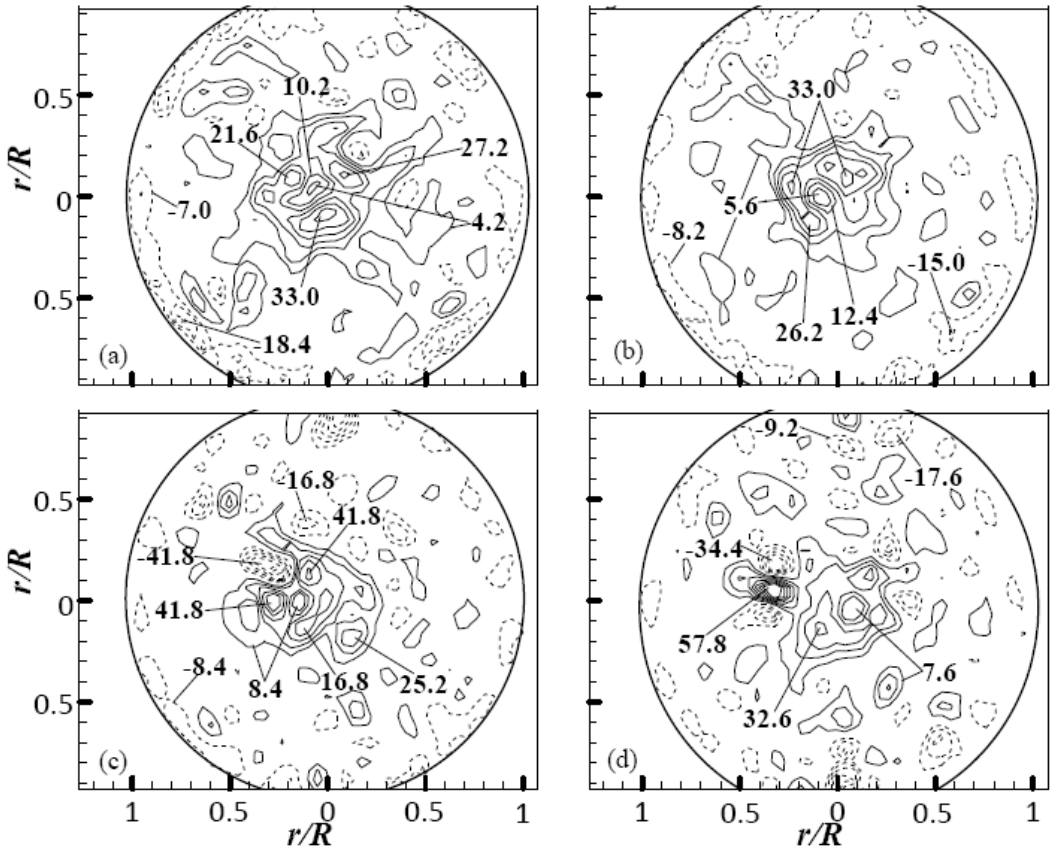

Figure 3-11 PIV-measured instantaneous vorticity contours in the (r, θ)-plane (z/R = 1). Re = 47000 and S =3.0.

exhibiting the characteristics of the precessing vortex core. On the other hand, the opposite-signed (negative) $\Omega_z 2R/U_{in}$ tends to dominate near the wall (r/R = 1), though significantly less concentrated than that in the inner region. Between the wall and inner regions (the outer region), the vortical structures of both signs are evident, again with less concentrated $\Omega_z 2R/U_{in}$ than in the inner region. The observation is consistent with the fact that the two precession motions in the cyclone are opposite in the sense of rotation. The above characteristics are better reflected in the contours of $\overline{\Omega}_z 2R/U_{in}$ (Figure 3-12) averaged from 278 plots of instantaneous vorticity data. The maximum $\overline{\Omega}_z 2R/U_{in}$ is shifted by $0.05R$ from the geometric centre of the cyclone chamber.

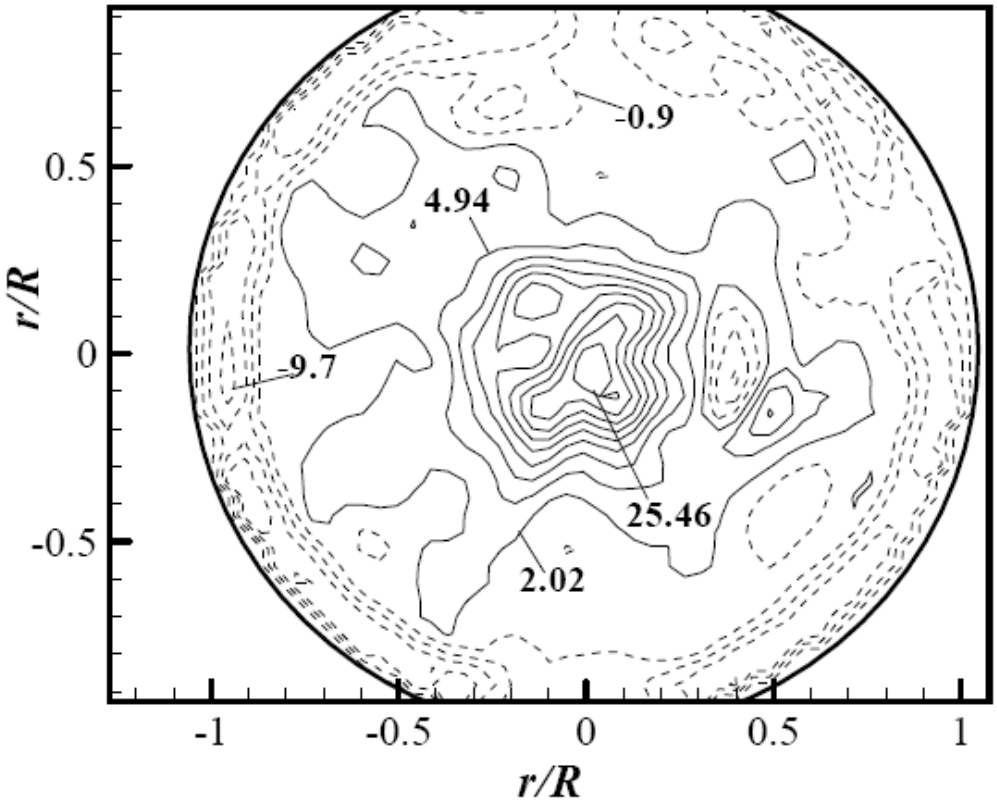

Figure 3-12 Averaged vorticity contours in the (r, θ)-plane (z/R = 1 measured using PIV. Re = 47000 and S =3.0.

Both the averaged and instantaneous vorticity contours suggest the presence of relatively large-scale structures encircling the vortex core in the annular region $|r/R| < 0.8$. These structures appear quasi-periodical and are probably responsible for the pronounced peak at St_1 = 0.53 in E_{v_θ} (Figure 3-5). Meanwhile, strong vortical structures that occur in $|r/R| < 0.4$ may account for the peak in E_{v_θ} (Figure 3-5) at St_2 = 0.62 that occur for r/R = 0.26 ~ 0.47. Note that the averaged vorticity contours shown in Figure 11 conform to the distribution of $V_{\theta,rms}$ (Figure 3-4a). The concentration in $\overline{\Omega}_z 2R/U_{in}$ for $0.8 < |r/R| < 1$ corresponds to the large $V_{\theta,rms}$ near the wall; $\overline{\Omega}_z 2R/U_{in}$ appears low in the annular region of $0.4 < |r/R| < 0.7$, where $V_{\theta,rms}$ is also small; $\overline{\Omega}_z 2R/U_{in}$ is large for $|r/R| < 0.2$, where $V_{\theta,rms}$ is large.

3.4 Conclusions

The turbulent flow structure within a cyclone was experimentally investigated on a laboratory-scale cylinder-on-cone cyclone model based on LDA and PIV measurements. The work leads to the following conclusions:

1 The flow has been characterized in detail in terms of the mean circumferential and axial velocities and their rms values, along with their topological features in the (r, θ)-plane and the (r, z)-plane. The rms circumferential and axial velocities are both high near the wall because of the turbulent boundary layer. The rms circumferential velocity is large in the core region, while the rms axial velocity displays a peak at $r/R \approx 0.3$, which is ascribed to the instability associated with the large velocity gradient immediately outside the vortex core region. The precession axis of the flow is found to be tilted and displaced from the geometric centre of the cyclone. The data obtained from the measurements provide a data base for numerical modeling of the flow in a cylinder-on-cone cyclone.

2 Two dominant frequencies, St_1 and St_2, are observed based on the power spectral density functions of the tangential and axial fluctuating velocities. The lower frequency St_1 is observed in both of the outer and inner regions of the flow. This frequency is ascribed to the downward precession of the flow, within the cyclone, as a whole. To our knowledge, this frequency has been observed for the first time in the flow of a cylinder-on-cone cyclone. The

higher frequency St_2 occurs in the vortex core region as a result of the upward precession of the vortex core, as previously reported. The two precession motions are opposite in the sense of rotation. The two fluid motions, one spiral down and the other spiral up (Figure 3-3), are unlikely to have a 'black-and-white' border between them; there should be a transition region where both motions could be present. Indeed, we have observed the twin-peak distribution in E_{v_θ} (Figures 3-5 and 3-7) over r/R ≈ 0.26 ~ 0.43 in the upward flow region. However, the proposed explanation has yet to be confirmed by more experimental or numerical data. It has been well known that large-scale vortical structures may result from shear layer instabilities (Zhou & Antonia, 1995, Wang & Zhou 2005, Wang *et al.* 2005). Naturally, the shear layer due to the occurrence of the spiral-up motion and spiral-down motion could lead to the formation of vortical structures. Nevertheless, more experimental evidence is required to confirm the present proposition.

CHAPTER 4

SWIRL NUMBER EFFECT ON TURBULENT FLOW STRUCTURE IN A CYCLONE

4.1. Introduction

Cyclone separators are most widely used in engineering as industrial gas-cleaning devices, e.g., vehicle exhaust-gas cleaning devices, vacuum cleaners, incinerators and boilers. The basic cyclone design has evolved little since its first application about one hundred years ago, largely attributed to the complexity and inadequate knowledge of the turbulent swirling flow and instabilities such as vortex breakdown and precessing vortex core within a cyclone. These instabilities are responsible for extra losses, producing a high pressure drop and a high level of turbulence and mixing in the cyclone (e.g. Biffin *et al*. 1984). As a result, there are problems in the use of cyclones. A typical example is the incorrect prediction of the separation efficiency of submicron particles in a common industrial cyclone separator. This calls for the need to gain an in-depth understanding of fluid dynamics, including the turbulent flow structure, which is crucial for improving the theoretical model of the separation efficiency (Bose *et al.* 2010).

The swirl flow in a cyclone separator is characterized by a strong tangential velocity component, a relatively small axial component and a very small radial

component, as illustrated in Fig. 4-1. One of the important characteristic parameters for the swirl flow or cyclone flow is the swirl number, *S*, defined as the ratio of the average angular momentum to the average axial momentum of the flow times the inlet hydraulic radius of the cyclone. In isothermal operation, *S* is determined by the geometrical parameters of a cyclone, given by $\pi d_e R/2A$, where d_e is the diameter of the cyclone outlet and *R* is the radius of the cylindrical chamber of the cyclone, and *A* is the inlet area of the cyclone. The choice of *S* may affect the separation efficiency and the pressure drop of the cyclone. In general, a higher *S* increases the separation efficiency of heavy particles and also corresponds to a higher pressure drop.

The phenomena of vortex breakdown and precessing vortex core in a swirl flow were observed and investigated rather extensively in the past (Chanaud 1965, Cassidy & Falvey 1970, Gouldin *et al.*1984, Harvey 1962, Sarpkaya 1971). Toh *et al*. (2010) provided a comprehensive review on this flow. Alekseenko *et al.* (1999) performed theoretical and experimental investigation of steady helical vortices in a swirl flow formed in a cylindrical chamber of square cross section. Five different swirl numbers from 1.0 to 3.8 were investigated. They observed only one precessing vortex frequency. The Strouhal number, *St* ($\equiv f_{prec}2R/U_{in}$, where f_{prec} is the precessing frequency of the vortex and U_{in} the inlet velocity) was almost constant for the range of the inlet Reynolds number *Re* ($\equiv U_{in}\,2R/\nu$, where ν is the kinematic viscosity of fluid) = 1.4 ~ 4.5 x 10^4, though exhibiting a dependence on *S*. Both Alekseenko *et al.* (1999) and Chao *et al.* (1991) pointed out that the flow structure in a swirl flow depended on *S* as well as on *Re* and the conditions at the exit and the downstream geometry of a

swirl tube. Lu *et al*. (2005) noted through large-eddy simulations that the swirl number played an important role in the development of the swirl flow in a swirl tube. The helical structure, arising from the vortex breakdown, grew downstream in terms of size and circulation at $S = 0.5$, but shrank at $S = 0.3$. At smaller S, the observation was connected to the precession of the vortex core around the centreline. The precession resulted in the intermittent occurrence of vortex breakdown and subsequently caused the helical structure formed upstream of the time-mean flow direction of the swirl tube to vanish rapidly downstream. On the other hand, the larger swirl number acted to maintain flow coherence.

Flow in a cylinder-on-cone cyclone is another type of swirl flow, rather different from the swirl flow discussed above. This flow is associated with a reverse flow, while the other is not. For the convenience of discussion, we hereinafter refer to the former as the cyclone flow and the latter as the swirl flow, unless otherwise stated. As such, one may surmise that the dependence of the flow structure on S in the cyclone flow might not be the same as in the swirl flow. The questions may naturally arise: how does the reverse flow in the cyclone influence the relationship between the cyclone flow structure and swirl number? There have been a number of numerical and experimental investigations on the turbulent flow structure in cyclones. Zhou and Soo (1990) and Hsieh and Rajamani (1991) studied numerically fluid flows and particle motions in the cyclone flow on the assumption of axisymmetrical flow, notwithstanding the fact that the actual flow in a cyclone with reverse flow was not found to be axisymmetrical (e.g. Wong *et al.* 2007). Their results deviated rather

substantially from experimental data in terms of velocity distributions. Using the second-order Reynolds-stress turbulence model and large eddy simulation, respectively, Cristea *et al*. (1994) and Derksen (2003) achieved reasonable agreement with measured time-averaged and fluctuating velocities in cyclones. None of these investigations examined the effect of S on the flow.

The presence of the reverse flow in a cyclone flow also raises the issue whether the dependence of St on S would be the same as in the swirl flow. Significant attention has been devoted in literature to the Strouhal number in the cyclone flow because of its engineering significance. For example, a higher Strouhal number of the cyclone flow is beneficial to enhancing the mixing of different phases in the cyclone. Derksen and Akker (2000) noted numerically that the main vortex core moved about the geometrical axis of the cyclone flow in a quasi-periodic manner, and St was found to be 0.53 at $Re = 1.4 \times 10^4$ and $S = 2.1$. Hoekstra *et al.* (1999) observed experimentally $St = 0.6$ in a cyclone, whose geometry was similar to that used by Derksen and Akker, at $Re = 2.5 \times 10^4$ and $S = 1.8$, 2.2 and 3.1. Solero and Coghe (2002) experimentally investigated both single- and two-phased flows in a cylinder-on-cone cyclone. In the single phase gas flow, St was found to be 0.62 at $S = 2.39$ and $Re = 3.76 \times 10^4$ and 1.25×10^5. Hoekstra's (2000) measurements of St was 0.7 in a cyclone at $S = 3.93$ and a comparable Re. In Wong *et al.*'s (2007) LDA and PIV (particle imaging velocimetry) measurements at $S = 3$ in a cylinder-on-cone cyclone, two distinct Strouhal numbers St_1 (= 0.53) and St_2 (= 0.62) were detected for the Re range of $3.71 \sim 7.42 \times 10^4$. St_2 occurred in the vortex core region, as a result of the upward precession of the vortex

core, whilst St_1, observed in both the outer and inner regions of the vortex core, was ascribed to the downward precession of the flow. Evidently, there is a considerable scattering in the measured *St*, ranging from 0.53 to 0.70. Different experimental conditions and uncertainties could not entirely account for the large disparity in measured *St*. Nor could the *Re* effect. Wong *et al*.'s measurements at a fixed *S* obtained in the same experimental facilities suggested little change in *St* for the *Re* range of 3.7 ~ 7.4 x 10^4. Then, one wonders whether the scattered *St* is linked to the effect of the swirl number, which has not been previously investigated for the cyclone flow.

This work aims to address the issues raised above, specifically, to gain an improved understanding of the turbulent flow structure and to determine its possible dependence on the swirl number in the swirl flow within a cylinder-on-cone cyclone. The swirl number range examined is from 2.4 to 5.3. The Reynolds number is 7.42 x 10^4. The Reynolds number used in the experimental study is typical for many centrifugal separators and dedusters applied in wood works, boilers, power coating, chemical and pesticides, plastic, foundry, carbon processing, grain handling, cement industries and many more. PIV and LDA techniques are deployed to measure the flow. Both mean and fluctuating velocity and vorticity fields are examined carefully and discussed, along with the probability density function, skewness, flatness and spectra of fluctuating velocities.

4.2. Experimental details

Figure 4-1a shows schematically the experimental setup, including an open-loop

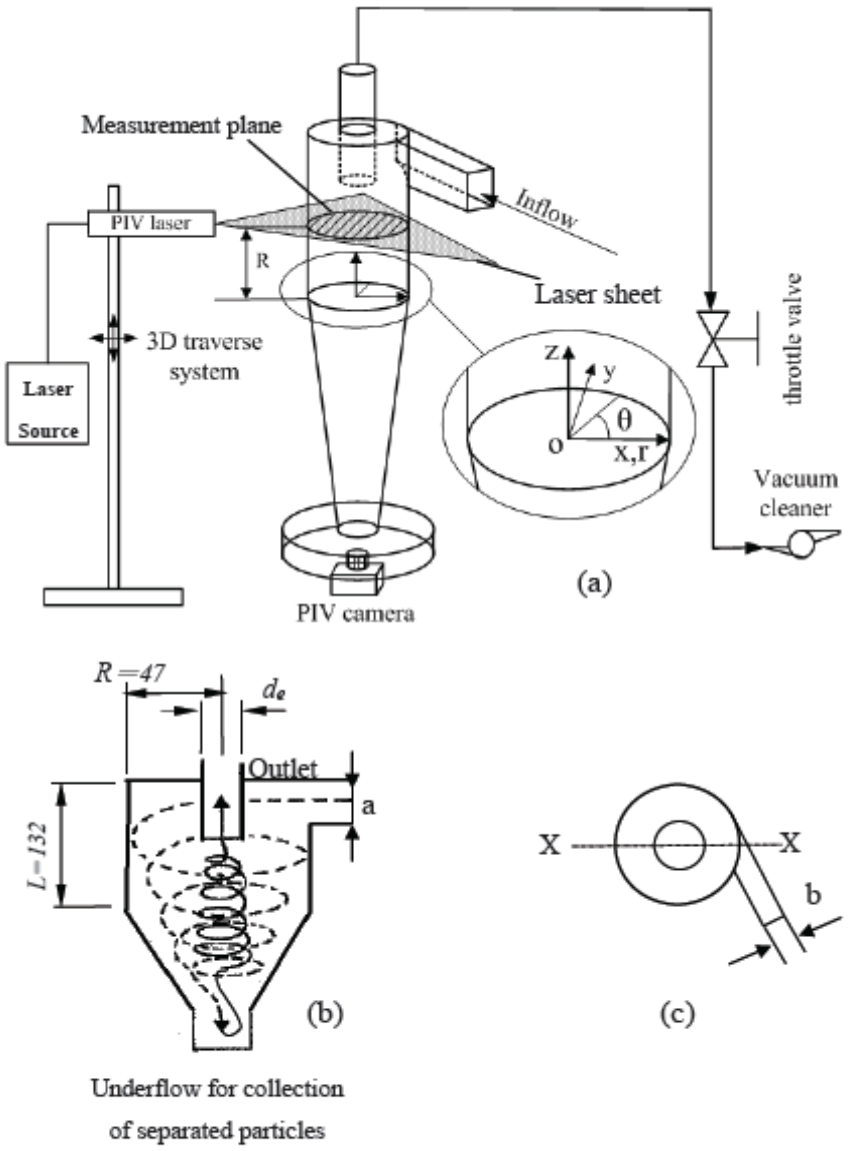

Fig. 4-1 (a) Schematic of experimental setup and the definition of the coordinate system; (b) sketched mean flow (length unit in mm); (c) the top view of the cyclone where X-X indicates the path the LDA probe was traversed across.

cylinder-on-cone cyclone model of laboratory scale. The model was made of transparent acrylic. The radius R and length L of the cylindrical chamber were 47 mm and 132 mm, respectively; the diameter d_e of outlet circular cross section was 44 mm, and the area A of inlet rectangular cross section (50 mm x 22 mm) was 1100 mm^2. An equivalent hydraulic inlet diameter is the diameter of a cylindrical inlet pipe having the same cross sectional area to perimeter ratio as the rectangular inlet pipe

used in the experiment. The equivalent hydraulic diameter is calculated as 4 x A/p = 30.6 mm where p is the perimeter of the inlet rectangular pipe. S was varied from 2.4 to 5.3 by varying the sizes of the inlet width and outlet diameter of the cyclone. The cyclone flow was produced through suction generated by a vacuum cleaner with a power of 1.5kW. Its speed could be controlled via a throttle valve. The mean flow direction is indicated in Fig. 4-1b. The wind velocity at the cyclone inlet was rather uniform and measured by a pitot-static tube connected to a micro-manometer (Furness FCO510). Experiments were conducted at Re = 7.4 x 10^4.

The coordinate system, (r, θ, z), is defined such that its origin is at the center of the joint plane between the cylindrical and conical sections of the cyclone (Fig. 4-1a). The instantaneous velocity components in the r, θ and z directions are designated as V_θ, V_r and V_z, respectively. An instantaneous velocity may be decomposed into an averaged component and a fluctuating component, viz. $V_\theta = \overline{V}_\theta + v_\theta$, $V_r = \overline{V}_r + r_r$, $V_z = \overline{V}_z + v_z$, where overbar denotes averaging over an adequately long time, and v_θ, r_r and v_z are the fluctuating velocity components, out of which the root mean square values, $v_{\theta,rms}$, $v_{r,rms}$ and $v_{z,rms}$, may be calculated.

A two-component LDA system (Dantec Model 58N40) with an enhanced FVA signal processor was used to measure the tangential and axial flow velocity components, V_θ and V_z, respectively, along the axis X-X in the (r, θ)-plane at z/R = 1 (Fig. 4-1c), which was the mid section of the cylindrical chamber. At this section, the possible perturbation of inlet and outlet to flow is minimum. The laser source was an argon ion laser (Spectra-Physics, Stabilite 2017) with a maximum power output of

4 W. The measuring volume had a minor axis of 1.18 mm and a major axis of 2.48 mm (Wang *et al*. 2005). The LDA optic probe was mounted on a computer-controlled 3D traversing system with a maximal positional error of ± 0.1 mm. Adequate seeding is crucial for LDA measurements in the air flow. Fog generated from Paraffin oil by a smoke generator was tested first, which failed to provide a sufficient seeding concentration because particles in the cyclone chamber were continuously taken out by the vacuum cleaner. Mosquito-repellant-generated smoke released near the inlet of the cyclone was then examined. This smoke was found to provide adequate seeding for LDA measurements by So *et al*. (2000) and it is reconfirmed presently. The back-scatter mode LDA was used with a sampling rate of about 1200 samples per second. The number of samples collected at each measurement point was 50,000, with a typical validation rate of about 90%. The LDA system comes with necessary software for data processing and analysis to produce the time-averaged velocities, Reynolds stresses and power spectral density functions. Experimental uncertainties were estimated to be within 3% in averaged velocities and 10% in the root-mean-square (rms) values.

A Dantec standard PIV2100 system was deployed to measure flow velocities, V_θ and V_r, in the (r, θ)-plane at $z/R = 1$ (Fig. 4-1a). Four snapshots of the flow were taken each second. The flow was seeded by fog generated from Paraffin oil with a particle size of about 1μm in diameter, and illuminated by two New Wave standard pulsed laser sources, each having a maximum energy output of 120 mJ. Mosquito-repellant-generated smoke tended to deposit on the internal wall of the

cyclone, which had a negligible effect on LDA measurements but not on PIV measurements. An optical filter was used to allow only the green light (wavelength = 532 nm) generated by laser sources to pass through. Each laser pulse lasted for 10 ns. The time interval to capture two sequential images was about 50 μs. Digital particle images were taken using one CCD camera (HiSense type 13, gain × 4, double frames, 1280 × 1024 pixels), mounted with a wide-angle lens so that each image corresponded to an area of 112 mm × 89.6 mm, covering almost the entire flow field of interest. A Dantec FlowMap Processor (PIV2100) was used to synchronize image acquisition and illumination. The longitudinal and lateral image magnifications were identical, i.e., 0.0875 mm/pixel.

The PIV data analysis was conducted by software, FlowManager, provided by Dantec. The peak-finding algorithm was *Peak-height validation*, which validated or rejected individual vectors based on the values of the peak heights in the correlation data**,** where the raw vector displacement was measured. The cross correlation between the initial and final positions of the flow field, recorded on two consecutive images, was calculated using a cross-correlation algorithm, included in the software of the Dantec PIV system. In the processing of the (r, θ)-plane images, the interrogation area was 64 pixels × 64 pixels (≈ 5.6 mm × 5.6 mm) with 75% overlap in each direction. The overlap was used to minimize the occurrence of erroneous vectors. The ensuing in-plane velocity vector field consisted of 77 × 61 vectors (4697 vectors in total). Vectors outside the specified velocity range are most likely to be false vectors (outliers). *Velocity range validation* and *moving average validation* were applied to

remove outliers from raw velocity vectors. The rejected vectors were replaced by vectors estimated using the neighboring values. Subsequently, the *moving average filter* was used for reducing noise in the obtained vectors. In this investigation, about 51 outliers were substituted in a typical vector map, accounting for about 1% of the

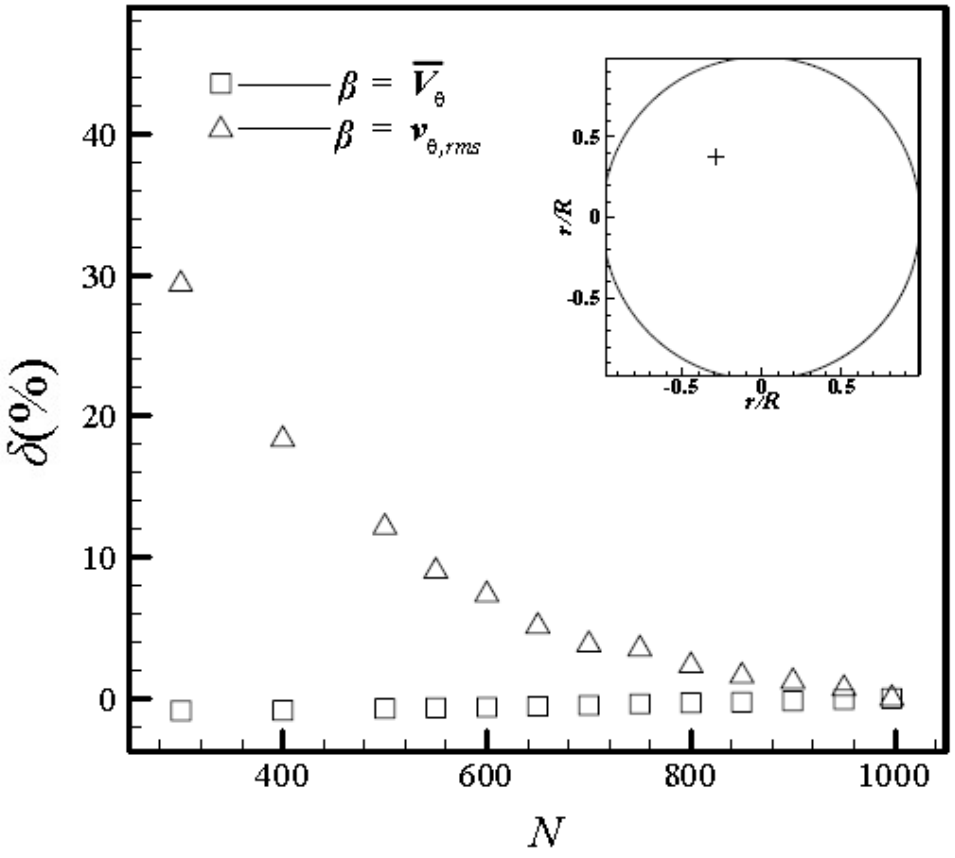

Fig. 4-2 Dependence of $\delta = \frac{\beta_N - \beta_{N-\Delta N}}{\beta_N} \times 100\%$, where β is $\overline{V_\theta}$ or $v_{\theta,rms}$, on the number N, of PIV images. Measurement location is at $r/R = 0.5$ and $\theta = 120^\circ$, as marked by symbol

total number of vectors generated. A total of 1000 flow snapshots were obtained. A convergence test was done based on velocity data obtained at $r/R = 0.5$, $\theta = 120^o$, as marked by symbol + in the insert of Fig. 4-2. As illustrated in the figure, $\delta = \frac{\beta_N - \beta_{N-\Delta N}}{\beta_N} \times 100\%$, where β denotes $\overline{V_\theta}$ or $v_{\theta,rms}$, indicates that experimental

uncertainty is less than 1% in the averaged velocity even before the snapshot number N reaches 400 and within 2% in the root mean square (rms) velocity. The axial vorticity component Ω_z of the same number as velocity vectors was approximately derived based on particle velocities, viz.

$$\Omega_z = \frac{1}{r}\frac{\partial r V_\theta}{\partial r} - \frac{1}{r}\frac{\partial V_r}{\partial \theta} \approx \frac{1}{r}\left(\frac{\Delta r V_\theta}{\Delta r} - \frac{\Delta V_r}{\Delta \theta}\right) .$$

Ω_z may be resolved into an averaged component $\overline{\Omega}_z$ and a fluctuating component ω_z, viz. $\Omega_z = \overline{\Omega}_z + \omega_z$.

4.3. Turbulent flow structure

Figure 4-3 presents the radial distributions of the normalized LDA-measured parameters $\overline{V}_\theta^*$ (= V_θ / V_{in}), $v_{\theta,rms}^*$ (= $v_{\theta,rms} / V_{in}$), $\overline{V}_z^*$ (= V_z / V_{in}), and $v_{z,rms}^*$ (= $v_{z,rms} / V_{in}$) at S = 2.4 and the ($r;\theta$) plane of z/R=1. For the convenience of discussion, we hereinafter designate the r/R value at θ = 0 or 0.5π to be positive and that at $\theta = \pi$ and 1.5π to be negative. The distributions are not perfectly symmetrical about the geometric centre r/R = 0 or the centre of the vortex core, as noted by Wong *et al*. (2007). This is not unexpected since the flow at the entry of the cyclone is asymmetrical (Fig 4-1a). Solero and Coghe (2002) measured the turbulent flow in a cyclone chamber at a swirl number of S = 2.39 and Re = 3.76×10^4 using LDA technique. Their measurements were in agreement quantitatively with the present data in $\overline{V}_\theta$, though only qualitatively in $\overline{V}_z$. Quantitative agreement was also observed in $v_{\theta,rms}$ and $v_{z,rms}$ in r/R = -0.86 ~ 0.70 but not in r/R = 0.70 ~ 0.86. The deviation

probably results from a difference in the cyclone inlet used in the two sets of experiments. Solero and Coghe used a helix type of inlet, whilst we used a tangential

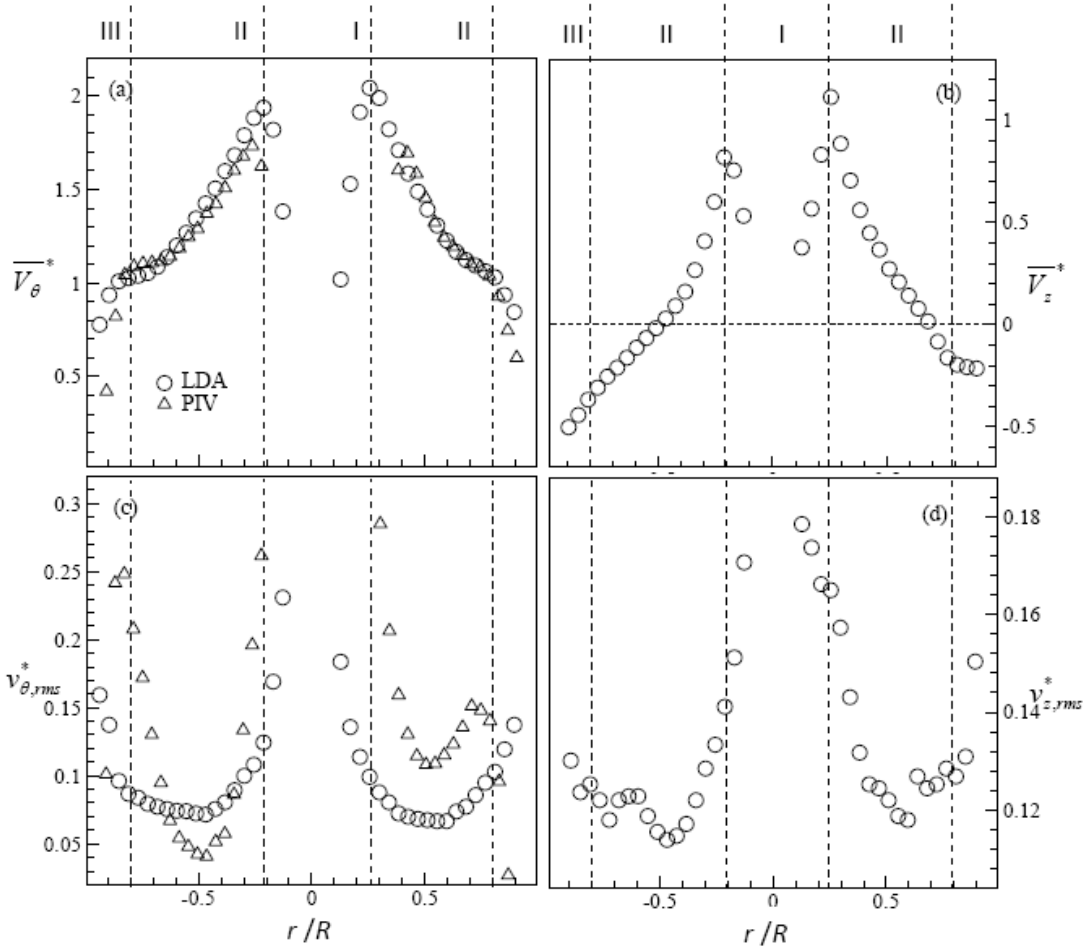

Fig. 4-3 The radial distributions of (a) the LDA-measured mean tangential velocity $\overline{V_\theta}^*$, (b) mean axial velocity $\overline{V_z}^*$, (c) rms tangential velocity $v^*_{\theta,rms}$, (d) rms axial velocity $v^*_{z,rms}$ S = 2.4, Re = 74000, z/R=1. Three distinct regions may be identified, viz. the vortex core region (I), the outer region (II), and the wall-affected region (III).

type of inlet. As a cross check, the PIV-measured $\overline{V}^*_\theta$ and $v^*_{\theta,rms}$ are included in the figure. In general, the $\overline{V}^*_\theta$ data (Fig 4-3a) from the two techniques collapses well. A qualitative agreement in $v^*_{\theta,rms}$ is also observed, though not quantitatively. This departure is ascribed to a difference in both the measurement technique, including different seeding particles, and the number of data (1000 vs 50,000). In view of its much larger quantity, the LDA data is considered to be more reliable than the PIV

data.

The flow may be divided into three regions, viz. the vortex core region or Region I, the outer region or Region II, and the wall-affected region or Region III, as marked on the top of figure 4-3a and b. In Region I, $\overline{V}_\theta^*$ rises rapidly and approximately linearly to its maximum with increasing *r/R*, that is, the core region rotates like a rigid body in terms of $\overline{V}_\theta^*$, as described by Hoffmann and Stein (2002). $\overline{V}_z^*$ also increases approximately linearly to its maximum with respect to *r/R* and is positive, i.e., upward. Moreover, both $v_{\theta,rms}^*$ and $v_{z,rms}^*$ are large in this region. It should be mentioned that the flow seeding concentration is rather low because of difficulty for seeding particles to get into this region under the centrifugal force effect, which is the major reason of a large scattering of measured velocities in this region than in other regions. As a result, the LDA data near the core center was not included. This point will be elaborated in more detail in Section 4-4. In Region II, $\overline{V}_\theta^*$ declines approximately linearly with increasing *r/R* and so does $\overline{V}_z^*$. $\overline{V}_z^*$ is predominantly positive. Both $v_{\theta,rms}^*$ and $v_{z,rms}^*$ are small in this region. Region III is downward flow, characterized by interactions between Region II and the near wall flow. $\overline{V}_\theta^*$ and $v_{\theta,rms}^*$ display the characteristics of the boundary layer, rapidly dropping and rising, respectively, as the wall is approached. $\overline{V}_z^*$ is entirely negative in sign (downward), and $v_{z,rms}^*$ appears rising.

In order to gain a better picture of the turbulent flow structure in the cyclone, the iso-contours of the PIV-measured $\overline{V}_\theta^*$, $\overline{V}_r^*$, $v_{\theta,rms}^*$, $v_{r,rms}^*$, $\overline{v_\theta v_r}^*$ and averaged velocity vectors in the (r, θ) plane of the cyclone chamber (z/R = 1) are examined, which are calculated based on 1000 snapshots of flow obtained at $Re = 7.4\times10^4$ and S

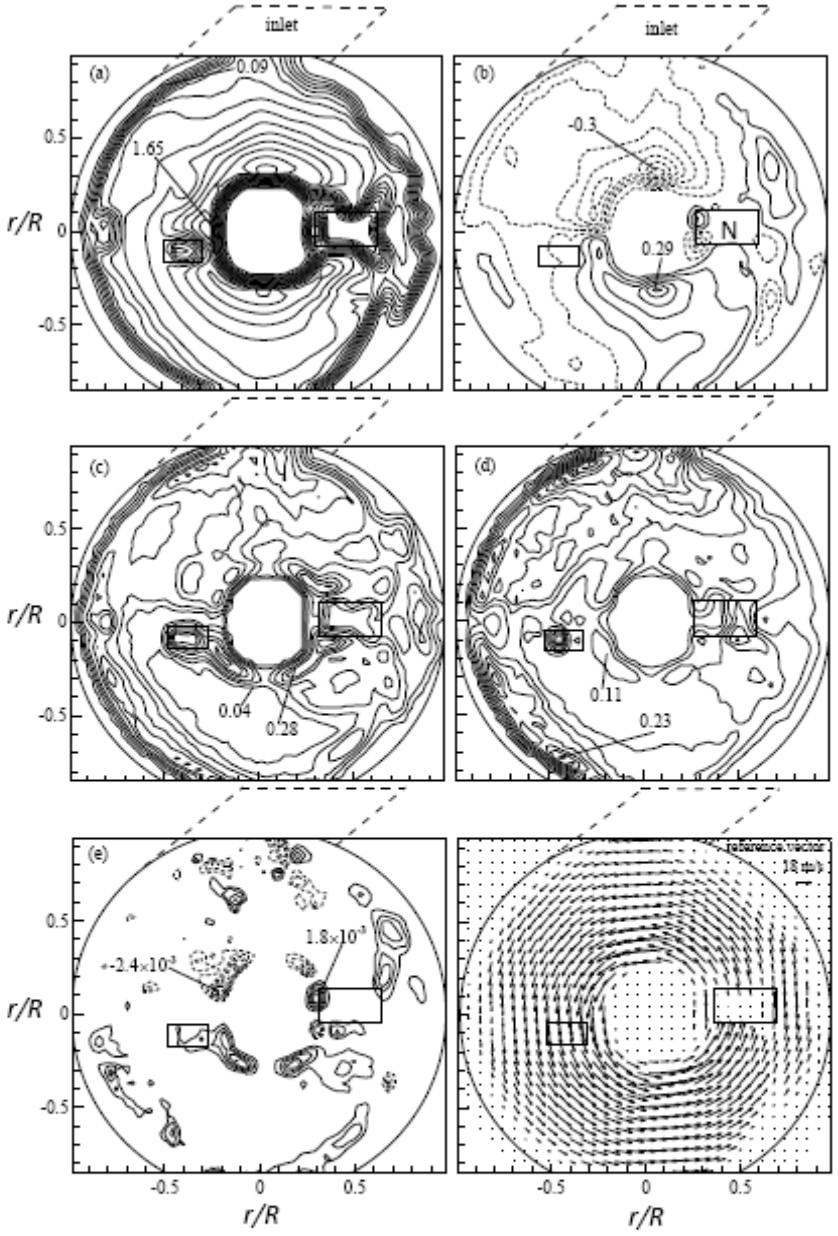

Fig. 4-4 Iso-contours of (a) mean tangential velocity $\overline{V_\theta}^*$ (contours interval $\Delta = 0.12$), (b) mean radial velocity $\overline{V_r}^*$ (0.039), (c) RMS tangential velocity $v^*_{\theta,rms}$ (0.035), (d) RMS radial velocity $v^*_{r,rms}$ (0.029), and (e) Reynolds shear stress $\overline{v_\theta v_r}^*$ in the (r, θ)-plane ($3.0\text{x}10^{-4}$). (f) Averaged velocity vectors. $Re = 7.4 \times 10^4$, $S = 2.4$, $z/R = 1$.

= 2.4. As in the LDA measurement, the centrifugal force could act to reduce the seeding particle concentration in the core region, resulting in a poor quality of data in this region. Therefore, the data near the core centre has been removed. Note that, as

the laser sheet shined across the measurement section, its reflection noise from the wall of the circle cyclone chamber was strongest about the directly opposite spot, resulting in a small area of funny shaped contours, denoted by N in figure 4- 4a. All the contours (Fig. 4-4) share the same characteristics and may be in general divided into three regions: (1) the central region of the highest concentration, (2) the near wall region of relatively high concentration and (3) the annular region between the central and the near wall regions, which is least concentrated. The three regions coincide with Regions I, II and III, respectively, as identified from the LDA data (Fig. 4-3). This division has not been reported before.

As shown in Fig. 4-4a, the $\overline{V}_{\theta}^{*}$-contours have the maximum value at $r/R \approx \pm 0.25$, where Regions I and II join. The spacing between the contours is small within the core region, indicating a large gradient of $\overline{V}_{\theta}^{*}$. Outside the core, the $\overline{V}_{\theta}^{*}$ gradient is smaller, though increasing again near the wall. The observations are internally consistent with the LDA measurement (Fig. 4-3a). The $\overline{V}_{r}^{*}$-contours (Fig. 4-4b) are largely of negative sign in the semicircular area starting from the inlet. The observation is reasonable. In this area, the centripetal movement of flow was produced, which changes the inflow mode from the tangential motion to the swirl, that is, with a motion towards the cyclone centre. In the other semicircular area, the flow was under the centrifugal force associated with the swirl motion, generating a significant presence of positive $\overline{V}_{r}^{*}$. $\overline{V}_{r}^{*}$ does not exceed 20% of $\overline{V}_{\theta}^{*}$ in magnitude, perhaps partially due to its random occurrence of opposite signs. The maximum magnitude of $\overline{V}_{r}^{*}$, as that of $\overline{V}_{\theta}^{*}$, occurs in the area joining Regions I and II.

The level of $v^*_{\theta,rms}$ as shown in Fig. 4-4c is large within $|r/R|$ < 0.3 and near the wall at $|r/R|$ > 0.7. In the two regions, the spacing between the contours is very small, implying a rapid change in $v^*_{\theta,rms}$ with respect to *r/R,* in agreement with the LDA measurement as shown in Fig. 4-3c. The $v^*_{r,rms}$ as shown in Fig. 4-4d is in general very small; its maximum is less than one half of that of $v^*_{\theta,rms}$ and occurs at $|r/R| < 0.1$. The Reynolds shear stress $\overline{v_\theta v_r}^*$ as shown in Fig. 4-4e is by far smaller in magnitude than $v^*_{r,rms}$ and $v^*_{\theta,rms}$, perhaps only appreciable in the core region, where the iso-contours of $\overline{v_\theta v_r}^*$ bear topological similarity to that of $\overline{V}^*_r$. The averaged velocity vectors calculated from the velocity data of 1000 flow snapshots in the measurement plane are shown in Fig. 4-4f. It shows that the flow field is not entirely axisymmetrical about the axis of the cyclone.

The iso-contours of the averaged magnitude, $|\overline{\Omega_z}^*|$ (=$|\overline{\Omega_z} 2R/U_{in}|$) is shown in

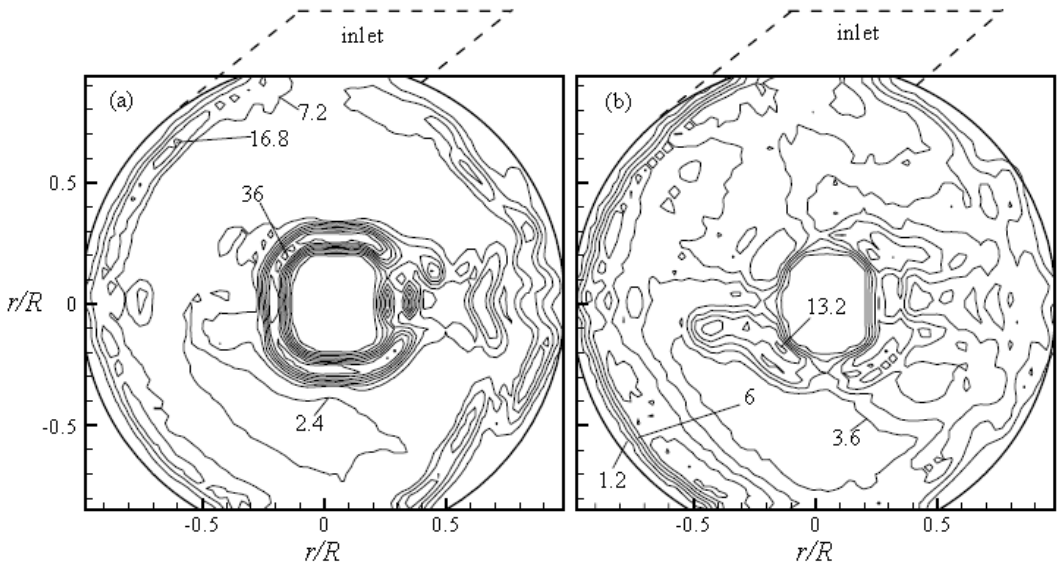

Fig. 4-5 Iso-contours of (a) the magnitude of averaged vorticity $|\overline{\Omega_z}(2R/U_{in})|$ (contour interval Δ = 4.8) and (b) RMS vorticity $\omega^*_{z,rms}$ in the (r, θ) plane (Δ = 2.4), Re = 7.4 x 10^4, S = 2.4, z/R = 1.

Fig. 4-5a, and root mean square value, $\omega^*_{z,rms}$ as shown in Fig. 4-5b, of the axial

vorticity component appear qualitatively similar to those of $v^*_{r,rms}$ or $v^*_{\theta,rms}$, displaying three distinct regions, the highly concentrated central region, the relatively concentrated near-wall region and the annular region of very low contour levels, which coincide well with the three regions identified from velocity data in Figs. 4-3 and 4-4.

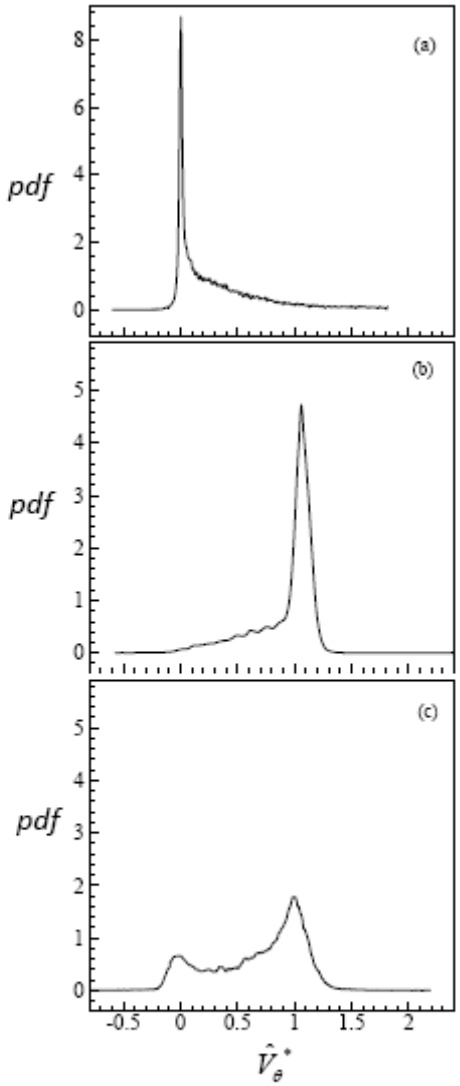

Fig. 4-6 The probability density function, p, of the instantaneous circumferentially averaged tangential velocity $\hat{V}_\theta^*$: (a) $r/R = 0.2$, (b) 0.65, (c) 0.85. $S = 2.4$, $Re = 74000$.

The probability density function of velocities may provide important information

on the turbulent flow structure. As indicated in Figs. 4-3 and 4-4, the velocity field is not perfectly axis-symmetrical about the cyclone centre. Thus, we define a circumferentially averaged velocity component by

$$\hat{\alpha}(r) = \frac{1}{2\pi}\int_0^{2\pi} \alpha(r,\theta)d\theta \approx \frac{1}{2\pi}\sum_{\theta_i=0}^{2\pi} \alpha(r,\theta_i)\Delta\theta_i ,$$

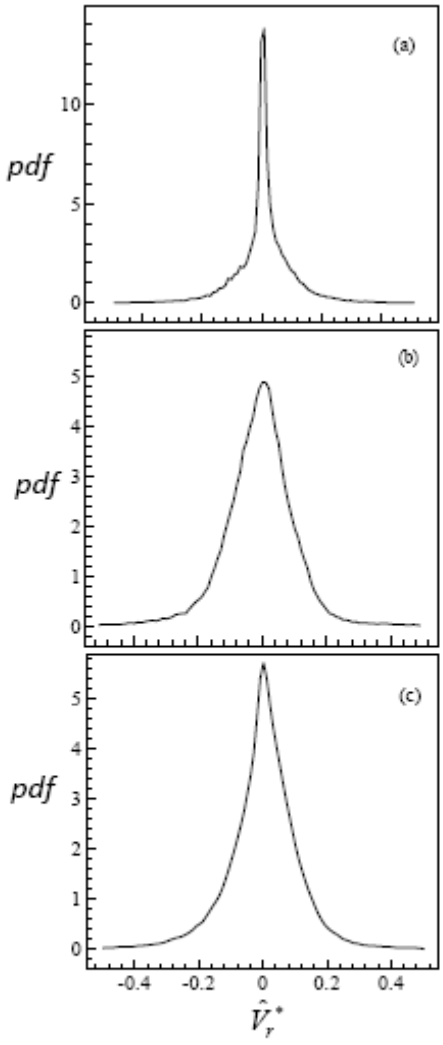

Fig. 4-7 The probability density function, p, of the instantaneous circumferentially averaged radial velocity $\hat{V}_r^*$. $S = 2.4$, $Re = 7.4 \times 10^4$, (a) $r/R = 0.2$, (b) 0.65, (c) 0.85.

where α denotes V_θ or V_r. The probability density function, $p(\hat{\alpha})$, of $\hat{\alpha}$ was calculated from the velocity data of 1000 flow snapshots. Typical $p(\hat{V}_\theta^*)$ and $p(\hat{V}_r^*)$

plots in each of the three regions are shown in Figs. 4-6 and 4-7, respectively; the chosen r/R = 0.2, 0.65 and 0.85 correspond to Region I, II and III, respectively. Evidently, each $p(\hat{V}_\theta^*)$ is distinct from others. In the core region (I), $p(\hat{V}_\theta^*)$ (Fig. 4-6a) is characterized by a sharp spike about $\hat{V}_\theta^* = 0$. The $p(\hat{V}_\theta^*)$ is asymmetrical about $\hat{V}_\theta^* = 0$: significant at $\hat{V}_\theta^* > 0$ and appreciable up to only $\hat{V}_\theta^* \approx 1$. The observation is consistent with the perception of the flow in the core region. In the outer region (II), a pronounced peak occurs at $\hat{V}_\theta^* > 1$, and $p(\hat{V}_\theta^*)$ is small for $\hat{V}_\theta^* < 1$, which matches with the small value of $v_{\theta,rms}^*$ in Fig. 4-3c. In the wall-affected

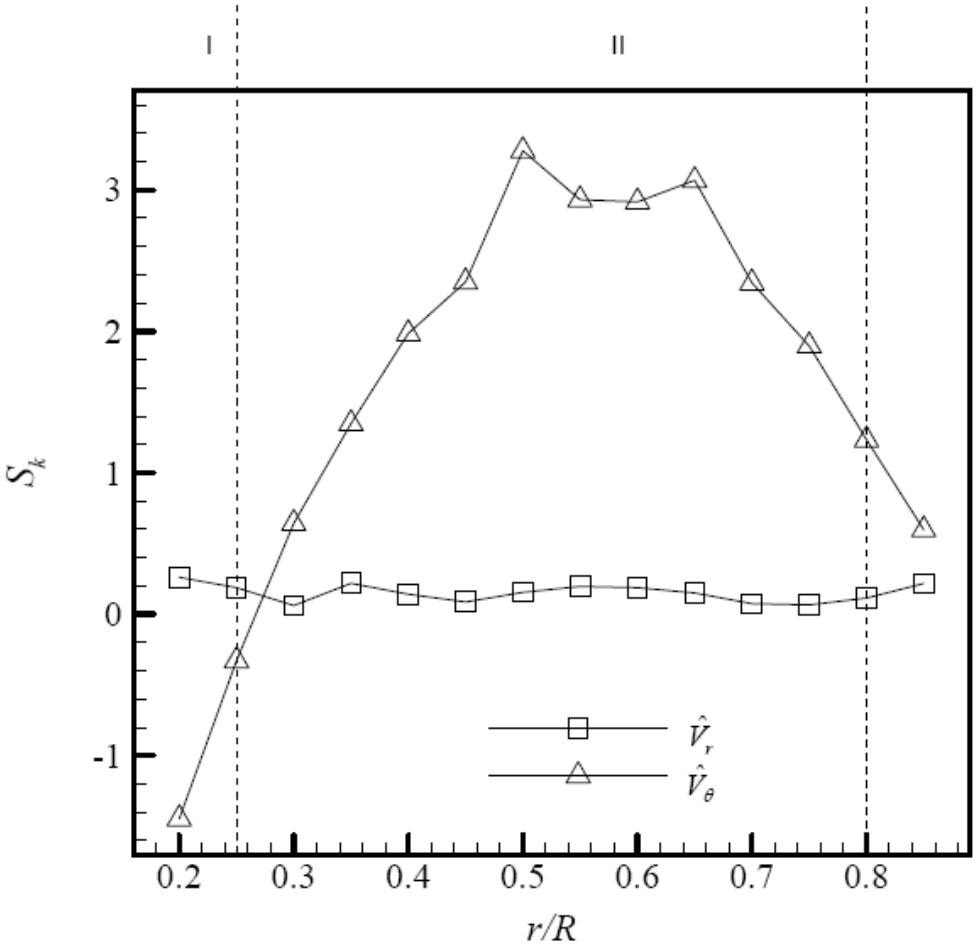

Fig. 4-8 Dependence on r/R of skewness S_k of the instantaneous circumferentially averaged velocities $\hat{V}_\theta$ and $\hat{V}_r$. $S = 2.4$, $Re = 7.4 \times 10^4$, $z/R = 1$.

region (III), two peaks are discernible, though with much less difference in magnitude than in Region II. Furthermore, $p(\hat{V}_\theta^*)$ is significant all the way from the peak at $\hat{V}_\theta^*$ = 0 to the other peak at $\hat{V}_\theta^*$ = 1, revealing an increased $v_{\theta,rms}^*$, as shown in Fig. 4-3c.

The $p(\hat{V}_r^*)$ in Fig. 4-7 is rather different from $p(\hat{V}_\theta^*)$, regardless of regions. Nevertheless, the difference is discernible between the three regions. In the core region, $p(\hat{V}_r^*)$ is characterized by a very sharp peak and is approximately symmetrical about $\hat{V}_r^*$ = 0. In the outer region, the distribution of $p(\hat{V}_r^*)$ appears to be normal. In the wall-affected region, $p(\hat{V}_r^*)$ displays a sharp peak at $\hat{V}_r^*$ = 0, though with a broader distribution than in the core region. Note that in the core region the range of the magnitude of nonzero $\hat{V}_r^*$ is about 0 ~ 0.2 while that of $\hat{V}_\theta^*$ (Fig. 4-6a) is about 0 ~ 1, suggesting that the radial motion could not be entirely neglected in this region. This observation shows the deviation from the assumption of rigid body fluid rotation in the core region which is often made in other fluid flow models (Hoffmann and Stein 2002). Appreciable radial motion is also evident in other two regions.

The skewness (S_k) and flatness (F) of circumferentially averaged velocity component $\hat{\alpha}$ are defined by

$$S_k = \frac{\overline{(\hat{\alpha} - \overline{\hat{\alpha}})^3}}{\sqrt{\overline{(\hat{\alpha} - \overline{\hat{\alpha}})^2}^3}} \quad ,$$

and

$$F = \frac{\overline{(\hat{\alpha} - \overline{\hat{\alpha}})^4}}{\sqrt{\overline{(\hat{\alpha} - \overline{\hat{\alpha}})^2}^4}} \quad ,$$

respectively. Figures 4-8 and 4-9 present S_k and F of $\hat{V}_\theta$ and $\hat{V}_r$, respectively, at a number of radii from r/R = 0.2 to 0.85. It is evident that $\hat{V}_\theta$ is negatively and

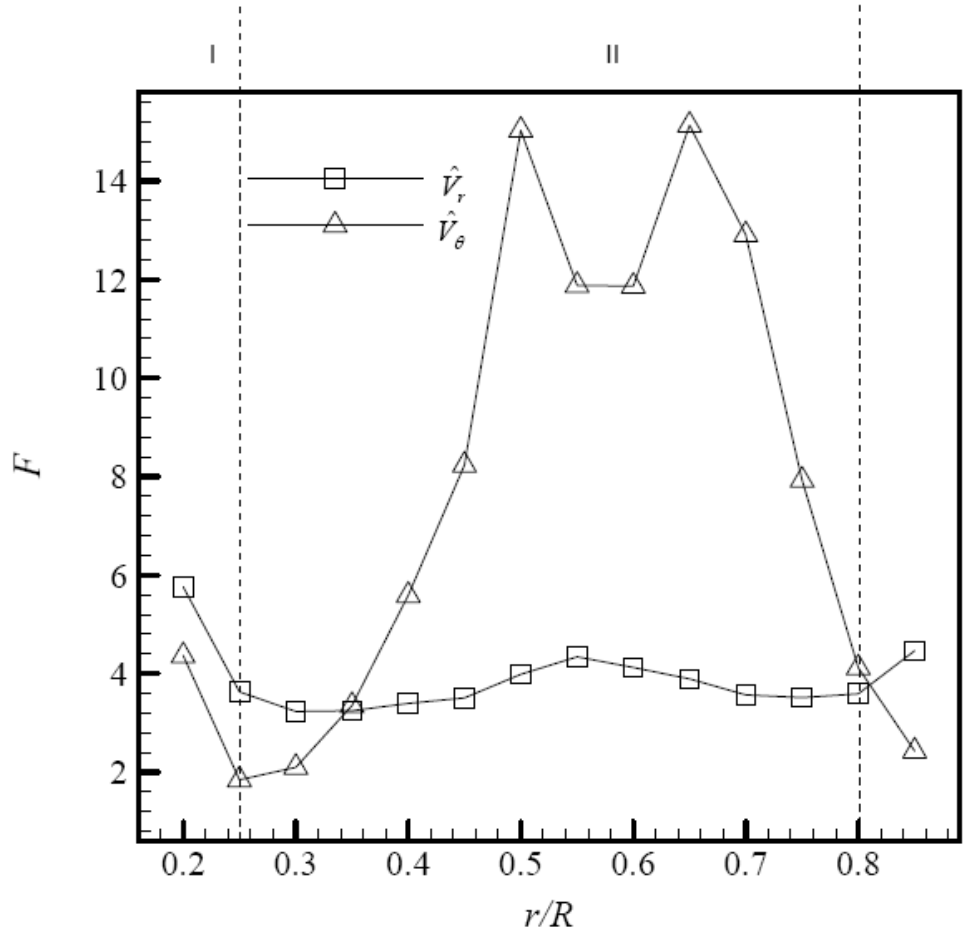

Fig.4- 9 Dependence on r/R of flatness F of the instantaneous circumferentially averaged velocities $\hat{V}_\theta$ and $\hat{V}_r$. $S = 2.4$, $Re = 7.4 \times 10^4$, $z/R = 1$.

positively skewed in the core and outer regions, respectively. $S_k(\hat{V}_\theta)$ remains positive but approaches zero with increasing r/R in the wall-affected region. On the other hand, $S_k(\hat{V}_r)$ varies little across the flow and is only slightly positively skewed. $F(\hat{V}_\theta)$ is small in the core and wall affected regions but may become large in the outer region.

4.4. Flow dependence on swirl number

4.4.1. Mean and fluctuating velocities

The dependence of the flow on the swirl number is investigated by examining the flow in the (r, θ)-plane. Figure 4-10 presents the radial distributions of LDA-measured $\overline{V_\theta}^*$ and $v^*_{\theta,rms}$ along the X-X axis (Fig. 1c) at four different swirl numbers, i.e., S = 2.4, 3.0, 4.3 and 5.3. The data is shown only in the outer region because flow could not be always well seeded, that is, the concentration of smoke particles is not always sufficient, about the center and near the wall for the four swirl numbers examined,

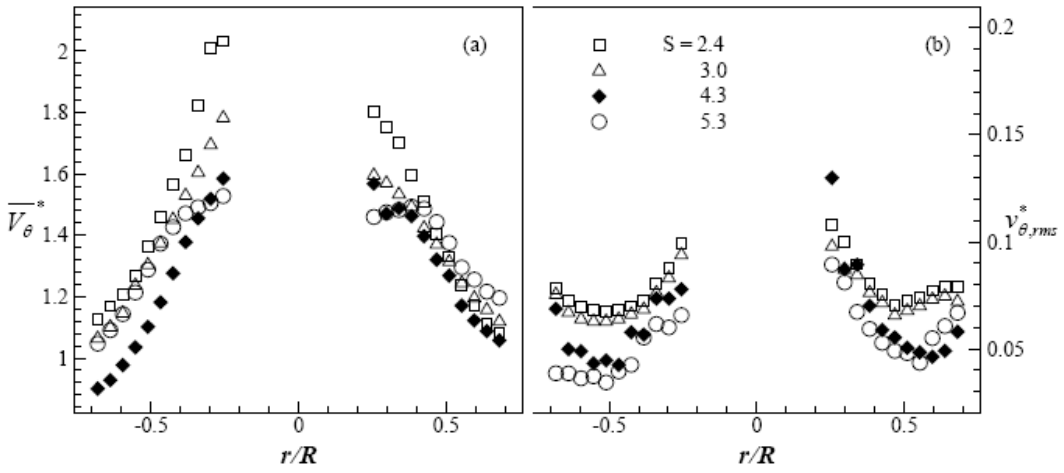

F1g. 4-10 The radial distribution of (a) the LDA-measured mean tangential velocity $\overline{V_\theta}^*$, and (b) rms tangential velocity $v^*_{\theta,rms}$ at different swirl number. Re = 7.4 x 10^4, z/R = 1.

which caused a low data sampling rate and hence a poor quality of data in the two regions. As the swirl number increases, $\overline{V_\theta}^*$ displays appreciable variation, becoming less steep with respect to r/R, across the region. Hoekstra *et al*. (1999) investigated the turbulent swirl flow in a gas cyclone using the LDA technique and numerical simulation at $Re = 2.5 \times 10^4$ and S = 1.8, 2.2 and 3.1. Their setup had a vortex stabilizer at the bottom of the cylinder chamber of the cyclone. Their measured $\overline{V_\theta}^*$ profiles showed a similar trend to the present data, that is, the gradients of $\overline{V_\theta}^*$ along the radial direction increased as the swirl number decreased.

The $v^*_{\theta,rms}$ (Fig. 4-10b) reduced as the swirl number increased. To quantify this trend, we define the following averaged turbulence intensity

$$T_{v_\theta} = \frac{1}{2}\left(\frac{1}{N_1}\sum_{i=1}^{i=N_1} \frac{v_{\theta,rms}(r_i/R)}{U_{in}} + \frac{1}{N_2}\sum_{i=1}^{i=N_2} \frac{v_{\theta,rms}(r_i/R)}{U_{in}} \right),$$

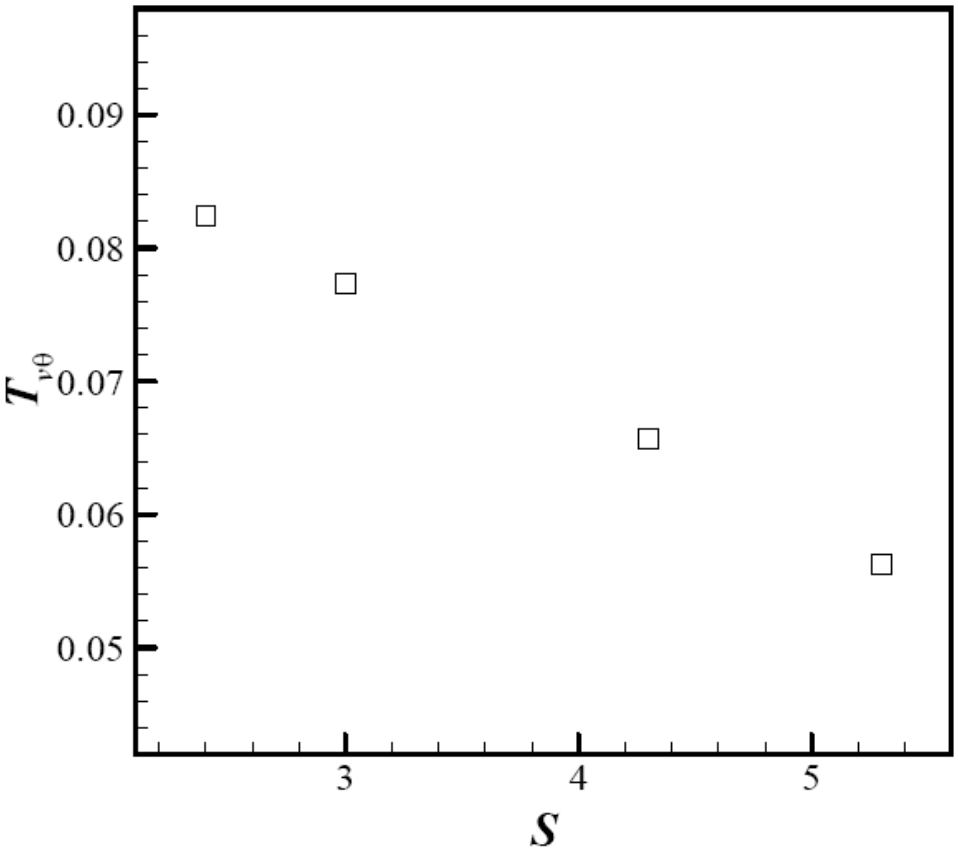

Fig. 4-11 Dependence of $T_{v_\theta} = \frac{1}{2}\left(\frac{1}{N_1}\sum_{i=1}^{i=N_1} \frac{v_{\theta,rms}(r_i/R)}{U_{in}} + \frac{1}{N_2}\sum_{i=1}^{i=N_2} \frac{v_{\theta,rms}(r_i/R)}{U_{in}} \right)$ on S, where r_1/R (= 0.25) $\le r_i/R \le$ r_{N_1}/R (= 0.68) or r_1/R (= -0.68) $\le r_i/R \le$ r_{N_2}/R (= -0.25) corresponds to the outer region. Re = 7.4 x 10^4.

where r_i/R falls in the outer region, i.e., r_1/R (= 0.25) $\le r_i/R \le$ r_{N_1}/R (= 0.68) or r_1/R (= -0.68) $\le r_i/R \le$ r_{N_2}/R (= -0.25). N_1 is the number of measured velocity in the range of $0.25 \le r/R \le 0.68$, and N_2 is the number of measured velocity in the range of $-0.25 \le r/R \le -0.68$. Referring to Figure 4-10, N_1 and N_2 equal to 11.

Figure 4-11 shows the dependence of T_{v_θ} on *S*. T_{v_θ} drops almost linearly with increasing *S*. The observation may not be unexpected in view of the reduced radial gradient of $\overline{V_\theta}^*$, which implies a smaller strength of large-scale coherent structures resulting from the shear layer instability, for a higher *S* (Fig. 4-10a). This result also conforms to Hoekstra *et al*.'s (1999) numerical prediction of fluctuating velocities based on a Reynolds stress transport model, where the fluctuating velocities decreased as the swirl number increased. The result indicates that the mixing performance in the cyclone flow will be weakened as the swirl number increases. It should be noted that the measured $v^*_{\theta,rms}$ by Hoekstra *et al*. was different from ours. For example, their $v^*_{\theta,rms}$ at $S = 2.2$ decreased from the maximum at $r/R = 0$ to about 0.12 at $r/R \approx 0.25$ and then changed little from $r/R \approx 0.25$ to 0.95, but the present $v^*_{\theta,rms}$ at $S = 2.4$ drops from the maximum at $r/R = 0$ to about 0.07 at $r/R \approx 0.5$ and then rises towards the wall. This deviation is expected since a vortex stabilizer was installed in their cyclone but not in the present one.

4.4.2. Strouhal number

Figure 4-12 presents the power spectral density function, E_{v_θ}, of the LDA-measured v_θ at $r/R = 0.26 \sim 0.90$ along the axis X-X (Fig. 4-1c) at the four different swirl numbers. The power spectrum in the core and wall-affected regions was not shown for the same reason as mentioned in 4.1. A number of observations can be made. Firstly, E_{v_θ} displays pronounced twin peaks in $0.26 \le r/R \le 0.43$, one at $St_1 \equiv f_1(2R)/U_{in}$ and the other at a higher frequency $St_2 \equiv f_2(2R)/U_{in}$, where f_1 and f_2 are the frequencies corresponding to the two peaks, respectively. Wong *et al*. (2007) made the same observation for $Re = 3.7 \sim 7.4 \times 10^4$, and ascribed f_1 and f_2 to the shear layer

instabilities associated with the downward and upward precessions of the flow, respectively. The two precessions are oppositely sensed. The downward

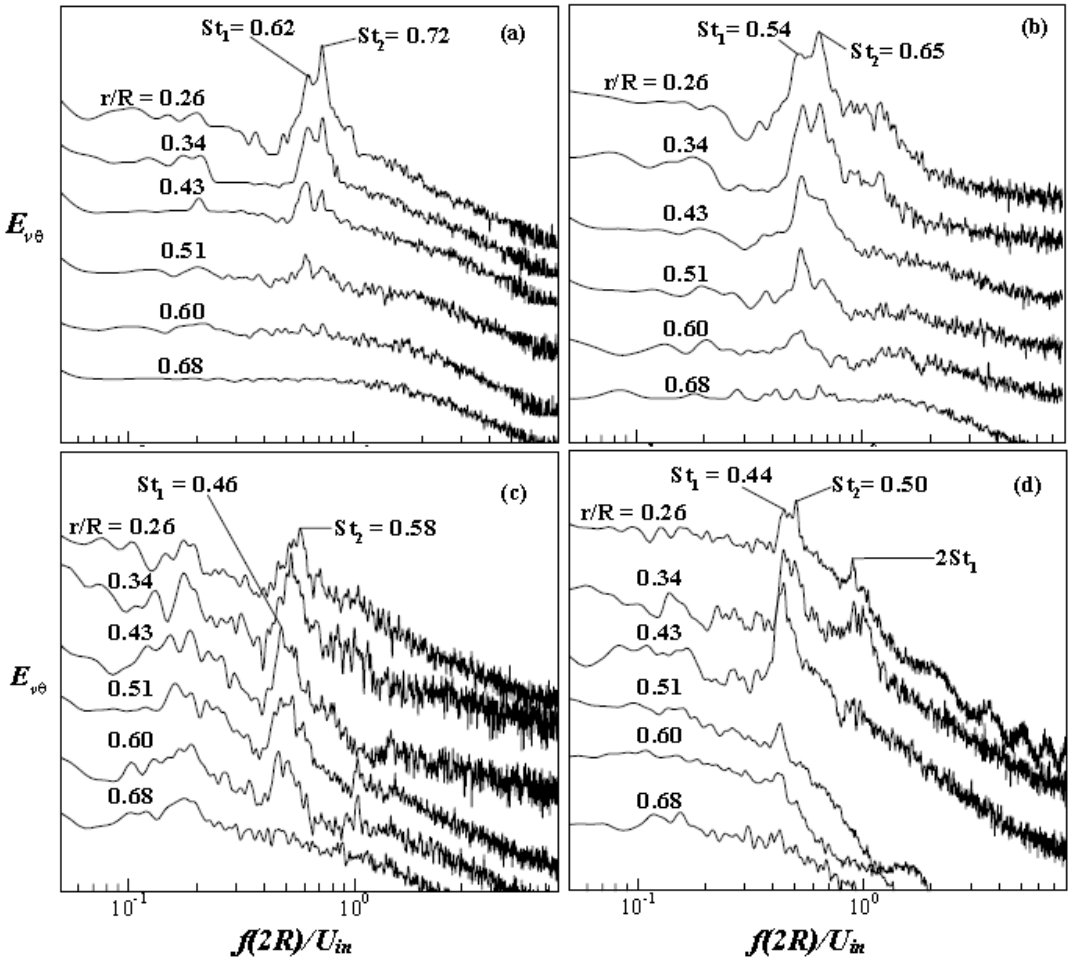

Fig. 4-12 Power spectral density functions E_{v_θ} of v_θ, measured along X-X (Fig. 1c) in the (r, θ) plane (z/R=1), at various r/R using LDA. (a) S = 2.4, (b) 3.0, (c) 4.3, (d) 5.3. Re = 7.4x10^4.

precession occurs in the outer and wall-affected regions and the upward in the outer and core regions as shown in Fig. 4-3b. The range of r/R = 0.26 ~ 0.43 is in the upward flow part of the outer region. This part joins the core region and the downward flow that occurs in the outer and wall-affected regions, and naturally both instabilities can be seen in E_{v_θ}. Secondly, the peak at St_2 is less pronounced at r/R = 0.43 and almost invisible at r/R = 0.68, irrespective of the S values. The observation

complies with the perception that the influence of the shear layer instability associated with the upward precession motion in the core region diminishes with increasing *r/R* in the outer region. Meanwhile, the peak at St_1 remains evident in the outer region,

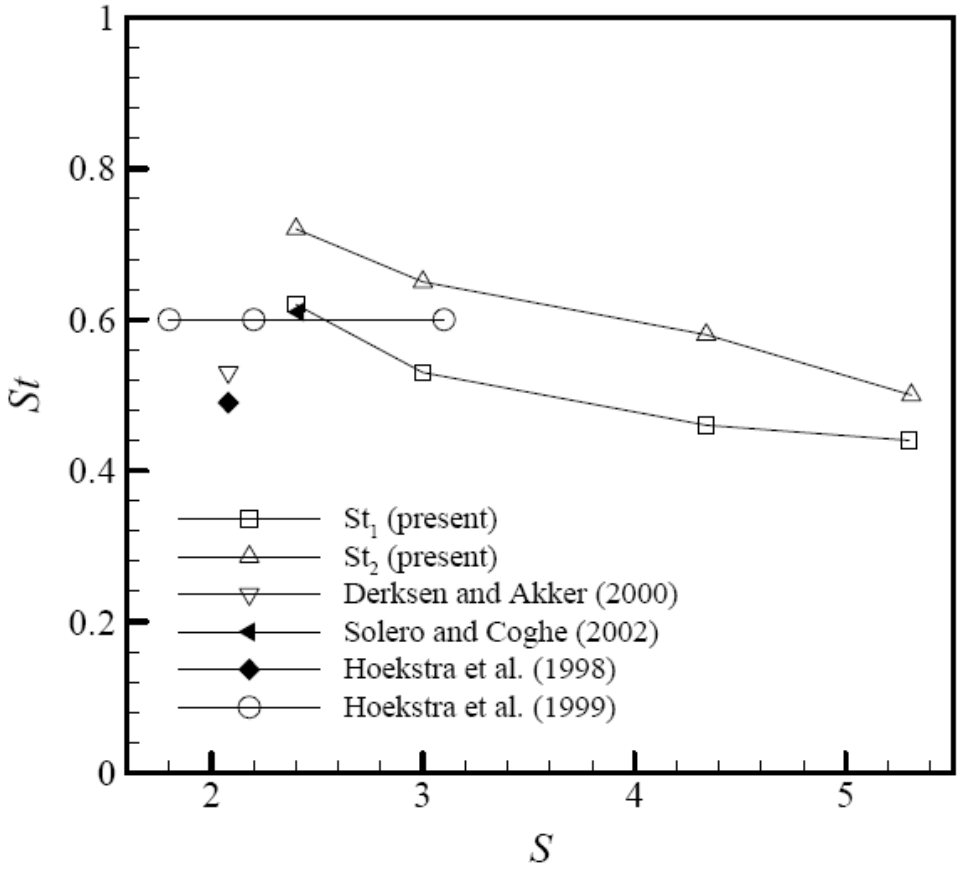

Fig. 4-13 Dependence of Strouhal numbers (*St*) on the swirl number (*S*) in the cyclone flow.

though weakened when approaching the wall-affected region. The interaction with the wall or the wall-affected region apparently impairs the shear layer instability associated with the downward precession motion. Finally, both St_1 and St_2 decrease with increasing *S* as shown in Fig. 4-13. Both St_1 and St_2 shows a near linear relationship with the swirl number *S*. Data reported by other investigators are also given in the figure for comparison. Solero and Coghe's (2002) LDA measurement at *S* = 2.39 (*Re* = 3.76 x 10^4 and 1.25 x 10^5) agrees well with the present St_1 at *S* = 2.4.

Hoekstra *et al*.'s (1998) measurement using LDA and Derksen and Akker's (2000) simulation result deviate considerably from either St_1 or St_2. The cyclone was mounted with a vortex stabilizer for the former but built without the conical section for the latter. Hoekstra *et al*.'s (1999) *St* data appears independent of *S*. Their cyclone, built without the conical section, was installed with a vortex stabilizer at the base of the cylindrical body to create a sudden reduction in the cross-sectional area. The flow field would be very different from that of a standard cyclone. The difference in the cyclone will naturally lead to different observations. The present observation is believed to be reasonable. As shown in Fig. 4-10, the radial gradient of $\overline{V_\theta}^*$ decreases for a higher *S,* and the smaller gradient of the velocity would correspond to a thicker shear layer for the same velocity differentiation. The shear layer thickness and the characteristic frequency of large-scale coherent structures are inversely related (Wang and Zhou 2005). As a result, a lower frequency of coherent structures occurs for a higher *S*.

4.5. Conclusions

The turbulent flow structure inside a laboratory-scale cyclone has been studied at $Re = 7.4 \times 10^4$ based on the LDA- and PIV-measured three velocity components. The swirl number effect on the flow has also been investigated for $S = 2.4 \sim 5.3$. The work leads to the following conclusions.

1 Three distinct flow regions are identified in the cyclone flow, i.e., the core region, the outer region and the wall-affected region. The core region extends

from the centre to $r/R \approx 0.25$. This region is characterized by a high concentration of the axial vorticity and large fluctuating velocities $v^*_{\theta,rms}$ and $v^*_{z,rms}$. The averaged tangential velocity $\overline{V_\theta}^*$ rises rapidly to the maximum and approximately linearly with increasing *r/R*. So does the averaged axial velocity $\overline{V_z}^*$, though less rapidly. The outer region occurs from $r/R \approx 0.25$ to 0.70. In this region, both $\overline{V_\theta}$ and $\overline{V_z}^*$ decrease, albeit with a much smaller velocity gradient. Accordingly, the vorticity concentration is very low. So do $v^*_{\theta,rms}$ and $v^*_{z,rms}$. Beyond $r/R \approx 0.7$, the flow is appreciably affected by the presence of the wall; the vorticity concentration, $v^*_{\theta,rms}$ and $v^*_{z,rms}$ all rise, compared with the outer region, though remaining considerably below their counterparts in the core region. The circumferential and radial fluctuating velocities further exhibit distinct distributions in the probability density function, skewness and flatness from one region to another.

2 An increasing swirl number *S* causes a reduction in the tangential velocity gradient in the outer and core regions. As a result, the two Strouhal numbers, associated with the core and outer regions (Wong *et al*. 2007), respectively, decrease for a higher *S*. The reduced velocity gradient also results in a decrease in $v^*_{\theta,rms}$, implying impaired mixing in the cyclone with increasing *S*. Hoekstra *et al*. (1999) also noted that an increasing *S* was associated with a reduced tangential velocity gradient. However, their *St* appeared independent of *S,* in distinct contrast with the present result. The distinct observations lie in the fact that, whilst a standard cyclone is presently involved, their cyclone was

installed with a vortex stabilizer at the base of the cylindrical body, which created a sudden reduction in the cross-sectional area.

3 The radial motion could not be completely neglected in the core region, pointing to a departure from the rigid body rotation. In all the three regions, the Reynolds shear stress $\overline{v_\theta v_r}^*$ is by far smaller in magnitude than $v^*_{r,rms}$ or $v^*_{\theta,rms}$.

The experimental results reported in this article reveal a clearer picture of the turbulent flow structure and the dependence of flow velocities on the swirl number in the swirl flow within a cylinder-on-cone cyclone. It is hoped that these results will help in the improvement of the theoretical model of cyclone separator for more accurate prediction of the separation efficiency in future research.

CHAPTER 5

SUMMARY AND CONCLUSIONS

The thesis reports the major findings of investigations on two different turbulent flows, i.e., flow around an Ahmed vehicle model and that within a cylinder-on-cone cyclone. The details are summarized in two subsections.

5.1. Turbulent near wake of an Ahmed vehicle model

The detailed measurements of the 3-D near wake of the Ahmed model at Re_H = 5.26×10^4 have led to significant findings in three aspects. One aspect is the proposition of a modified flow structure model for each of the two distinct flow regimes examined, as presented in Fig 2-23.

In the regime of $\alpha < 30°$, six modifications are made, compared with the classical model shown in Fig 2-1a. (1) Shear layer developed over the top of the vehicle model flows partially along the slant under the effect of the C-pillar vortex and detaches partially from the body, as suggested by the distributions of the Reynolds stresses (Figs 2-16a, 2-18a and 2-19a). (2) While part of the shear layer separated from the slant is drawn into the recirculation bubble "A", the other part forms a quasi-periodical wavy spanwise roll flowing over "A", as is suggested by instantaneous Ω_y-contours (Fig 2-14a). The spectra of both fluctuating pressure and velocity signals measured near the upper edge of the vertical base by Vino *et al*.'s (2005) displayed a pronounced peak at a dimensionless frequency of 0.11, providing

experimental evidence for quasi-periodical flow separation from the upper edge of the base. The projection of this spanwise roll results in alternately signed vorticity concentrations in the y-z plane (Figs 2-6a and 2-7a) and in the *x*-*y* plane (Figs 2-20a and 2-21a). (3) Separated from the lower edge of the base, the gap flow between the model underside and wall is partially drawn into the recirculation bubble "B" and partially form a spanwise roll, separated quasi-periodically, again based on Vino *et al*.'s (2005) data. This roll is wrapped by longitudinal structures, as is supported by the instantaneous longitudinal vorticity contours (Fig 2-7a). Its signature in the *x*-*y* plane is also discernible by the alternately signed transverse vorticity concentrations in Fig 2-20a. (4) Side vortex "D" is added, which is generated by the shear layer developed over the side surface. This vortex starts breaking down at $x^* \approx 1.0$ as a result of interaction and merger with the C-pillar vortex. (5) The previously observed lower vortex (Krajnovic *et al.* 2005; Strachan *et al*. 2007) is added, which is generated by the pressure difference between flow inside the gap and that outside in a manner similar to how the C-pillar vortices are generated. (6) One pair of gap vortices are included, which are generated by struts between the model underside and wall.

In the regime of $\alpha > 30°$, modifications (3) through (6) at $\alpha < 30°$ apply. Three changes are noted, as per the case of $\alpha < 30°$. Firstly, the shear layer developed over the top of the vehicle now separates near the upper edge of the slant (Figs 2-13c, 2-14c, 2-15c, 2-17c and 2-19c) and is imbedded with alternately signed longitudinal vortices, as evidenced in Figs 2-6c and 2-7c. Secondly, the C-pillar vortex is greatly weakened, as shown in Figs 2-6c and 2-7c. Thirdly, the recirculation bubbles "E" over

the slant and “A” behind the base merge into one (Figs 2-13c, 2-14c, 2-15c, 2-17c and 2-19c).

The second aspect is the documentation of the effect of the clearance between the model underside and wall. It has been found that this clearance has a pronounced effect on the near wake of the vehicle model. Firstly, both bubbles “A” and “B” are altered, including the disappearance of the bubble “B”, at g* = 0 (Figs 2-13b, 2-13d, 2-14b, 2-14d and 2-19). But this does not necessarily mean the total recirculation bubble may shrink in size. As a matter of fact, the bubble size grows at $\alpha = 35°$, as shown in Fig 2-15c-d. Secondly, the absence of the clearance changes the strengths of the C-pillar vortex “C” and side vortex “D” (Fig 2-6).

The third aspect is to obtain the mean velocity and the second moments of fluctuating velocities in three orthogonal planes for different configurations, i.e., g* = 0.174 and 0 and $\alpha = 25°$ and 35°, which may be used for the validation of numerical models in the future.

5.2. Turbulent flow structure in a cylinder-on-cone cyclone

The important findings from the investigation on the turbulent flow within a cylinder-on-cone cyclone are summarized below:

Three distinct flow regions are identified in the cyclone flow, i.e., the core region, the outer region and the wall-affected region. The core region extends from the centre to $r/R \approx 0.25$. This region is characterized by a high concentration of the axial vorticity and large fluctuating velocities $v^*_{\theta,rms}$ and $v^*_{z,rms}$. The averaged tangential

velocity $\overline{V_\theta}^*$ rises rapidly to the maximum and approximately linearly with increasing *r/R*. So does the averaged axial velocity $\overline{V_z}^*$, though less rapidly. The outer region occurs from *r/R* ≈ 0.25 to 0.70. In this region, both $\overline{V_\theta}$ and $\overline{V_z}^*$ decrease, albeit with a much smaller velocity gradient. Accordingly, the vorticity concentration is very low. So do $v^*_{\theta,rms}$ and $v^*_{z,rms}$. Beyond *r/R* ≈ 0.7, the flow is appreciably affected by the presence of the wall; the vorticity concentration, $v^*_{\theta,rms}$ and $v^*_{z,rms}$ all rise, compared with the outer region, though remaining considerably below their counterparts in the core region. The circumferential and radial fluctuating velocities further exhibit distinct distributions in the probability density function, skewness and flatness from one region to another.

Two dominant frequencies, St_1 and St_2, are observed based on the power spectral density functions of the tangential and axial fluctuating velocities. The lower frequency St_1 is observed in both of the outer and core regions of the flow. This frequency is ascribed to the downward precession of the flow, within the cyclone, as a whole. To our knowledge, this frequency has been observed for the first time in the flow of a cylinder-on-cone cyclone. The higher frequency St_2 occurs in the core region as a result of the upward precession of the vortex core, as previously reported. The two precession motions are opposite in the sense of rotation. The two fluid motions, one spiral down and the other spiral up (Figure 3-3), are unlikely to have a 'clear-cut' border between them; there should be a transition region where both motions could be present. Indeed, the twin-peak distribution in E_{v_θ} (Figures 3-5 and 3-7) have been observed over r/R ≈ 0.26 ~ 0.43 in the upward flow region. However, the proposed

explanation has yet to be confirmed by more experimental or numerical data. It has been well known that large-scale vortical structures may result from shear layer instabilities (Zhou & Antonia, 1995, Wang & Zhou 2005, Wang *et al.* 2005). Naturally, the shear layer due to the occurrence of the spiral-up motion and spiral-down motion could lead to the formation of vortical structures. Nevertheless, more experimental evidence is required to confirm the present proposition.

An increasing swirl number *S* causes a reduction in the tangential velocity gradient in the outer and core regions. As a result, the two Strouhal numbers, associated with the core and outer regions, respectively, decrease for a higher *S.* The reduced velocity gradient also results in a decrease in $v^*_{\theta,rms}$, implying impaired mixing in the cyclone with increasing *S*.

Appendix 1

List of Publications already published/accepted/submitted or in preparation:

Refereed Journals

Wang XW, Zhou Y, Wong WO 2011 Turbulent flow structure and swirl number effect in a cyclone. *Journal of Fluids Engineering* (accepted).

Zhou Y, Du C, Mi J, Wang XW 2011 Turbulent round jet control using two steady mini-jets. *AIAA Journal* (accepted).

Alam MM, Zhou Y, Wang XW 2011 The wake of two side-by-side square cylinders. *Journal of Fluid Mechanics* **669**: 432-471.

Chan T.L., Gosse K., Zhou Y., Lee S.C., Wang X.W. and Huang J.F. 2008 Effect of Rear Slant Angle on Flow Structures, and Pollutant Dispersion and Concentration Fields in the Wake of the Studied Model Vehicle. *Int. J. Heat and Mass Transfer* **51,** 6180-6193.

Wong WO, Wang XW and Zhou Y 2007 Turbulent Flow Structure in a Cylinder on Cone Cyclone. *Journal of Fluids Engineering* **129:** 1179-1185.

Lai WC, Zhou Y, Wong WO and Wang XW 2007 Effect of an oscillating cylinder on flow in a cylinder array. *Dynamics of Continuous, Discrete and Impulsive Systems Series* B: *Applications & Algorithms* **14**(S8)**:** 63-77.

Wang ZJ, Zhou Y and Wang XW 2004 Temperature measurements on a heated cylinder placed in a cylinder near-wake using a fiber-optic Bragg grating sensor. *ASME Transactions-Journal of Heat Transfer,* **26**: 62-69.

Wang ZJ, Zhou Y, Wang XW and Jin W 2003 A Fiber-Optic Bragg Grating Sensor for Simultaneous Static and Dynamic Temperature Measurement on A Heated Cylinder in Cross-Flow. *International Journal of heat and Mass Transfer* **46**: 2983-2992.

Wang XW, Zhang HJ, Zhou Y and Tu JY 2002 Flow Visualization behind Three Cylinders of Equal and Unequal Spacing, *Journal of Flow Visualization and Image Processing,* **9**: 139-151.

Ho HL, Jin W, Chan CC, Zhou Y, and Wang XW 2002 A Fibre Bragg Grating Sensor for Static and Dynamic Measurands. *Sensors and Actuators A: Physical,* **96(**1): 21-24.

Refereed conference proceedings

Wang XW, Zhou Y, Wong WO 2011 Swirl Number Effect on the Turbulent Flow Structure in a Cylinder-on-Cone Cyclone. *4th International Conference on Experiments/Process/System Modeling/Simulation/Optimization*, Athens, 6-9 July, 2011, pp. 612-619.

Pin Y F, Zhou y, Liu Y & Wang X W 2010 Effect of clearance on the flow structure behind a 3d Ahmed vehicle model, proceedings of 4th International Conference from Scientific Computing to Computational Engineering (4th IC-SCCE), pp. 222-231, July 7-10, 2010, Athens, Greece. ISBN: 978-960-98941-4-2.

Wong WO, Wang XW and Zhou Y 2005 Flow Measurement in a Cyclone Using PIV and LDA. *Symposium of Flow, Structural Vibration, Their Interaction and Control*,

Guelph, Canada, July 29-31, pp. 8-19.

Wang ZJ, Wang XW, Zhou Y and Wong WO 2002 Fluctuating Temperature Measurement on a Cylinder in a Cross Flow Using Fibre-optic Bragg Grating Sensors. *Proc. of 11th International Symposium on Applications of Laser Techniques to Fluid Mechanics (CD Rom), Lisbon,* Paper 18.2.

Ho HL, Jin W, Chan CC, Zhou Y & Wang XW 2001 Fibre Bragg grating sensor for static and dynamic measurands, *Proceedings of SPIE,* Singapore. Nov 28-30, Vol. 4596, paper no. 4596-18.

Wang XW, Zhou Y & Li H 2001 Vortex Structures behind Three Side-by-Side Cylinders, *Proceedings of 5th World Conference on Experimental Heat Transfer, Fluid Mechanics and Thermodynamics,* Thessaloniki, Greece, September 24-28, pp.2417-2422.

References

Adaramola, M.S., Akinlade, O.G., Sumner, D., Bergstrom, D.J. & Schenstead, A.J. 2006 Turbulent wake of a finite circular cylinder of small aspect ratio. *Journal of Fluids and Structures***. 22**: 919-928.

Ahmed SR 1981 Wake structure of typical automobile shapes. *ASME Journal of Fluids Engineering* **103**:62-169.

Ahmed SR 1983 Influence of base slant on the wake structure and drag of road vehicles. *ASME Journal of Fluids Engineering* **105**:429-434.

Ahmed SR & Baumert W 1979 The structure of wake flow behind road vehicles. aerodynamics of transportation. ASME-CSME Conference, Niagara Falls, June 18-20 pp93-103.

Ahmed SR, Ramm G, Faltin G 1984 Some salient features of the time averaged ground vehicle wake. *SAE Technical Paper* No.: 840300, USA.

Alekseenko SW, Kuibin PK, Okulov VL, Shtork SI 1999 Helical Vortex in Swirl Flow. *J. Fluids Mech.*, **382:**195-243.

Beaudoin JF, Aider JL 2008 Drag and lift reduction of a 3D bluff body using flaps. *Experiments in Fluids* **44**(4):491-501

Bearman PW 1997 Near wake flows behind two- and three-dimensional bluff bodies. *Journal of Wind Engineering and Industrial Aerodynamics* **69-71**:33-54.

Biffin M, Syred N, Sage P 1984 Enhanced collection efficiency for cyclone dust separators. *Chem. Eng. Res. Des.* **62**(4):261-265.

Bose PK, Roy K, Mukhopadhya N, Chakraborty RK 2010 Improved theoretical modeling of a cyclone separator as a diesel soot particulate emission arrester. *International Journal of Automotive Technology* **11**:1-10.

Brunn A, Wassen E, Sperber D, Nitsche W, Thiele F 2007 "Active drag control for a generic car." *In Active Flow Control (ed. King R), NNFM95, 247-259, Springer-Verlag Berlin Heidelberg.*

Cassidy JJ, Falvey HT 1970 Observations of unsteady flow arising after vortex breakdown. *J. Fluids Mech.* **41:**727-736.

Chanaud RC 1965 Observations of oscillatory motion in certain swirling flows. *J. Fluids Mech.* **21**:111-127.

Chao YC, Leu JH, Hung YF, Lin CK 1991 Downstream boundary effects on the spectral characteristics of a swirling flowfield. *Experiments in Fluids* **10**:341–348.

Cristea ED, Malfa E, Coghe A 1994 3-D Simulation and Experiments of Cement Rotary Kiln Preheater Top Cyclone. *Proceedings of Fluent European User's Group Meeting, Harrogate, U. K., C54.*

Czarny O, Iacovides H, Launder BE 2002 Precessing vortex structures in turbulent flow within rotor-stator disc cavities. *Flow Turbulence and Combustion* **69**:51-61.

Depardon S, Lasserre JJ, Brizzi LE, Boree J 2006 ¼ Scale vehicle wake pattern analysis using near-wall PIV. *SAE Technical Paper* No. 2006-01-1027, USA.

Derksen JJ, 2003 Separation performance predictions of a Stairmand high-efficiency cyclone. *AIChE journal* **49**:1359-1371.

Derksen JJ, Van den Akker HEA 2000 Simulation of Vortex Core Precession in a Reverse-Flow Cyclone. *AIChE Journal* **46**:1317-1331.

Duell EG, George AR 1999 Experimental study of a ground vehicle body unsteady near wake. *SAE Technical Paper* No.: 1999-01-0812.

Farell C, Carrasquel S, Guben O, Patel VC 1977 Effect of wind tunnel walls on the flow past circular cylinders and cooling tower models. *Journal Fluids Engineering* **99**:470-479.

Gouldin FC, Halthore RN, Vu BT 1984 Periodic oscillations observed in swirling flows with and without combustion. Proceedings of the Twentieth Symposium (international) on combustion, The Combustion Institute, pp. 269-276.

Harvey JK 1962 Some observations of the vortex breakdown phenomenon. *J. Fluids Mech.* **45:**585-592.

Hoekstra AJ 2000 Gas Flow Field and Collection Efficiency of Cyclone Separators. *Ph.D. thesis, Delft University of Technology.*

Hoekstra AJ, Israel AT, Derksen JJ, Van den Akker HEA 1998 The Application of Laser Diagnostics to Cyclonic Flow with Vortex Precession. *Int. Symp. Applications of Laser Techniques to Fluid Mechanics, Lisbon.*

Hoekstra AJ, Israel AT, Derksen JJ Van den Akker HEA 1999 An experimental and numerical study of turbulent swirling flow in gas cyclones. *Chem. Eng. Sci.* **54**: 2055-2065.

Hoffmann & Stein 2002 Gas Cyclones and Swirl Tubes, Principles, Design and

Operation, Springer, pp 38.

Hsieh KT, Rajamani RK 1991 Mathematical Model of the Hydrocyclone Based on Physics of Fluid Flow. *AIChE Journal* **37**:735-746.

Hu JC, Zhou Y, Dalton C 2006 Effects of the corner radius on the near wake of a square prism. *Experiments in Fluids* **40**:106-118.

Huang J F, Zhou Y & Zhou T M 2006 Three-dimensional wake structure measurement using a modified PIV technique, *Experiments in Fluids* **40,** 884-896.

Hucho WH, Sovran G 1993 Aerodynamics of Road Vehicles. *Ann. Rev. Fluid Mech.* **25:** 485-537.

Janssen LJ, Hucho WH 1974 Aerodynamische Formoptimierung der Type VW-Golf und VW-Sirocco. Kolloquium uber Inderstrie-aerodynamik, Achen, Part 3, 46-49.

Krajnovic S, Davidson L 2002 Exploring the flow around a simplified bus with large eddy simulation and topological tools, in *The Serodynamics of Heavy Vehicles: Trucks, Buses and Trains* (Springer, Monterey, CA).

Krajnovic S, Davidson L 2003 Numerical study of the flow around the bus-shaped body, *ASME Journal of Fluids Engineering,* **125,** 500-509.

Krajnovic S, Davidson L 2005a Flow around a simplified car, Part 1: large eddy simulation. *ASME Journal of Fluids Engineering* **127**:907-918.

Krajnovic S, Davidson L 2005b Flow around a simplified car, Part 2: understanding the flow. *ASME Journal of Fluids Engineering* **127**:919-928.

Lienhart H, Becker S 2003 Flow and turbulence structures in the wake of a simplified car model. *SAE Technical Paper* No.: 2003-01-0656.

Linden AJ 1949 Investigations into cyclone dust collectors. *Proc. Inst. Mech. Eng.* **130:**233-251.

Liu ZL, Jiao J, Zheng Y, Zhang QK, Jia LF 2006 Investigation of turbulence characteristics in a gas cyclone by stereoscopic PIV. *AIChE Journal* **52**: 4150 – 4160.

Lu X, Wang SW, Sung HG, Hsieh SY, Yang V 2005 Large-eddy simulations of turbulent swirling flows injected into a dump chamber. *Journal of Fluid Mechanics* **527**:171–195.

Minguez M, Pasquetti R, Serre E 2009 Spectral vanishing viscosity stabilized LES of the Ahmed body turbulent wake. *Communication in Computational Physics*, **5**(2-4): 635-648.

Narasimha R, Prasad SN 1994 Leading edge shape for flat plate boundary layer studies. *Experiments in Fluids*, **17**:358-360.

Nouzawa T, Haruna S, Hiasa K, Nakamura T, Sato H 1990 Analysis of wake pattern for reducing aerodynamic drag of notchback model. *SAE Technical Paper* No.: 900318, 1990.

O'Doherty T, Jaryczewski R, Bates CJ, Syred N 1991 Velocity characteristics of cyclone chambers. **1**: Laser Anemometry, ASME.

Oertel H 1990 Wakes behind blunt bodies. *Annu. Rev. Fluid Mech*. **22**:539-64.

Peng W, Boot PJAJ, Hoffmann AC, Dries HWA, Kater J, Ekker A 2001 Flow in the inlet region in tangential inlet cyclones. *Ind. Eng. Chem. Res.* **40:**5649-5655.

Peng W, Hoffmann AC, Dries HWA, Regelink MA, Stein LE 2005 Experimental

study of the vortex end in centrifugal separators: The nature of the vortex end. *Chem. Eng. Sci.* **60**:6919-6928.

Sarpkaya T 1971 On stationary and traveling vortex breakdown. *Journal of Fluid Mechanics*. **45**:545-559.

Schildmacher KU, Koch R 2005 Experimental investigation of the interaction of unsteady flow with combustion. *Journal of engineering for gas turbines and power-Transactions of the ASME* **127**(2):295-300.

Sims-Williams DB, Dominy RG, Howell JP 2001 An investigation into large scale unsteady structures in the wake of real and idealized hatchback car models. *SAE Technical Paper* No.: 2001-01-1041.

Sims-Williams, DB, 2001 Self-Excited Aerodynamic Unsteadiness Associated with Passenger Cars, PhD Thesis, University of Durham.

Sims-Williams DB, Duncan BD 2003 The Ahmed model unsteady wake: Experimental and computational analyses. *SAE Technical Paper* No.: 2003-01-1315.

So RMC, Zhou Y, Liu MH 2000 Free Vibrations of an Elastic Cylinder in a Cross Flow and Their Effects on the Near Wake. *Experiments in Fluids*, **29**, 130-144.

Solero G, Coghe A 2002 Experimental fluid dynamic characterization of a cyclone chamber. *Exp. Therm. Fluid Sci.* **27**:87–96.

Strachan RK, Knowles K, Lawson NJ 2007 The vortex structure behind an Ahmed reference model in the presence of a moving ground plane. *Experiments in Fluids*, **42**:659-669.

Thompson M, Hourigan K, Sheridan J 1994 Three-dimensional instabilities in the cylinder wake, Int. Colloq. Jets, Wakes, Shear Layers, Melbourne, Australia, April 18-20, Paper 10.

Ustimenko BP, Bukhman MA 1968 Turbulent flow structure in a cyclone chamber. *Teploenergetika* **15**(2):64-67.

Vino, G., Watkins, S., Mousley, P., Watmuff, J., Prasad, S. 2005 Flow structures in the near-wake of the Ahmed model. *Journal of Fluids and Structure* **20**:673-695.

Wang HF, Zhou Y, Chan CK and Lam KS 2006 Effect of initial conditions on interaction between a boundary layer and a wall-mounted finite-length-cylinder wake. *Physics of Fluids* 18: Art. No. 065106.

Wang ZJ, Zhou Y 2005 Vortex Interactions in a Two Side-by-Side Cylinder Near-Wake. *International Journal of Heat and Fluid Flow* **26**:362-377.

Wang ZJ, Zhou Y, Huang JF, Xu YL 2005 Fluid dynamics around an inclined cylinder with running water rivulets. *Journal of Fluids and Structures* **21**:49-64.

Williamson CHK 1996 Vortex dynamics in the cylinder wake. *Ann. Rev. Fluid. Mech*. **28**:477.

Wong WO, Wang XW Zhou Y 2007 Turbulent flow structure in a cylinder-on-cone cyclone. *Journal of Fluids Engineering* **129**:1179-1185.

Zhou, Y., and Antonia, R.A., 1995, “Memory effects in turbulent plane wakes,” *Exp.*

Fluids, 19, pp. 112–120.

Wu J, Sheridan J, Welsh MC and Hourigan K 1996 Three-dimensional vortex structures in a cylinder wake, *Journal of Fluid Mechanics*. **312**, 201.

Zhang H-Q, Fey U, Noack BR, König M & Eckelmann H 1995 On the transition of the cylinder wake, *Phys. Fluids* **7**, 779.

Zhang H.J., Zhou, Y. & Antonia, R.A.: 2000. Longitudinal and spanwise structures in a turbulent wake, *Physics of Fluids*, **12**: 2954-2964.

Zhang H.J., Zhou Y., Whitelaw J.H. 2006 Near-field wing-tip vortices and exponential vortex solution. *Journal of Aircraft* **43**:446-449.

Zhou LX, & Soo SL 1990 Gas-solid flow and collection of solids in a cyclone separator. *Powder Technology* **63**:45-53.

Zhou Y & Antonia RA 1994 Critical points in a turbulent near wake. *Journal of Fluid Mechanics* **275:**59-81.

Zhou Y & Antonia RA 1995 Memory Effects in Turbulent Plane Wakes. *Experiments in Fluids* **19**:112-120.

Zhou Y & Yiu MW 2006 Flow structure, momentum and heat transport in a two-tandem-cylinder wake, *Journal of Fluid Mechanics* **548**:17 - 48.